UNIVERSITY OF TWENTE.

Nelen & Schuurmans

Representing spatially variable bathymetry and vegetation in a hydrodynamic model: A subgrid-based case study in the Whitianga Estuary, New Zealand

Olof Baltus

M.Sc. Thesis
11 July 2022

Supervisors:
dr. ir. E.M. Horstman
dr. ir. P. C. Roos
dr. ir. N.D. Volp
ir. M. Siemerink
ir. R. Gijsman

Civil Engineering & Management
Faculty of Engineering Technology
University of Twente
P.O. Box 217
7500 AE Enschede
The Netherlands

Preface

In front of you lies my master thesis ”Representing spatially variable bathymetry and vegetation in a hydrodynamic model: A subgrid-based case study in the Whitianga Estuary, New Zealand”, this work is the final part of my master Water Engineering and Management with a specialization in River&Coastal engineering.

This thesis was written during an internship at Nelen & Schuurmans from February till July 2022. I want to thank my supervisors, Nicolette Volp and Martijn Siemerink from Nelen & Schuurmans for always being available for questions and suggestions during my research. Next to my supervisors, I want to thank all other colleagues at Nelen & Schuurmans that were available for questions during my internship. I also want to thank my daily University supervisor, Erik Horstman, for his extensive feedback during our weekly meetings. Next to my daily supervisor I want to thank Pieter Roos and Rik Gijsman for their participation in my graduation committee.

I hope you enjoy reading my master thesis.

Olof Baltus

Utrecht, 11-07-2022

Summary

Due to climate change and sea level rise, there is an increasing need for sustainable and cost-effective coastal protection. Mangrove eco-systems have shown to be a sustainable addition to traditional coastal protection. Mangrove forests are capable to attenuate waves and lower water levels and by sediment trapping elevate their surroundings to grow with sea level rise. However, mangrove eco-systems have a limited capability to adapt to sea level rise. Therefore, it is important to learn more about the functioning and persistence of mangroves. Often hydrodynamic models form the basis of numerical studies into these dynamics. To correctly model the hydrodynamics, high resolution spatial data needs to be taken into over large areas, which leads to long computational times. This leads to interest in computationally efficient and accurate hydrodynamic models. Subgrid-based hydrodynamic models have proven to use spatial data (e.g. bathymetry) with a high spatial resolution in a computationally efficient way. But in subgrid-based hydrodynamic models, vegetation is currently only taken into account by increasing the bed roughness. Representing vegetation via bed roughness has the downside that the roughness contribution does not scale with the water depth, while drag due to vegetation does scale with the water depth. Also, when looking into morphodynamics, the bed shear stresses are over-estimated if vegetation is incorporated as a bed roughness.

Therefore, this study explores two options of how to include vegetation in a subgrid-based hydrodynamic model. More specifically, how the *Avicennia marina variant Australasica* mangrove species can be represented correctly in the model. A mangrove study area in New Zealand is used, where an extensive measurement campaign took place in February 2017. In this period, bathymetric, vegetation, water level and velocity measurements have been done. Based on these measurements, a hydrodynamic base-case model without a vegetation representation is made. Two vegetation representations are added to the model. The first representation is using a spatially varying roughness, where the bed roughness is increased at vegetated areas to take into account the effect of vegetation. The second representation will use the Darcy equations to model the flow through vegetation as flow through a porous medium. To test the functioning of both vegetation representations, competences for model accuracy are defined, based on the key characteristics of the tidal dynamics of the area.

The results of the different models demonstrate that the use of subgrid has significant potential in the modeling of intertidal area. As it allows for the use of larger computational grid cells without loss of accuracy. This results in lower computational cost of the model. Modeling a whole spring-neap cycle (12 days) took only a little more than an hour, while decreasing the computational grid to the resolution of the spatial data the computational cost of the model increased to 140 hours. Next to this, the research has shown that the subgrid modeling technique can especially be used in intertidal areas as the flow is mainly bathymetry driven, shown in the accuracy of the modeled tidal flow-stage curves.

The results of the vegetation representations show that spatially varying bed roughness did improve the overall functioning of the model on the defined competences. Due to the increased bed shear stress on the forest platform, more water is routed via the creeks, increasing the flow velocity in the creeks according to the measurements. But on the other hand, the varying roughness did show to have only minor affect on the highest water level modeled in the study area, caused by the decreased influence of the bed roughness on large water depths. The flow through a porous medium, implemented via an interflow layer, showed to have no significant effect on the highest water levels in the area and showed to have less predictive capability on the low water levels in the creek due to the decreased of the bathymetry on the flow. But, the interflow layer did improve the modeled flow velocities on the forest platform.

For future research, it would be recommended to look further into using the subgrid modeling technique to model intertidal area like mangroves as it has shown to decrease computational cost without massively affecting the modeled hydrodynamics. For the vegetation representations, it is recommended to use varying vegetation characteristics when extensive vegetation measurements are available. Additionally it is recommended to further develop the interflow layer, so that the interflow layer can be applied to parts of the model domain with dense vegetation. At last, it is recommended to look into other vegetation representations that scale with the water depth, as the roughness raster has shown to be less applicable for highly varying water levels.

Contents

Preface iii

Summary v

1 Introduction 1

1.1 Motivation . . . 1
1.2 Problem formulation . . . 2
1.3 Research Questions . . . 3
1.4 Methodology . . . 3
1.5 Report organization . . . 5

2 Background into (modeling of) mangrove systems 7

2.1 Functioning and persistence of mangrove eco-systems . . . 7
2.2 Effect of vegetation on hydrodynamics . . . 9
2.3 Current vegetation representations in hydrodynamic models . . . 11
2.3.1 Increasing bed roughness . . . 11
2.3.2 Trachytope approach . . . 12
2.4 3Di hydrodynamic modeling software . . . 13
2.4.1 Subgrid-based modeling . . . 13
2.4.2 Vegetation in the 3Di model environment . . . 14

3 Study area analysis 17

3.1 Whitianga Estuary . . . 17
3.2 Study Area . . . 18
3.3 Field data collection . . . 19
3.4 Study area characteristics & tidal dynamics . . . 20
3.4.1 Bathymetry . . . 20
3.4.2 Vegetation . . . 21
3.4.3 Tidal Dynamics . . . 22

4 Model competences **27**
4.1 Normalized root mean square error . . . 28
4.2 Tidal flow-stage curves . . . 28
4.3 Duration asymmetry . . . 29
4.4 Along creek delay . . . 29
4.5 Maximum flow velocities . . . 30
4.6 Asymmetry flow velocities . . . 30

5 Base-case model **33**
5.1 Model Domain . . . 33
5.2 Bathymetry . . . 34
5.3 Computational Grid . . . 36
5.3.1 Computational grid size outside the study area . . . 36
5.3.2 Computational grid within the study area . . . 39
5.4 Boundary Conditions . . . 41
5.5 Base-case simulation . . . 42

6 Vegetation Representations **45**
6.1 Roughness raster . . . 45
6.1.1 Roughness raster calibration . . . 46
6.1.2 Results and comparison to measured characteristics . . . 47
6.2 Interflow layer . . . 52
6.2.1 Calibration . . . 53
6.2.2 Results and comparison to measured characteristics . . . 55
6.3 Evaluation of vegetation representations . . . 60

7 Discussion **63**
7.1 Implications of the results . . . 63
7.1.1 Use of subgrid-based modeling in intertidal areas . . . 63
7.1.2 Modeled tidal flow-stage curves . . . 64
7.1.3 Water level results . . . 65
7.1.4 Flow Velocities . . . 67
7.2 Uncertainties in the used methodology . . . 68
7.2.1 Uncertainties in the hydrodynamic model in- and output . . . 68
7.2.2 Calibration and validation . . . 70

8 Conclusions and recommendations **73**
8.1 Conclusions . . . 73
8.2 Recommendations for future research . . . 75

References

A Water levels vegetation representations
A.1 Water level roughness raster . . . .
A.2 Water levels interflow layer . . . .

Appendices

B Results base-case simulation

List of Figures

1.1 Flowchart research methodology 5

2.1 Mangrove distribution around the world from Töpke (2022). 7
2.2 Interaction between hydrodynamic, morphological and ecological processes in mangroves (Gijsman et al., 2021) 8
2.3 Different scales of turbulence in vegetation. With the black line being the flow velocity profile. (Nepf, 2012) 10
2.4 Representation of the vertical velocity profile in two zones for submerged vegetation from Baptist et al. (2007) 13
2.5 Example of a computational cell with higher resolution subgrid for bed levels retrieved from https://docs.3di.live/bgrid.html 14
2.6 Schematization of an interflow layer 15

3.1 (a) Location Whitianga Estuary on north island New Zealand. (b) Study area location within Whitianga estuary. (c) study area including measurement stations, retrieved from Horstman et al. (2021) 18
3.2 Impression of the vegetation in the study area 19
3.3 Measured water levels at the different creek stations. (a) from 12 February till 18 February (b) from 12 February till 14 February 22
3.4 (a) Measured duration asymmetry at the creek stations (b) Measured along creek delay of the HWL and LWL in relation to creek station C0 23
3.5 Measured tidal velocity asymmetry at (a) the creek stations and (b) the forest stations 24
3.6 Tidal flow-stage curves for the different creek stations from Horstman et al. (2021). With the white dots being the maximum ebb flow velocities and the yellow dots being the maximum flood flow velocities during each tide 25

4.1 Schematization of the duration asymmetry 29
4.2 Schematization of the velocity asymmetry 31

5.1 Model domain of the Whitianga Estuary. The green line on the north of the model domain is representing the location of the tidal boundary condition. The boundary on the west of the model domain is representing the location of the assumed natural flow boundary. On the south and southeast of the model domain the closed boundary upstream of the river is shown with the green lines 34
5.2 Comparison of the measured and the constructed elevation, as used in the DEM. Along two transects 35
5.3 DEM after reconstructing lower elevations, elevation given in m+MSL . 35
5.4 Locations where water levels and flow velocities will be compared in a sensitivity analysis on the effects of varying grid sizes on model predictions. In the blue shaded area, the smaller computational grid will be applied. 37
5.5 Sensitivity analysis of the water levels on varying grid sizes. (a) Location 1 (b) Location 2 and (c) Location 3 in figure 5.4 37
5.6 Sensitivity analysis of the flow velocities on varying grid sizes. (a) Location 1 and (b) Location 2 in figure 5.4 38
5.7 Sensitivity analysis of the flow velocities on varying grid sizes. (a) Location 3 and (b) Location 4 in figure 5.4 40
5.8 Computational grid used in the hydrodynamic model of the Whitianga estuary. 41
5.9 Modeled and measured water level time series after calibration of the boundary condition, retrieved at creek station C0 42
5.10 Comparison of the water level at creek stations C5 and C6 between a simulation including subgrid and a simulation excluding subgrid . . . 43
5.11 Comparison of the tidal flow-stage curves of a simulation including subgrid and a simulation excluding subgrid 44

6.1 Base roughness raster with a Chézy roughness of 60 [$m^{1/2}s^{-1}$] in the creek (white) and a Chézy roughness of 2 [$m^{1/2}s^{-1}$] in the forest (black) 46
6.2 Simulated tidal flow-stage velocity curves for all creek stations, blue and pink dots indicate maximum ebb and flood tidal velocities during each individual tide. Modeled using a roughness raster. 48
6.3 Duration asymmetry of the simulated tidal dynamics at the creek stations. Modeled using a roughness raster 49
6.4 Along creek delay of the LWL, modeled using a roughness raster . . . 50
6.5 Flow velocity in creek station C3 and concurring forest station F3N, modeled using a roughness raster 51

6.6 Ratio between simulated maximum ebb and flood flow velocity at the forest stations using a roughness raster 52
6.7 Ratio between simulated maximum ebb and flood flow velocities at the creek stations using a roughness raster 52
6.8 Simulated tidal flow-stage velocity curves for all creek stations, blue and pink dots indicate maximum ebb and flood tidal velocities during each individual tide. Modeled using an interflow layer 55
6.9 Duration asymmetry at the creek stations using an interflow layer . . . 56
6.10 Along creek delay of tidal low- water levels using an interflow layer . . 57
6.11 Modeled flow velocities at stations C3 and F3N, using an interflow layer 58
6.12 Ratio between maximum ebb and flood flow velocity at the creek stations, modeled using an interflow layer 59
6.13 Ratio between maximum ebb and flood flow velocities at the forest stations, modeled using an interflow layer 59

7.1 Modeled water levels at all creek stations from 12 February till 14 February, (a) water levels modeled by the base-case model (b) water levels when applying a roughness raster and (b) applying an interflow layer 66
7.2 Flow routing using a calibrated roughness raster during ebb-tide on 14 February 2017 68

A.1 Comparison between modeled and measured water levels at creek station C0 . . . .
A.2 Comparison between modeled and measured water levels at creek station C1 . . . .
A.3 Comparison between modeled and measured water levels at creek station C2 . . . .
A.4 Comparison between modeled and measured water levels at creek station C3 . . . .
A.5 Comparison between modeled and measured water levels at creek station C4 . . . .
A.6 Comparison between modeled and measured water levels at creek station C5 . . . .
A.7 Comparison between modeled and measured water levels at creek station C6 . . . .
A.8 Comparison between modeled and measured water levels at creek station C0 . . . .
A.9 Comparison between modeled and measured water levels at creek station C1 . . . .

A.10 Comparison between modeled and measured water levels at creek station C2 . . . .
A.11 Comparison between modeled and measured water levels at creek station C3 . . . .
A.12 Comparison between modeled and measured water levels at creek station C4 . . . .
A.13 Comparison between modeled and measured water levels at creek station C5 . . . .
A.14 Comparison between modeled and measured water levels at creek station C6 . . . .

B.1 Duration asymmetry at the creek stations modeled with the base-case model . . . .
B.2 Along creek delay of the LWL, modeled using the base-case model . .
B.3 Flow velocity in creek station C3 and concurring forest station F3N, modeled using the base-case model . . . .
B.4 Ratio between maximum ebb and flood flow velocities at the forest stations, modeled using the base-case model . . . .
B.5 Ratio between maximum ebb and flood flow velocities at the creek stations, modeled using the base-case model . . . .
B.6 Simulated tidal flow-stage velocity curves for all creek stations, blue and pink dots indicate maximum ebb and flood tidal velocities during each individual tide. Modeled using the base-case model . . . .

List of Tables

2.1 Solid volume fraction of different mangrove types (Krauss et al., 2003; Mazda et al., 1997; Norris et al., 2017) 9

3.1 Vegetation properties along the transects, retrieved from Horstman et al. (2021) 21

4.1 Competences for validating the performance of the hydrodynamic models set-up in this research 27
4.2 28

5.1 Sensitivity analysis results outside the study area. RMSE of the different grids is calculated in relation to the 10 m by 10 m grid with equation 4.1 and the computational time is retrieved for a 5 day simulation. 39
5.2 Sensitivity analysis results of the computational grid in the study area. RMSE calculated using equation 4.1. The computational time is retrieved for a 5 day simulation. 40

6.1 Chezy roughness calibration ranges defined with roughness values found in Horstman et al. (2021), Mazda' et al. (1995) and Stark et al. (2015) 47
6.2 Deviations between modeled and measured HWL and LWL using a roughness raster at creek station C0 and C5 47
6.3 Mean deviation of HWL and LWL over every tidal cycle at all creek stations (C0-C6) 47
6.4 Model settings for the model with an interflow layer 53
6.5 Calibration parameter values for the interflow layer 54
6.6 mean deviation of HWL and LWL for every tidal cycle at all creek stations 54
6.7 Checklist qualitative comparison tidal flow-stage curves 60
6.8 Normalized root mean squared error results for the different hydrodynamic models set-up in this research tested on the first four competences 61

Chapter 1

Introduction

1.1 Motivation

Hundreds of millions of people worldwide are exposed to coastal flood risk (Kulp & Strauss, 2019). These risks are expected to increase, due to sea level rise (Kirezci et al., 2020; Taherkhani et al., 2020; Woodruff et al., 2013). Moreover, the population living in low-lying coastal area will probably increase rapidly (Neumann et al., 2015). These developments ask for cost-effective solutions for coastal defence. Using mangroves can be a cost-effective and sustainable option for providing such coastal protection (Gijsman et al., 2021). As they have to natural ability to attenuate wind waves and reduce surge levels, thereby providing coastal protection (Horstman et al., 2013b; Mazda et al., 2006). Mangrove ecosystems can also adapt to sea level rise by capturing sediment (Gijsman et al., 2021; Krauss et al., 2003). However, their ability to adapt to sea level rise is limited. If the sea level rise out-paces the accretion rate of the mangroves, the mangroves will drown and the functioning of mangroves in reducing flood risk will decrease. In the past 30 year the worldwide mangrove coverage has been reduced from $18.8 * 10^6$ ha to about $13.8 * 10^6$ ha (FAO, 2007; Giri et al., 2011). For this reason it is important to learn more about the functioning and persistence of mangroves to be able to use them in a safe/sound way for coastal protection.

In the development of knowledge about the functioning and the persistence of mangroves, hydrodynamic and ecological models of mangrove eco-systems are essential. Hydrodynamic models can be used to predict tidal dynamics in mangroves and learn more on the effect of human induced changes on mangrove areas (Horstman et al., 2015). For example reclaiming part of the mangrove extent for agriculture or damming a river reducing the sediment supply. The hydrodynamics simulated by a hydrodynamic model form the input for ecological models. Ecological models can be used to simulate the growth of mangroves and find out the effect of changing hydrodynamics on the growth of mangroves (Best et al., 2018). The predicted growth of mangroves trees can afterwards be used as input for the hydrodynamic models. The understanding of mangrove eco-systems is continuously improving due to model studies and measurements campaigns. To be able to simulate future scenarios with changing conditions, computationally fast and accurate hydrodynamic models are needed.

1.2 Problem formulation

An important limiting factor within the field of hydrodynamic modeling is the computational time. High-resolution data of the bathymetry and vegetation is required to accurately simulate hydrodynamics in mangrove forests. This is especially important in mangrove eco-systems, as large variations in elevation and vegetation properties are observed in mangrove forests. High-resolution spatial data is often available through new techniques like LiDAR. However, increasing spatial resolution significantly increases computational time, resulting in a trade-off between the spatial resolution of a hydrodynamic model and the computational time. Due to this trade-off the available fine resolution spatial data is often averaged over large grid sizes (Hu et al., 2018; Menéndez et al., 2018). Averaging spatial data over computational grid cells can have large effect on the modeled hydrodynamics in the area (Gourgue et al., 2021). Therefore, it is important to explore the implementation of small scale spatial data in large scale hydrodynamic models.

For the reason described in the previous paragraph, there is a large need for computationally fast and accurate hydrodynamic models, which can include high spatial resolution data at low computational costs. Subgrid-based hydrodynamic models have shown to be able to computationally efficient deal with high resolution spatial data like bathymetry and varying roughness (Casulli, 2009; Volp et al., 2013). In subgrid-based hydrodynamic models, vegetation is currently often taken into account by increasing the bed roughness. Although this method is easy to use, it is only limited in application. As the physics behind the increased drag due to vegetation is a vertical drag and not a horizontal shear stress. Therefore, the drag exerted by vegetation scales with the water depth/vegetation height and not with the horizontal surface area. Next to the added drag, also diffusivity is added to the flow by high density vegetation (Nepf, 1999). The diffusivity caused by vegetation is not correctly captured when representing vegetation as an increased bed shear stress.

1.3 Research Questions

The goal of this research is to determine how the inclusion of a vegetation representation in a subgrid-based hydrodynamic model affects model results. To reach this goal, a case-study is used where extensive hydrodynamic and vegetation data was collected. This research goal resulted in the following main research question.

What is the effect of taking mangrove vegetation into account in a subgrid-based hydrodynamic model of the Whitianga study area?

To support the main research question, several sub-questions have been formulated.

Q1 What are the hydrodynamic forcings, area, and flow characteristics in the creek and mangrove forest of the Whitianga study area?

Q2 Which competences are expected from a good model simulation of the hydrodynamics in the Whitianga study area?

Q3 What is the effect of including subgrid on simulated hydrodynamics in a hydrodynamic model?

Q4 How can vegetation be represented in a subgrid-based hydrodynamic model and what are the differences between the vegetation representations?

Q5 To what extent do the different representations of vegetation in a subgrid-based hydrodynamic model capture the observed tidal characteristics of the Whitianga mangrove forest?

1.4 Methodology

To investigate our main research question a mangrove eco-system is used as study area. The study area is an intertidal mangrove forest dissected by a creek in New Zealand, where extensive field measurements were performed by Horstman et al. (2021). The first part of this research will identify the geographic and hydrodynamic characteristics of the study area. Based on these characteristics, competences will be defined to test the hydrodynamic models. The competences for the hydrodynamic models will be designed to represent the key tidal flow characteristics observed in the area.

For the hydrodynamic simulations, the hydrodynamic software 3Di is used. With this software, three different models are set up: The base-case model, the model with a roughness raster as vegetation representation, and the model with an interflow layer as vegetation representation. The base-case model will be set-up, in order to set basic model parameters and boundary conditions, which will be kept constant during the rest of the research. The model parameters already chosen in the base-case model are the model domain, bathymetry, boundary conditions, and the computational grid size. Keeping these parameters constant throughout the research, will make it possible to purely compare the effect of the vegetation representations. The hydrodynamics modeled with the base-case model are serving as reference values in comparing the hydrodynamic models including a vegetation representation. Additionally, the base-case will be used to show the effect of the subgrid modeling approach.

To include the effect of vegetation on hydrodynamics in the subgrid-based hydrodynamic models, two vegetation representations have been explored. The first vegetation representation is based on an increased bed roughness, implemented via a spatially varying roughness raster. The second vegetation representation is based on diffusive flow through a porous medium, implemented via an interflow layer. Further explanation of these two vegetation representations is given in section 2.4.1.

The hydrodynamic models including a vegetation representation will be calibrated using the modeled highest water level (HWL) and lowest water level (LWL) during each tide. The HWL and LWL have been chosen as calibration parameter as the flow in the study area is mainly forced by the water level gradient, which means that if the HWL and LWL are simulated accurately the flow in the study area will also be simulated accurately. The HWL and LWL will be calibrated by comparing the measured HWL and LWL of each tide with the modeled HWL and LWL and calculate the mean deviation at each creek station (C0-C6). This process is continued till the mean deviation in HWL and LWL of all creek stations combined is 5 cm. If this exit criterion is not reached within 8 simulation runs the best performing run from these eight simulations will be used for the further validation of the vegetation representation.

The hydrodynamic models will be validated using the competences earlier defined. For the base-case model and the model including a roughness raster, the simulated flow velocities and water levels can be directly retrieved from the model results. When using an interflow layer within 3Di, the flow velocity and discharge of the flow within the interflow layer is computed apart from the open water flow velocity above the interflow layer. To be able to compare the modeled with the measured flow velocities, a depth-averaged flow velocity is calculated. This is explained in section 2.4. The methodology used is summarized in figure 1.1.

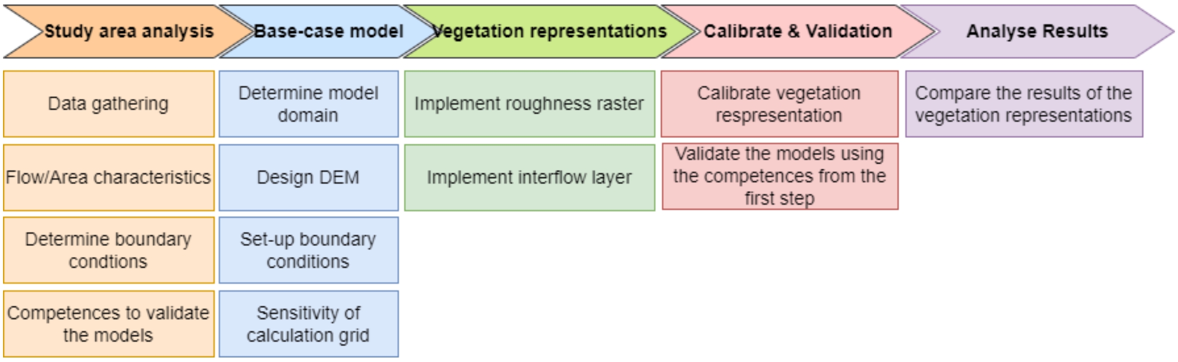

Figure 1.1: Flowchart research methodology

1.5 Report organization

In chapter 2, the theoretical background for this research will be given. In chapter 3, the study area will be introduced and the results of the measurements will be presented from which the competences will be set-up. In chapter 4 the competences used to validate the models will explained. In chapter 5, the set-up of the base-case model will be explained. In chapter 6, the implementation, calibration, results, and the validation of the vegetation representations will be presented. In chapter 7, the implications of the results and the uncertainties of this research are discussed. At last in chapter 8, the conclusions of this research and recommendations for future research will be given.

Chapter 2

Background into (modeling of) mangrove systems

2.1 Functioning and persistence of mangrove eco-systems

Mangrove forests are self-organizing complex eco-systems. Mangroves can be found in tropical intertidal coastal zones around the equator as they are vulnerable to frost (Ostling et al., 2009). The global distribution of mangroves is shown in figure 2.1.

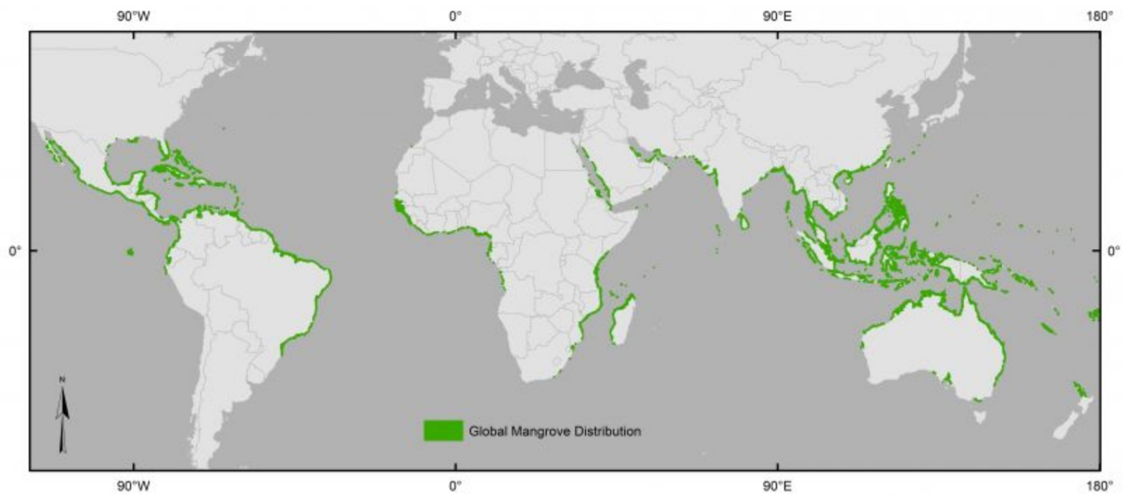

Figure 2.1: Mangrove distribution around the world from Töpke (2022).

Mangrove eco-systems have the capability to attenuate waves, caused by the energy losses due to vegetation drag and energy dissipation (Horstman et al., 2014). Wave attenuation rates between 0.002 m^{-1} were observed in sparsely vegetated forest fringes, and up to 0.012 m^{-1} in the dense vegetation. In addition, the wave attenuation in the mangroves was found to increase sediment deposition in the area (Horstman et al., 2014). The sediment deposition, increases for higher suspended sediment concentrations, increased tidal inundation frequency, inundation depth, and mangrove forest width and density (Furukawa & Wolanski, 1996; Horstman et al., 2014). The wave attenuation and the capability of mangroves to trap sediments is important for the flood protection service of mangroves and the ability of the mangroves to cope with sea level rise. The wave attenuation and sediment trapping in mangroves is governed by continuous interactions between hydrodynamic, morphological and ecological processes. These interactions are schematised in figure 2.2. The capacity to attenuate waves is governed by the present state of a mangrove forest. The persistence of a mangrove forest is governed by the change of the present state over time, driven by morphological changes, changes in forest composition, and changes in hydrodynamic forcings (Gijsman et al., 2021).

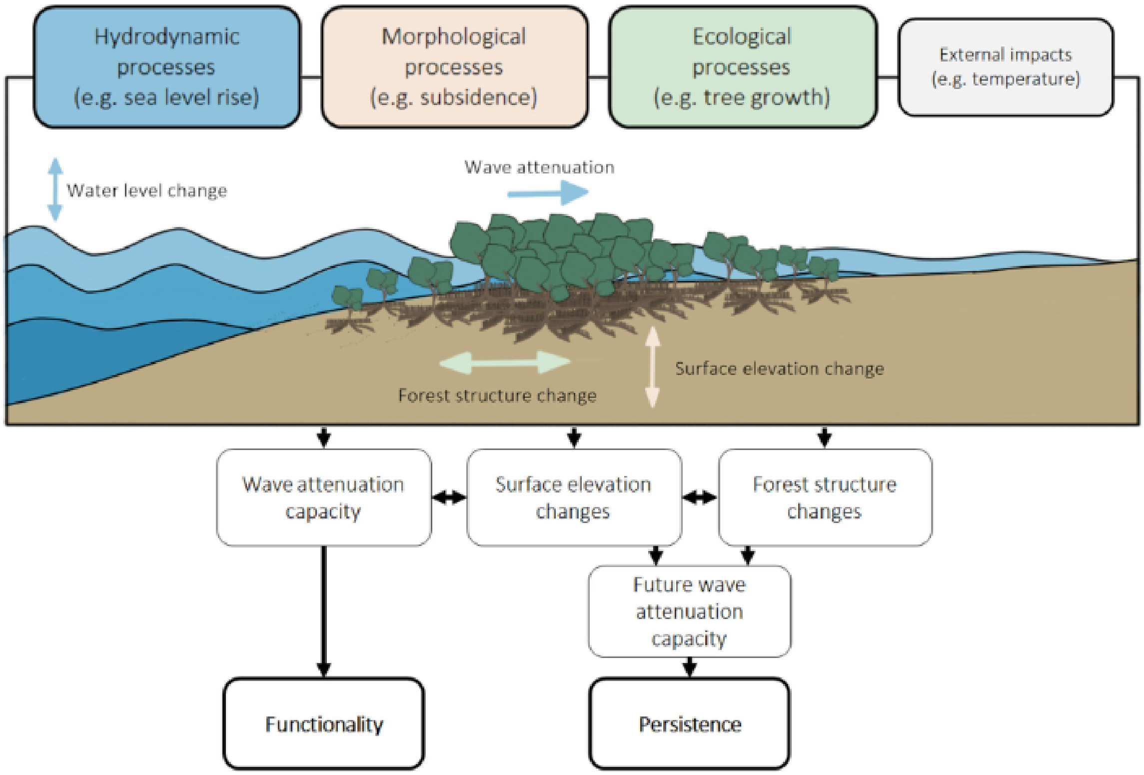

Figure 2.2: Interaction between hydrodynamic, morphological and ecological processes in mangroves (Gijsman et al., 2021)

The ability of the mangrove eco-systems to reduce flood risk depends on the capacity to attenuate waves as they approach the coast. This is called the functionality of a mangrove eco-system (Gijsman et al., 2021). The functionality of mangrove systems depends on multiple hydrodynamic and biophysical factors: inundation depth, wave height, wave period, flow velocity, intertidal topography, presence of creeks, forest width, tree species, tree stem density, tree stem diameter and tree height. For the functionality it is therefore important that these characteristics are consistent over time.

Unfortunately, mangroves are vulnerable eco-systems as they have species specific thresholds regarding inundation level and duration (Saintilan et al., 2020). If these thresholds are exceeded mangroves trees could starve (Gijsman et al., 2021). Therefore, the persistence of mangrove ecosystems is primarily affected by the surface elevation changes in relation to water levels. These thresholds are affected by two main factors. On the long term, mangroves are under threat of sea level rise (SLR). Which could cause that mangroves' critical threshold are exceeded causing starvation of mangrove trees. On the short term, mangroves are affected by storms which could damage parts of the mangrove forest.

2.2 Effect of vegetation on hydrodynamics

The presence of vegetation in intertidal areas can introduce significant spatial variation in the flow. The effect of vegetation on hydrodynamics is largely influenced by the amount and spacing of the vegetation stems in an area, also called the geometry (Mullarney & Henderson, 2018). The geometry of vegetation can vary a lot between different species but also within an area the vegetation geometry can vary significantly. Therefore, statistics are needed describing the vegetation geometry in an area. One of the most important vegetation geometry characteristics describing vegetation is the solid volume fraction of the vegetation, in this research denoted as φ (Britter & Hanna, 2003; Lowe et al., 2007). The solid volume fraction can be calculated using equation 2.1 (Mullarney & Henderson, 2018).

$$\varphi = \frac{N\pi d^2}{4} \tag{2.1}$$

With N being the number of stems per square meter and d is the diameter of the vegetation [m]. For mangrove vegetation, observed solid volume fractions are given in table 2.1.

Mangrove type	Solid volume fraction (φ)
Trunks	0.003-0.005
Prop roots	0.073-0.13
Pneumatophores	0.0003-0.038

Table 2.1: Solid volume fraction of different mangrove types (Krauss et al., 2003; Mazda et al., 1997; Norris et al., 2017)

The spatial variation in flow can be described on multiple scales. On an individual stem scale, the vegetation introduces turbulence through vortex shedding and wake generation shown in figure 2.3a (Mullarney & Henderson, 2018). This dominates the flow resistance in low density vegetation. In more dense vegetation, the flow resistance is dominated by the blockage of flow as the flow velocity through the vegetation gets smaller (Nepf, 2012). This is visualized in figure 2.3, where the flow velocity through and above the vegetation is shown.

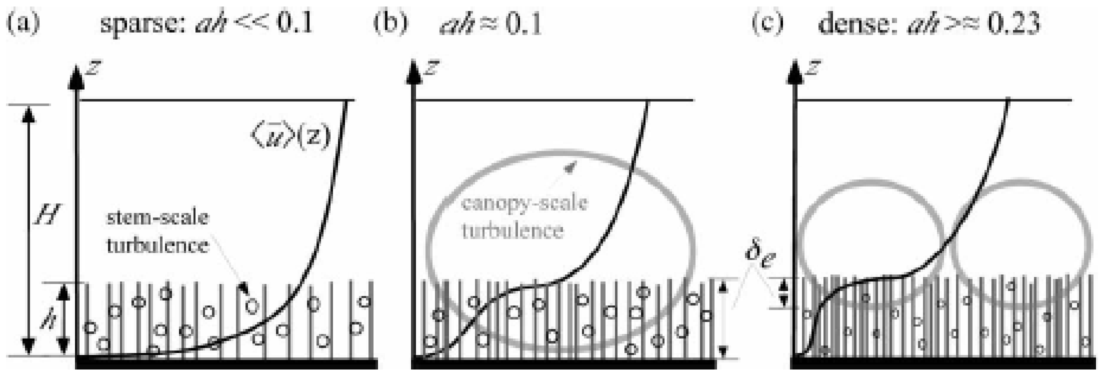

Figure 2.3: Different scales of turbulence in vegetation. With the black line being the flow velocity profile. (Nepf, 2012)

On a canopy scale, vegetation alters velocity profiles and dense canopy with a uniform height can create a very strong shear layer on top of the vegetation causing canopy scale turbulence. Moreover, it can create damping of larger scale motion, which is caused by the increased drag force and eddy viscosity by the vegetation (Mazda et al., 2005). Canopy-scale turbulence is created by the difference in flow velocity in the vegetation layer and above the vegetation layer creating a shear layer on top of the vegetation (Nepf, 2012).

Next to creating extra drag, vegetation also adds diffusivity to the flow (Nepf, 1999). The diffusion within vegetation is determined by two processes, the turbulent and the mechanical diffusion. The turbulent diffusivity is governed by the stem density and the flow velocity scale (Nepf, 1999). Mechanical diffusion, is common in porous media flow and is reflects the dispersion of flow particles due to the variability of the flow paths (Nepf, 1999). This concept is also applicable to flow through vegetation, as in vegetated flows the flow particles can also have different flow paths due to obstruction by stems. Therefore, it is important in modeling of vegetation that the diffusivity is also taken into account.

2.3 Current vegetation representations in hydrodynamic models

2.3.1 Increasing bed roughness

The simplest way vegetation is currently taken into account in hydrodynamic models is by increasing the bed roughness (Breda et al., 2021; Menéndez et al., 2018). Previous studies show different approaches of capturing the increased drag of vegetation using an increased roughness. Some of them focused on mangrove ecosystems: Menéndez et al. (2018) increased the bed roughness uniform over the whole mangrove model domain, Breda et al. (2021) applied an increased roughness only at cells where mangrove trees were present. Previous numerical modeling studies of the interactions between a creek channel and its surrounding forest platform found Chézy values as small as 1-5 [$m^{1/2}s^{-1}$] for mangrove forest platforms (Mazda' et al., 1995) and 10-20 [$m^{1/2}s^{-1}$] on salt marsh platforms (Stark et al., 2015), whereas values of 61 and 55-75 [$m^{1/2}s^{-1}$] were used for the creek channels through these eco-systems.

Horstman et al. (2021) shows that a simplified momentum balance can be used to compute a representative bed shear stress from measured hydrodynamics in the area (equation 2.2).

$$g\frac{d\eta}{dx} = -\frac{\tau_{bed} + \tau_{veg}}{\rho h} = -C_D\frac{U|U|}{h} \tag{2.2}$$

With g being the gravitational acceleration [ms^{-2}], $\frac{d\eta}{dx}[-]$ being the along creek water level gradient in x direction, $\tau_{\text{bed + veg}}$ $[Nm^{-2}]$ being respectively the bed shear stress and the vegetation drag, h the water depth [m], and U being the local depth-averaged flow velocity $[ms^{-1}]$ in x direction. These friction losses can be combined to one bulk drag coefficient, $C_D[-]$ (Friedrichs, 2010). The bulk drag coefficient can be derived by the gradient of a linear fit through the water pressure gradient $(g\frac{d\eta}{dx})$ as a function of $U|U|/h$ (Mullarney et al., 2017). The bulk drag coefficient is combining the bed roughness and the vegetation drag, which can be computed with equations 2.3 and 2.4.

$$\tau_{\text{bed}} = \rho\frac{g}{C_{\text{bed}}^2}U|U| \tag{2.3}$$

$$\tau_{\text{veg}} = \frac{1}{2}\rho C_D N d k U|U| \tag{2.4}$$

With C_{bed} being the Chézy coefficient of the bed roughness $[m^{1/2}s^{-1}]$. Combining equations 2.2, 2.3 and 2.4 the representative roughness can be calculated with equation 2.5.

$$\tau_{\text{bed+veg}} = \rho C_D U|U| = \rho \frac{g}{C^2} U|U| \tag{2.5}$$

Where C is the combined representative roughness, defined as a Chézy coefficient.

2.3.2 Trachytope approach

Next to the increased bed roughness approach, the effect of vegetation can also be taken into account via the trachytope approach (Haughey, 2017; Horstman et al., 2015; Hu et al., 2018). The trachytope approach resolves the effect of vegetation on hydrodynamics by increasing the bed roughness and adding flow resistance (Deltares, 2021). The computation of the bed roughness and flow resistance is based on the vegetation equations of Baptist et al. (2007). The equations of Baptist et al. (2007), are split-up in an equation for emergent vegetation and an equation for submerged vegetation. The equation for emergent calculates a representative roughness that scales with the water depth. The representative roughness for emergent vegetation is given by equation 2.6.

$$C_k = \sqrt{\frac{1}{1/C_{\text{bed}}^2 + (C_{\text{D}} N d h)/(2g)}} \tag{2.6}$$

With C_k being the representative Chézy coefficient for emergent vegetation [$m^{1/2}s^{-1}$].

For the submerged vegetation, Baptist et al. (2007) used two different methods to derive the theoretical resistance equation for submerged vegetation. In this section only the "method of effective water depth" will be explained, more information about the derivation of the analytical approach can be found in the paper of Baptist et al. (2007). The effective water depth method is based on the assumption that there are two flow zones. A vegetation zone, where an uniform flow velocity, u_c, is present. In the second zone, the layer above the vegetation, the flow velocity (u_u) is assumed to vary in height with a log. profile. At the top of the vegetation (k), u_u has the same flow velocity as within the vegetation. This is schematized in figure 2.4.

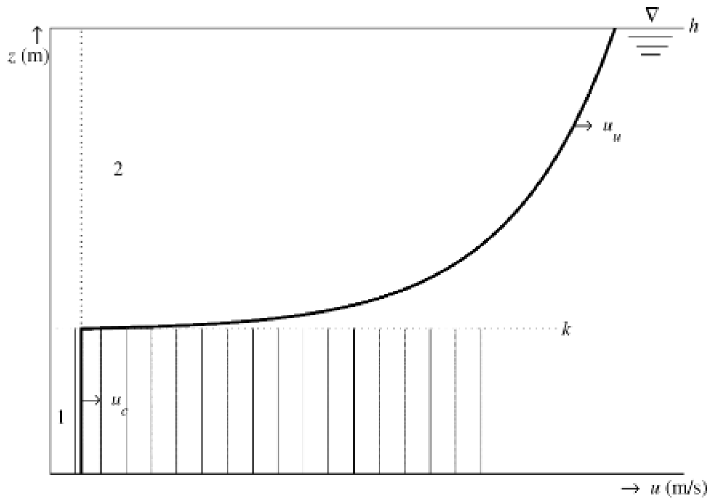

Figure 2.4: Representation of the vertical velocity profile in two zones for submerged vegetation from Baptist et al. (2007)

Combining the equations of these two flow zones results in a representative Chézy roughness calculated with equation 2.7. With the first term on the right being equal to the equation of the emergent vegetation 2.6. With C_r being the representative Chézy value for submerged vegetation [$m^{1/2}s^{-1}$], κ the Von Kármán constant, and e is the base of the natural logarithm.

$$C_{\mathrm{r}} = \sqrt{\frac{1}{1/C_{\mathrm{bed}}^2 + \left(C_{\mathrm{D}} mDk\right)/(2g)}} + \frac{(h-k)^{3/2}(\sqrt{g}/\kappa)\ln\left((h-k)/ez_0\right)}{h^{3/2}} \tag{2.7}$$

2.4 3Di hydrodynamic modeling software

In this research, the 3Di modeling software is used. 3Di has been developed by Nelen&Schuurmans in combination with Deltares, Delft University of Technology, G.S. Stelling, and several water authorities. 3Di is a hydrodynamic simulation software for pluvial, fluvial and coastal flows and it is applied in both urban and rural areas around the world.

2.4.1 Subgrid-based modeling

3Di is a subgrid-based depth-averaged hydrodynamic model. Subgrid-based modeling is a recent development in hydrodynamic modeling. The method is computationally efficient and automatically deals with flooding and drying. The subgrid approach allows to take high resolution, spatially varying information into account without increasing computational cost significantly (Casulli, 2009; Volp et al., 2013).

The subgrid-based hydrodynamic model deals with two different grids. The coarse grid is the computational grid. In 3Di, a staggered Cartesian grid is used where the water level is calculated in the cell centre and the velocities are calculated at the cell edges. Within a computational cell, the bed level is allowed to vary (figure 2.5). This bed level is defined on the finer grid, the subgrid. Due to the varying bed level in a computational cell, the cell can be partly wet, completely wet or completely dry. Cell volumes, cell surfaces and cross-sectional areas of the computational cell are a non-linear function of the water level and the bathymetry. Although, the flow velocity is a course grid quantity, a high resolution estimate is used for computing the momentum balance. This is especially important for determining the friction within a computational cell. Within the subgrid modeling approach, local values for the water depth, bed roughness, and an estimated subgrid flow velocity are used to compute the bed shear stress. This prevents an overestimation of the bed shear stress in areas with a strongly varying bathymetry (Volp et al., 2013).

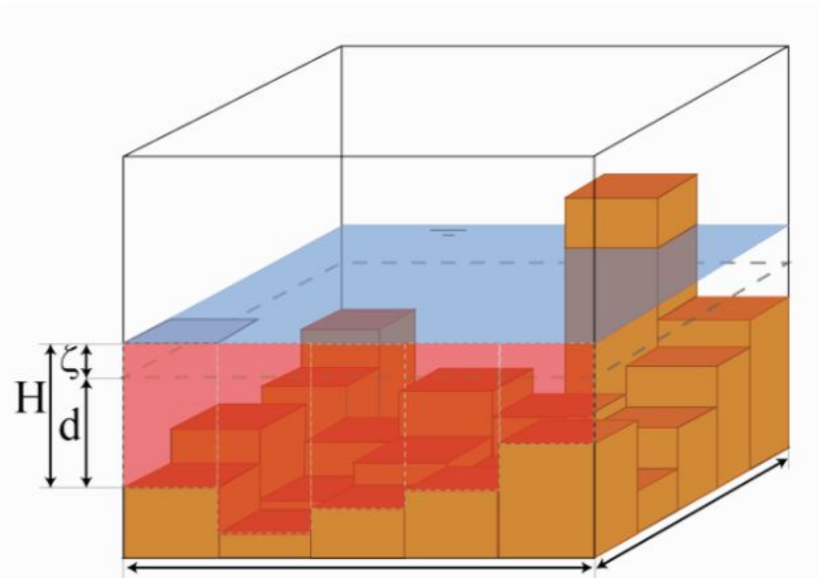

Figure 2.5: Example of a computational cell with higher resolution subgrid for bed levels retrieved from https://docs.3di.live/bgrid.html

2.4.2 Vegetation in the 3Di model environment

In this section, a more in depth explanation will be given of the specific functions used for the vegetation representations in 3Di during this research.

Roughness raster

To take the effect of vegetation into account a spatially varying roughness will be added to the model. This representation is applied to capture the large spatial variations in vegetation cover. Within 3Di the roughness can be defined at the high-resolution via the subgrid. This is done by using a roughness raster which has the same spatial resolution as the bathymetry used in the model. The high-resolution roughness raster will be defined based on measurements and literature.

Interflow layer

For the second vegetation representation an interflow layer will be added. An interflow layer is a layer with diffusive flow (Nelen & Schuurmans, 2022). In the model the interflow layer is defined from the bed up to the top of the pencil roots. The use of the interflow layer for vegetation is schematized in figure 2.6. By introducing the interflow layer, two different kind of flows are simulated. Above the vegetation, open water flow is simulated calculated by the depth-averaged shallow water equations. In the interflow layer, diffusive flow is simulated.

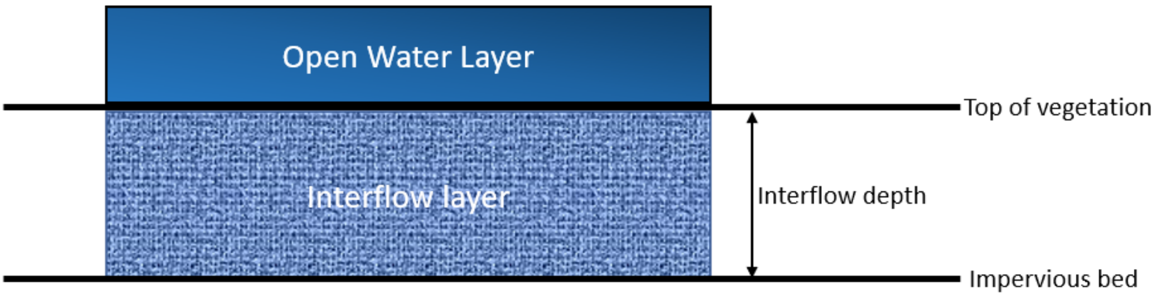

Figure 2.6: Schematization of an interflow layer

The flow through an interflow layer is described by the Darcy equations for diffusive flow given in equations 2.8 and 2.9. With $\kappa[m/s]$ being the hydraulic conductivity, $A_I[m^2]$ the the cross-sectional area, and $\frac{\delta\eta}{\delta x}$ being the water level gradient in the x and respectively also the y direction of the 2D domain. With the x direction being defined from east to west and the y direction from south to north.

$$Q_I^x = -\kappa A_I^x \frac{\delta\eta}{\delta x} \tag{2.8}$$

$$Q_I^y = -\kappa A_I^y \frac{\delta\eta}{\delta y} \tag{2.9}$$

The interflow layer is defined by the porosity, depth, and the hydraulic conductivity. In 3Di there are four methods to define the interflow layer using the input parameters. In the first two methods the storage in the interflow layer is known apriori (Nelen & Schuurmans, 2022). As this is not the case in our use of the interflow layer because of the varying water level, these two methods can not be used. In the other two methods, the volume of water in the interflow layer is based on the porosity of the interflow layer. The difference between the two methods is that in the first method the depth of the interflow layer is defined to the lowest elevation in the whole model and in the second method to the lowest elevation of the computational cell. For our application the interflow method with the interflow depth relative to the lowest elevation in the computational cell is used, as large differences in bed level can be found in the model domain of the Whitianga estuary.

To compare the flow velocities of the model with the measured depth-averaged flow velocities in the study area. The depth-averaged flow velocity in the whole water column is calculated using equation 2.10. Where $U_{interflow}$ is the depth-averaged flow velocity in the interflow layer [m/s], $A_{interflow}$ is the wet cross-sectional area of the interflow layer [m^2]. U_{open} is the depth-averaged open water flow velocity [m/s], and A_{open} is wet cross-sectional area above the interflow layer [m], which is retrieved from the model results. The wet cross-sectional area of the interflow layer is not stored by default in the model results. Therefore, the wet cross-sectional area has been manually reconstructed with equation 2.11.

$$U = U_{interflow} \frac{A_{interflow}}{A_{interflow} + A_{open}} + U_{open} \frac{A_{open}}{A_{interflow} + A_{open}} \tag{2.10}$$

$$A_{interflow} = Q_{interflow} / U_{interflow} \tag{2.11}$$

Chapter 3

Study area analysis

3.1 Whitianga Estuary

The mangrove ecosystem that will be used as study area is located in the Whitianga estuary, an estuary located on the north island of New Zealand (figure 3.1). The estuary is around 6 km long and up to 4 km wide, with a total area of 12.9 km^2. The whole catchment of the Whitianga estuary is 433 km^2 (Jones, 2008). The estuary has a small inlet to the ocean and is therefore sheltered from wave energy. Hence, tides are the dominant hydrodynamic forcing inside the estuary. The tide measured at the mouth of the estuary (harbor of Whitianga) is a M2 tide, with a tidal amplitude of 1.6 m during spring tide and 1.1 m during neap tide.

The estuary is populated with the *Avicennia marina variant australasica* mangrove species, which can grow up to 10 m in height. Mangroves in the estuary can be found on the intertidal profile from mean sea level to the highest spring tide mark (Horstman et al., 2018). The mangrove forests in the Whitianga estuary consist of a spatially varying density of mangrove trees with a pneumatophore cover in between the mangrove trees. Pneumatophores are small vertical above ground roots, which supply oxygen to the main root system during tidal inundation (Nair, 2010). The upper end of the intertidal area is inhabited by saltmarsh vegetation which consists of sea rush and oioi. These species form thick grasslands up to 1.5 m in vegetation height (Horstman et al., 2018). An impression of the different vegetation species in the area is given in figure 3.2.

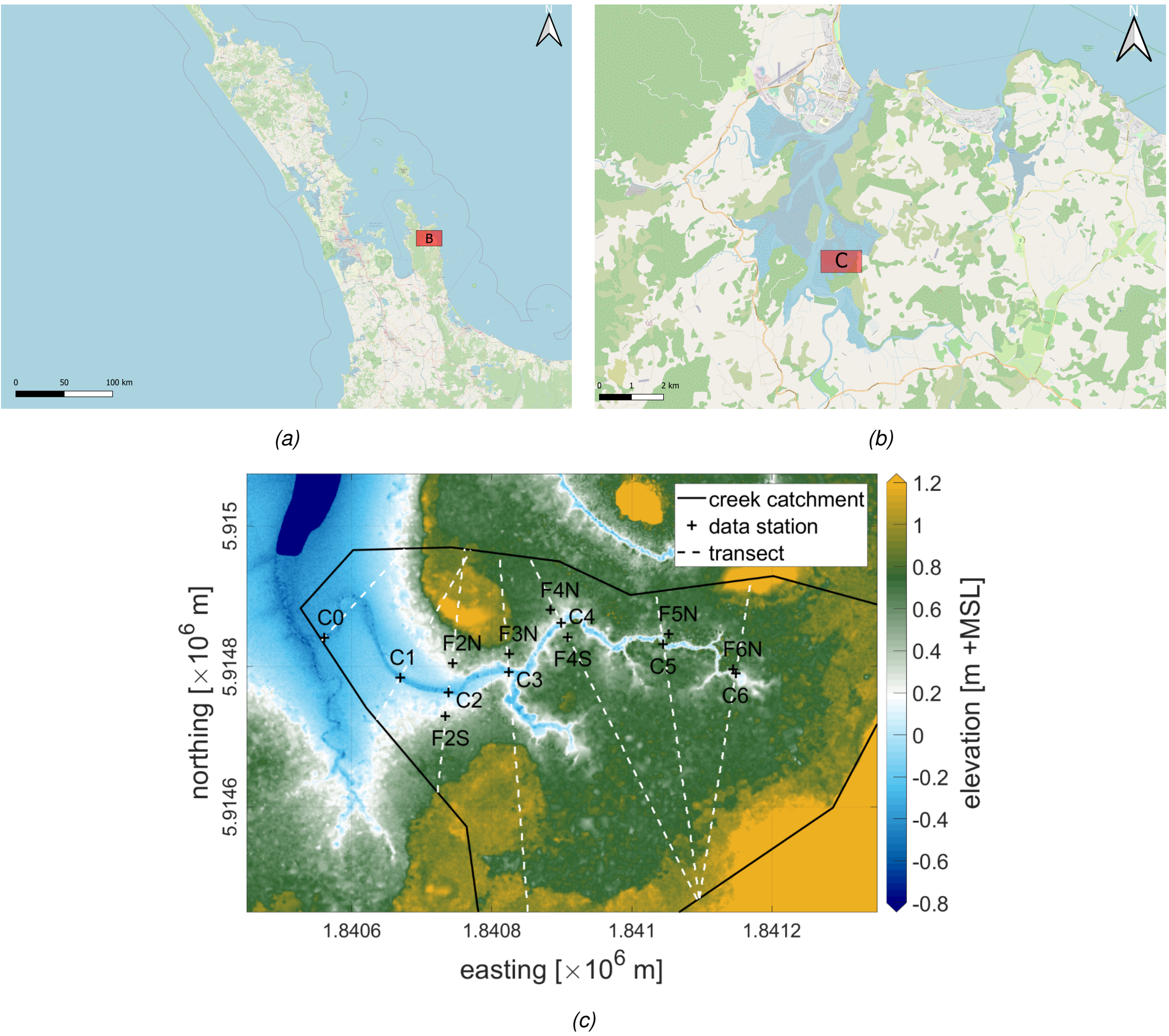

Figure 3.1: (a) Location Whitianga Estuary on north island New Zealand. (b) Study area location within Whitianga estuary. (c) study area including measurement stations, retrieved from Horstman et al. (2021)

3.2 Study Area

The study area is located in the south-east of the estuary (figure 3.1b). The study area is shown in figure 3.1c. The study area is a mangrove creek system with one major creek dissecting the mangrove forest. Bed elevations in the area vary between -0.8 m + MSL and 1.2 m + MSL (Horstman et al., 2021). The tide is entering the study area via the main channel shown in the northwest of figure 3.1c. The creek catchment has no direct freshwater input, except from intermittent rainfall.

(a) Creek measurement station C4

(b) Higher elevated area

(c) Avicennia marina variant australasica at station F2N

(d) Steep overhanging banks at creek station C5

Figure 3.2: Impression of the vegetation in the study area

3.3 Field data collection

Horstman et al. (2021) performed measurements in the area during a whole spring-neap cycle in February 2017. In the creek dissecting the mangrove forest, 7 stations (C0-C6) were installed at every 100-200 m (figure 3.1c). In addition to the creek measurement stations, extra stations were placed on the forest platform north of the creek (F2N-F6N) and at two locations south of the creek (F2S, F4S) also shown in figure 3.1c. Next to the data stations, creek normal transects were defined at each creek station. Along the transects, a manual RTK GPS (Trimble R8 GNSS) survey was performed to collect elevation data in the area. Local geodetic marks were used to obtain accurate vertical datum, with accuracy in the order of $10^{-2}m$. However, the measurements were hampered by tree cover and reception issues, resulting in a vertical accuracy of $10^{-1}m$. Additionally to the transect measurements, a LiDAR map of the study area from 2012 is available, measured by the Waikato Regional Council.

Mangrove tree density, height and diameter were measured at 30 cm above the bed in 5 m x 5 m tree plots at each of the forest stations. At each corner of the tree plots the mangrove pneumatophores were counted in 0.5 m x 0.5 m quadrats. With these measurements the total frontal area density and the total solid volume fraction of the vegetation in each of these plots was calculated. The total solid volume fraction is explained in more detail in section 2.2. At transect C1 and C2, exceptions were made for the measurements of vegetation properties, because a difference could be observed between the creek bank and the forest platform. This is also clearly visible in figure 3.1c, where the creek bank at these two transects is at lower elevation (light blue color) and the forest is at higher elevation (green color). At transect C1 the vegetation was only measured at the sparsely vegetated creek bank, as the forest fringe was narrow and transitioned into the raised saltmarsh ridges just inland of the forest fringe. At transect C2, separate vegetation plots were measured for the creek bank and the forest. This was not applicable at station C3-C6 as the creek banks were steep and unvegetated, causing a sudden transition between creek and forest platform resulting in comparable vegetation properties.

Measurements of hydrodynamic data were performed by an extensive network of acoustic flow meters and pressure gauges over a full spring-neap cycle (10-22 February 2017). At station C0-C6 the flow velocity profile was measured with intervals of 90 seconds. At the forest stations F2N, F2S, F4N, and F4S the full flow profile was measured at intervals of 900 seconds. At forest stations F3N and F5N point measurements for the velocity where performed with an interval of 900 seconds. At last, at station F6N the full flow profile was measured at 90 seconds interval. More details about the exact equipment used at the different stations can be found in the paper of Horstman et al. (2021).

3.4 Study area characteristics & tidal dynamics

3.4.1 Bathymetry

To get a continuous elevation map of the area the measurements of the cross-sections and the LiDAR map are combined. The reconstructed LiDAR map is needed as area wide coverage cannot be produced from the measured transects. The LiDAR data showed good agreement with the measured field elevation data with a correlation ($R^2 = 0.88$) after a fixed offset for all elevations above 0.4 m+MSL (Horstman et al., 2021). The deeper parts of the estuary below this elevation could not be reconstructed from the LiDAR map, due to the fact that LiDAR reflects on water. Therefore, for the cross-sectional properties of the creek the LiDAR map was substituted by manually collected survey data.

3.4.2 Vegetation

The vegetation measurements resulted in characteristics of vegetation along each transect. The total density is expressed in the total solid volume fraction (φ) calculated by equation 2.1. Along transects C1 and C2 there is a difference in vegetation density between creek bank and forest. This is related to the elevation difference between the creek bank and the forest as described in the previous section. The total vegetation density increases from 0 at transect C1 to 0.0263 at transect C6 (table 3.1). The results show that the density of the mangroves along the creek slightly increases when going further into the back of the forest. Further, a gradient along the creek was observed in the height of the pneumatophores. Where the height of the pneumatophores decreased going further into the creek system. The pneumatophore height is 13.5 cm along transect C1 and is decreasing to a height of 4.6 cm along transect C6 (table 3.1).

Transect	Pneumatophore height [cm]	Total mangrove density φ [-]
C0	-	-
C1	13.5	0
C2	9.4	0.0184
C3	7.6	0.023
C4	5.2	0.0203
C5	2.8	0.0246
C6	4.6	0.0263

Table 3.1: Vegetation properties along the transects, retrieved from Horstman et al. (2021)

As explained in chapter 2, vegetation adds extra drag to the water column. The drag and bed friction can be combined into a representative roughness, which can be computed from the measured hydrodynamics in the area (section 2.4.2). Horstman et al. (2021) computed the representative roughness values in the beginning of the creek, end of the creek between creek station C2-C6 and the forest platform. The computed Chézy roughness values in the creek (C0-C1) vary between 40-60 [$m^{1/2}s^{-1}$]. Deeper in the creek system (C2-C6) Chézy values decrease, which means that the bed roughness of the creek bank increases. This is due to the overhanging banks with root systems. Chézy values computed here are between 10-30 [$m^{1/2}s^{-1}$]. For the forest platform the computed Chézy value is between the 10-20 [$m^{1/2}s^{-1}$].

3.4.3 Tidal Dynamics

Water levels

The flow in the study area is forced by a semi-diurnal (M2) tide, with a significant spring neap cycle (figure 3.3a). A semi-diurnal tide, means that approximately twice a day high water and twice a day low water occurs. The estuary mouth is sheltering the study area from incoming wind waves. The measurement period starts at spring tide, when maximum high tidal water levels are up to 1.1 m+MSL (at creek station C0). The maximum water level at neap tide decreases to 0.6 m+MSL (figure 3.3a).

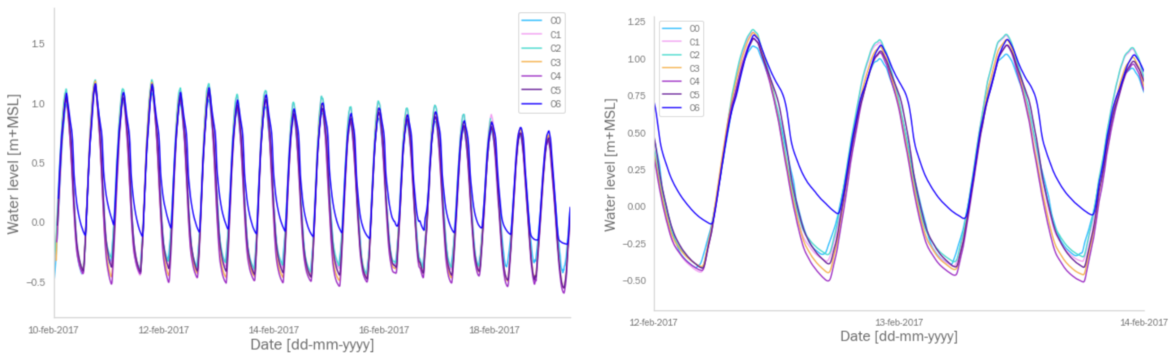

(a) (b)

Figure 3.3: Measured water levels at the different creek stations. (a) from 12 February till 18 February (b) from 12 February till 14 February

At stations C1-C2 the tidal amplitude (the difference between high water level and the consecutive low water level) is amplified by 10% compared to the seaward station C0, due to shoaling (figure 3.3b). Shoaling appears due to decreasing channel width and increasing elevation of the surrounding intertidal flats at the creek mouth. In between stations C1 till C4 the tidal amplitude remained constant as the continued shoaling was counteracted through the effect of flow divergence due to the increase in creek depth and platform width. Flow divergence increased further inland, decreasing the tidal amplitude at creek stations C5 and C6. Next to this, the tidal amplitude decayed in the landward section of the creek due to the frictional effects of a narrowing forest platform dominating over the amplifying effect of the reducing creek depth. Another factor contributing to the reduction of the tidal amplitude was the incomplete drainage of the falling tide at the inland creek end, which substantially elevated the minimum water level at low tide. The mangrove functionality is measured with the water level reduction over the full length of the mangrove system. The total water level reduction along the creek was 12 cm/km and the water level reduction over the full forest platform was 36 cm/km.

A tidal period can be split into a rising part and a falling part. Generally, there is an asymmetry in these periods caused by the bathymetry, friction and the tidal forcing (Horstman et al., 2021). In figure 3.4a, the asymmetry is shown as a ratio between the duration of falling to the rising tide. It can be seen that this asymmetry changes in the direction of the sea and during the spring-neap cycle. The asymmetry increased with tidal Highest Water Level (HWL) till the HWL reached about 1 m + MSL, where falling tides took 1.5 to 2 times longer than rising tides. With HWL larger than 1 m + MSL the duration asymmetry decreased again. A strong increase in asymmetry can be observed comparing station C6 to the other creek stations. This is caused due to the rising tide catching up with the falling tide at station C6 causing a larger asymmetry.

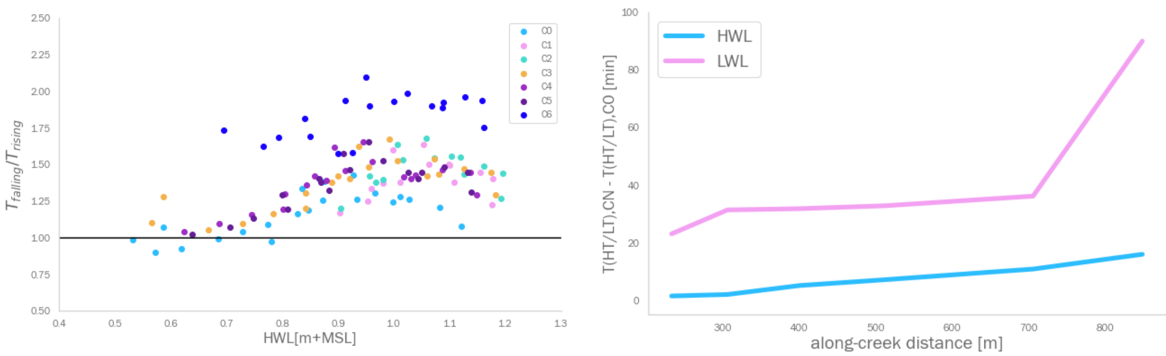

(a) *(b)*

Figure 3.4: (a) Measured duration asymmetry at the creek stations (b) Measured along creek delay of the HWL and LWL in relation to creek station C0

Next to the duration asymmetry also a large difference can be found in the along creek delay of the HWL and Low Water Level (LWL). The along creek delay is defined as the time it takes for the HWL and LWL to propagate inland along the creek in relation to station C0. In the measurements can be found that the along creek delay of the LWL is significantly larger than the delay of the HWL. This difference caused that the rising tide caught up with preceding falling tide, causing a higher elevated low tide shown in figure 3.3b.

Flow velocities

The observed flow velocities over the forest platform are slower than flow velocities in the corresponding creek stations, due to vegetation drag. At the creek stations, maximum flow velocities were reached of 0.35 m/s during flood tide and 0.7 m/s during ebb tide. In the forest, maximum flow velocities of 0.15 m/s were reached during flood tide and during ebb tide maximum flow velocities of 0.13 m/s were reached. The flow directions over the forest platform were mainly parallel aligned to the adjacent creek sections. Tidal flow asymmetries (ratio of the maximum ebb to flood flow velocities during a tidal cycle) showed opposite behaviour between the creek and the forest platform (figure 3.5). The creek is ebb-dominant and the forest platform is mainly flood dominant. The ebb dominance in the creek decreased when moving further into the creek system (station C4-C6), this can be caused by the declining size of the sub-catchment draining past these stations. For the same reason the ebb-dominance increased with tidal amplitude. This increasing effect was mainly present for water levels between 0.8 m+MSL and 1.0 m+MSL, above this threshold the ebb-dominance stayed constant. Conversely, the flood-dominance on the forest platform showed a weak declining trend with increasing HWL till about 1 m+MSL after which the asymmetry slightly increased again.

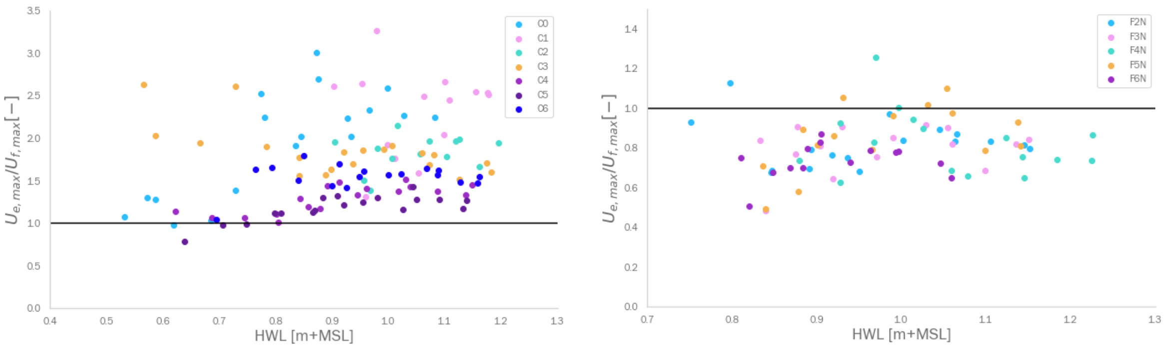

(a) (b)

Figure 3.5: Measured tidal velocity asymmetry at (a) the creek stations and (b) the forest stations

Figure 3.6 displays the tidal flow-stage curves (water level versus flow velocity) for the different creek stations. In the figure, maximum flood flow velocities per tidal cycle are given with the yellow dots and the white dots are the maximum ebb flow velocity during each tidal cycle. For creek station C0 and C1 the flow velocity maxima occurred at within-creek water levels. For creek station C2 the ebb flow maxima occurred mostly at within-creek water level while the flood flow velocity maxima occurred at over-bank elevations. At creek stations C3-C6 flow velocity maxima at the ebb- and flood-stage occurred at over-bank water levels.

In the deeply incised inland creek system (stations C3-C6), the ebb flow velocity maxima happen at water levels just above bank level. The HWL, which changes during the spring-neap cycle, does not influence the water level at which the maximum ebb flow velocities occur. On the other hand, the maximum flood flow velocity increases with the HWL. The confounding effects of the bathymetry and vegetation cause the combined variations of the occurrence of both ebb and flood flow velocity maxima throughout the area (Horstman et al., 2021).

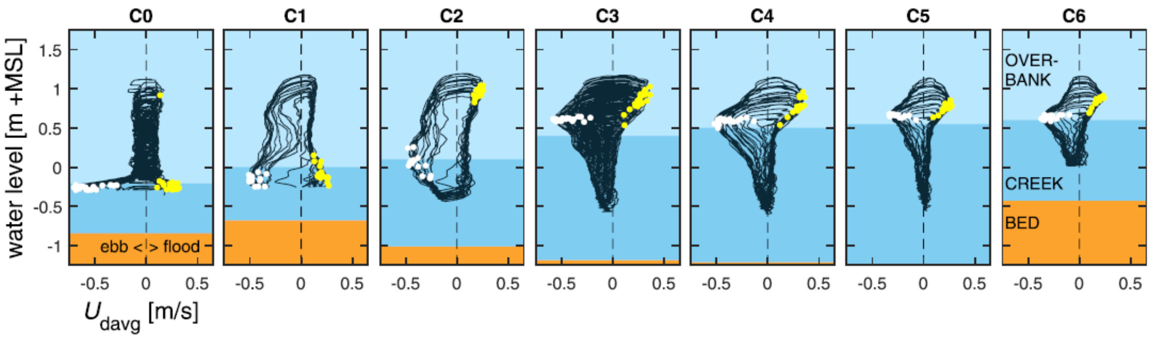

Figure 3.6: Tidal flow-stage curves for the different creek stations from Horstman et al. (2021). With the white dots being the maximum ebb flow velocities and the yellow dots being the maximum flood flow velocities during each tide

Summarizing the key tidal characteristics measured in the area:

- The duration of the falling tide is consistently longer then the duration of the rising tide. This duration asymmetry is increasing with HWL.
- The along creek propagation velocity of the LWL is consistently smaller than HWL, with a big decrease in velocity in between station C5 and C6.
- The velocity at the creek stations is a factor 3-5 higher compared to corresponding forest stations.
- The asymmetry in tidal velocities, show ebb dominant flow in the creek and flood dominant flow in the forest.
- Peak flood flow velocities occur at increasing water levels with increasing HWL, while peak ebb flow velocities constantly occur at the same just over-bank water level. Additionally, at station C0-C2 the peak ebb velocities appear at below bank elevation.

Chapter 4

Model competences

To determine the quality of the results modeled by the three hydrodynamic models, a number of competences are defined. The competences are based on the dominant flow characteristics described in the previous chapter. These characteristics are summarized at the end of section 3.4.3. The competences defined are summarized in table 4.1.

The motivation for the use of competences is that the vegetation representations can be quantitatively tested on flow characteristics in the study area. The competences are set-up to validate HWL, LWL, peak flow velocities and a combination of flow velocities and water levels via tidal flow-stage curves. Therefore, the competences are a solid validation of the performance of the different hydrodynamic models.

	Competence	Qualitative/Quantitative	Locations	Comparison Technique
1	Tidal flow-stage curves	Qualitative	C0-C6	Visual
2	Tidal duration asymmetry in the creek	Quantitative	C0-C6	NRMSE
3	Along creek delay in low water level	Quantitative	C0-C6	NRMSE
4	Maximum flow velocities in the creek and forest	Quantitative	C3 & F3N	NRMSE
5	Asymmetry in tidal velocity	Quantitative	C0-C6 F2N-F4N	NRMSE

Table 4.1: Competences for validating the performance of the hydrodynamic models set-up in this research

The hydrodynamic models will be tested on a complete spring-neap cycle (12 days). The parameters will be calculated for each tide during the spring-neap cycle (21 tides). For the quantitative competences, the computed parameters will be compared for every tide to the corresponding tide in the measurements. A more in-depth description of how the different competences will be assessed is given per competence in the sections below. But, first there will be explained how the NRMSE used in the quantitative competences is calculated.

4.1 Normalized root mean square error

To calculate the normalized root mean square error (NRMSE), first a root mean square error (RMSE) will be calculated with equation 4.1. Where $y_{simulated}$ is the simulated parameter value and $y_{measured}$ is the measured parameter value, which will be substituted with the parameters values of the quantitative competences. n is the number of parameter values used to calculate the RMSE (AgriMetSoft, 2019).

$$RMSE = \sqrt{\sum_{i=1}^{n} \frac{(y_{simulated} - y_{measured})^2}{n}} \tag{4.1}$$

To be able to compare the scoring of a model on a certain competence to scoring on other competences, the RMSE will be normalized using equation 4.2. Where the RMSE calculated with equation 4.1 is divided by the mean of the measured parameter values (AgriMetSoft, 2020).

$$NRMSE = \frac{RMSE}{\mathrm{mean}(measured)} \tag{4.2}$$

The closer the NRMSE value is to zero, the better the model prediction is on a certain competence. The NRMSE values have been classified to determine the accuracy of the model. Three classes have been distinguished (table 4.2).

NRMSE value	Interpretation
NRMSE $<$ 0.3	Accurate
0.3 $\geq$ NRMSE $\leq$ 0.7	Somewhat accurate
NRMSE $>$ 0.7	Poorly accurate

Table 4.2

4.2 Tidal flow-stage curves

To qualitatively assess the different models on this competence, tidal flow-stage curves of the creek stations will be plotted. These flow-stage curves will be tested on four (yes/no) criteria of characteristics observed in the measured tidal flow-stage curves. Both vegetation representations and the base-case will be tested on these criteria to determine how the modeled tidal flow-stage curves fit the observed characteristics.

- Maximum flow velocities at within-creek water level at station C0 and C1
- Maximum ebb flow velocity at constant water level (C3-C5)

- Maximum ebb flow velocity at just over bank water level (C3-C5)
- Increasing maximum flow velocity with increasing HWL (C3-C5)

4.3 Duration asymmetry

For the first quantitative competence 'duration asymmetry', the tidal duration asymmetry in the creek is calculated. The duration asymmetry is calculated with equation 4.3.

$$A_{duration} = \frac{T_{falling}}{T_{rising}} \tag{4.3}$$

Where the $T_{falling}$ and the T_{rising} are the duration of the rising of the tide and the falling of the tide as schematized in figure 4.1

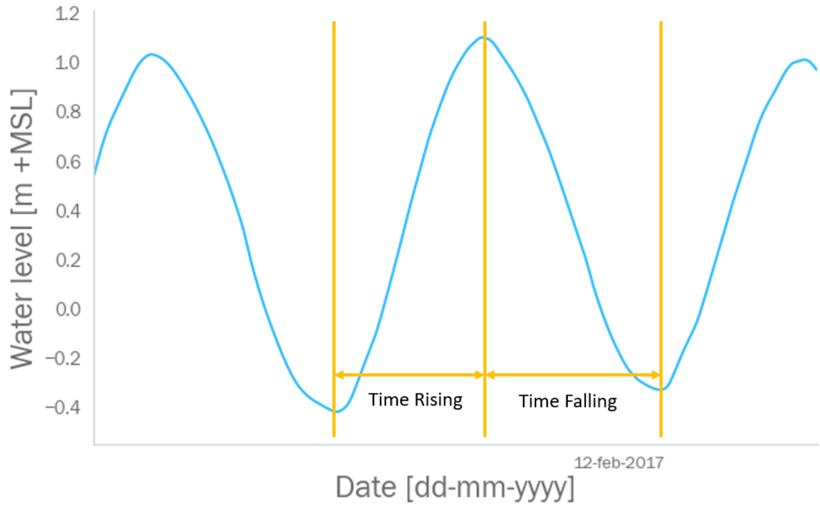

Figure 4.1: Schematization of the duration asymmetry

The duration asymmetry will be computed at all creek stations (C0-C6), after which a NRMSE is calculated for each creek station. At last, the mean is taken of the computed NRMSE's to have one NRMSE value. This NRMSE values is used in the validation of the model.

4.4 Along creek delay

For the second quantitative competence 'Along creek delay', the time it takes for the LWL to reach the different creek stations is calculated. This delay is calculated with equation 4.4

$$Delay_{LT,CN} = T_{LT,CN} - T_{LT,C0} \tag{4.4}$$

With N being substituted with the number of the different creek stations (C1-C6), $T_{LT,CN}$ being the time the low tide reaches a certain creek station, and $T_{LT,C0}$ being the time the low tide reached creek station C0. The delay (in minutes) it takes for the tidal wave to reach each creek station is calculated. Afterwards, the NRMSE for each creek station is calculated. At last, the mean is taken of the computed NRMSE's to have one NRMSE value to use in the validation of the model.

4.5 Maximum flow velocities

For the third quantitative competence 'Maximum flow velocities', the maximum flow velocities during flood and ebb tide are selected for each tidal cycle at creek station C3 and forest station F3N. After retrieving the maximum flow velocities, a NRMSE will be calculated comparing the measured low tide maximum velocities with the modeled and comparing the measured high tide maximum velocities with the modeled velocities at both measurement stations, resulting in four NRMSE's. Finally, the mean of the NRMSE's is taken to use in the validation of the model.

4.6 Asymmetry flow velocities

For quantitative competence four 'Asymmetry flow velocities', the ratio between the maximum ebb flow velocity to the maximum flood flow velocity during one tide is assessed. This ratio is calculated with equation 4.5.

$$A_{velocity} = U_{E,max}/U_{F,max} \tag{4.5}$$

Where $U_{E,max}$ is the maximum flow velocity during ebb tide in m/s and $U_{F,max}$ is the maximum flow velocity during flood tide in m/s, schematized in figure 4.2.

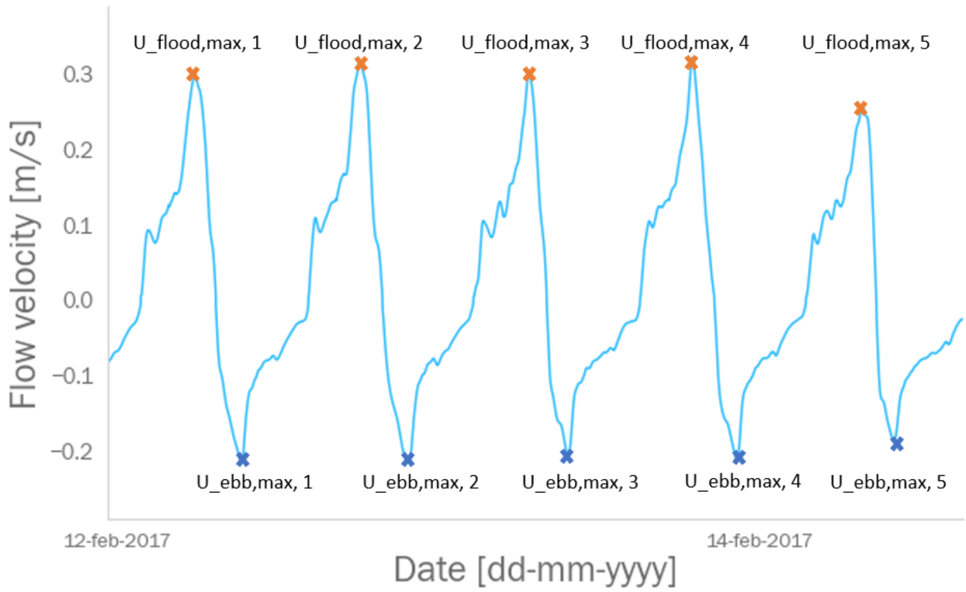

Figure 4.2: Schematization of the velocity asymmetry

The asymmetry in flow velocities is calculated for each tidal cycle at all creek and forest stations (C0-C6, F2N-F6N). After calculation, a NRMSE is calculated for each creek and forest station by comparing the modeled asymmetry with the measured asymmetry for each tidal cycle. Afterwards, the mean of the creek stations NRMSE's and the mean of the forest stations NRMSE's resulting in two NRMSE values for the tidal velocity asymmetry. These two values will be used to validate the models on this competence.

Chapter 5

Base-case model

5.1 Model Domain

It is important to choose the model domain carefully to minimize the effect of the model boundary on hydrodynamics within the study area, but also considering the availability of data. Because of the effect model boundaries have on the flow in the model, the effect of the model domain on computational times are not considered for choosing the model domain. The computational cost of the model is addressed in the choice of the computational grid size. The model domain is set-up using natural flow boundaries in the estuary. At natural flow boundaries the tidal flow is minimal, for example a tidal divide. In addition, at one of the boundaries of the model domain the forcing boundary condition must be placed.

Figure 5.1 shows the chosen model domain of the hydrodynamic model. On the northern boundary of the model domain, one inflow channel can be found. The channel is enclosed by two higher elevated areas, which makes this a suitable location for the forcing boundary. Therefore, the forcing boundary has been placed in this channel. The location is also shown in figure 5.1 with the light green line on the north boundary of the model domain. On the east side of the model domain a very shallow area in the estuary is assumed to result in minimal flow interaction between the estuary part on the west side of the island and the east side of the island. Therefore, a closed boundary has been chosen at this location. This tidal divide is also shown in figure 5.1 with a green line. On the south end of the model domain, the domain boundary is chosen as far away from the study area as data was available. Here, a river flows into the estuary. Because the discharge is small, it is considered negligible. Therefore, also at the south end a closed boundary has been chosen.

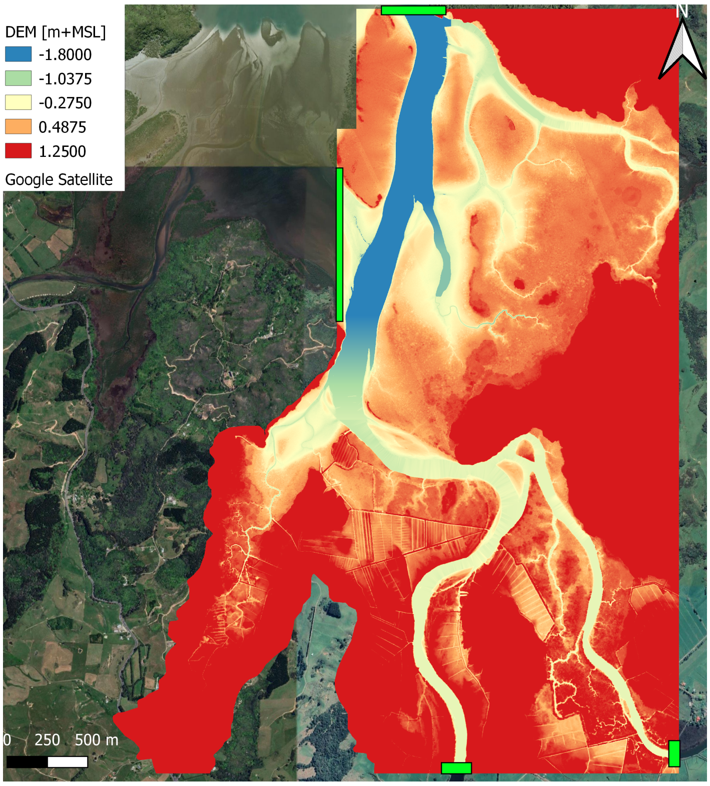

Figure 5.1: Model domain of the Whitianga Estuary. The green line on the north of the model domain is representing the location of the tidal boundary condition. The boundary on the west of the model domain is representing the location of the assumed natural flow boundary. On the south and southeast of the model domain the closed boundary upstream of the river is shown with the green lines

5.2 Bathymetry

One of the most important factors influencing flow in a hydrodynamic model is the bathymetry. The bathymetry in the hydrodynamic model is defined by combining the LiDAR map (spatial resolution of $1m^2$) and the measured transect information, that were described in chapter 3. For elevations below -0.4 m+MSL the LiDAR data is substituted with the survey data. In between the transects, the cross-sectional values are interpolated using a triangle interpolation method over the thalweg of the creek.

The constructed bathymetry is tested by comparing transects of the new bathymetry with those of the measured transects C1 and C4 (figure 5.2a and 5.2b). The comparison shows a good agreement between the constructed and the measured transects.

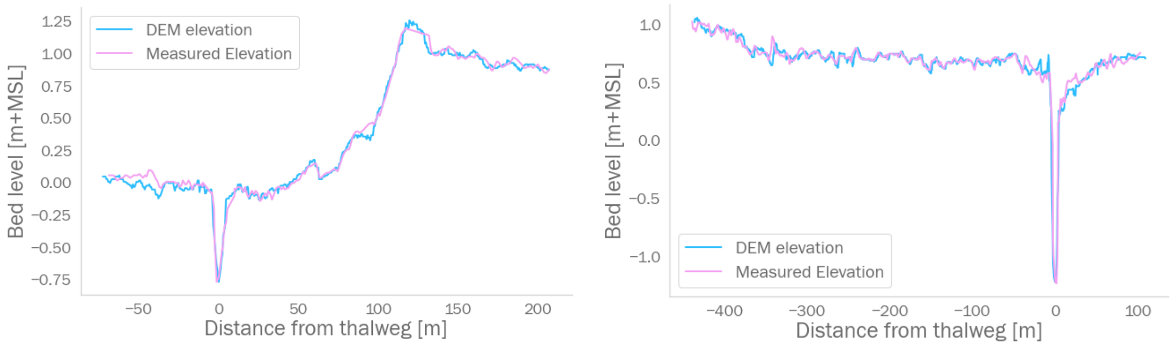

(a) Transect 1

(b) Transect 4

Figure 5.2: Comparison of the measured and the constructed elevation, as used in the DEM. Along two transects

Also outside of the study area elevations of -0.4 m + MSL appear where the LiDAR data did not provide bed levels of the deeper parts of the estuary. In contrast to the study area, only a few point measurements were available close to the study area. Therefore, an assumption is made for the bed elevation in these deeper parts. From the point measurements and an assumption made; A gradually decreasing bed level is chosen decreasing from -1.2 m + MSL just outside the creek system till -1.8 m + MSL at the model boundary in the main channel is chosen. The main channel elevation is gradually increasing till an elevation of -1 m+MSL in the rivers south of the study area. The resulting Digital Elevation Map (DEM) is shown in figure 5.3.

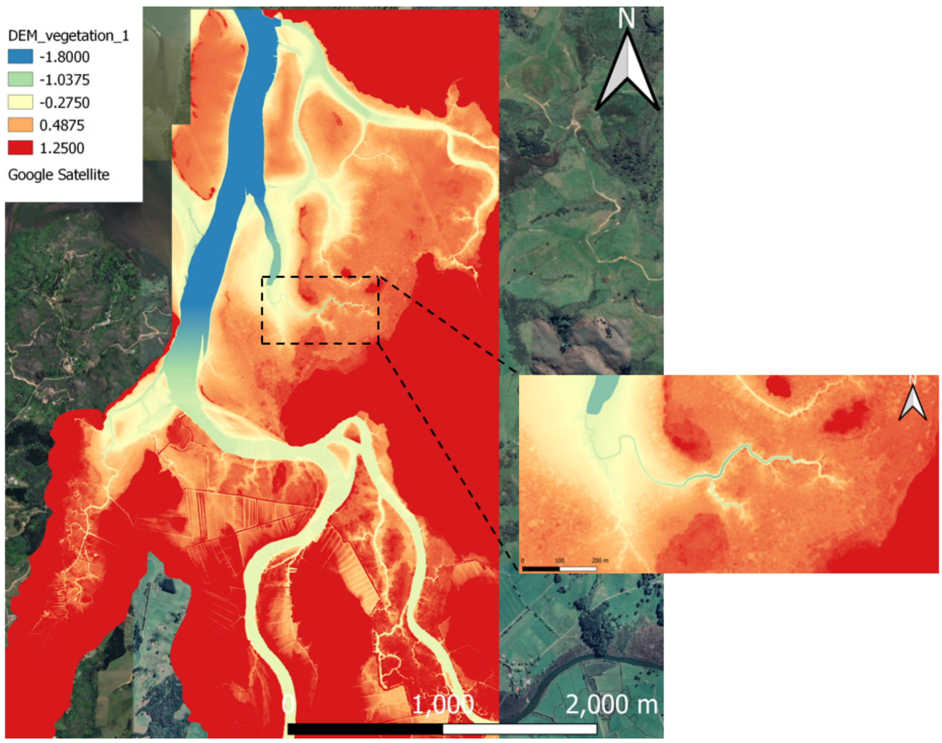

Figure 5.3: DEM after reconstructing lower elevations, elevation given in m+MSL

5.3 Computational Grid

The computational grid size is chosen using a sensitivity analysis to determine the influence of the computational grid size on simulated water levels and flow velocities. Next to the results of the sensitivity analysis, the computational times are also considered in the choice of the computational grid. Two sensitivity analysis will be performed, one for the grid size choice outside the study area and the other one for the computational grid sizes within the study area. This distinction has been made as in the study area a smaller computational grid size is required to be able to accurately compare the simulated with the measured hydrodynamics.

5.3.1 Computational grid size outside the study area

Outside of the study area, computational grid sizes of 240 m by 240 m, 120 m by 120 m, 60 m by 60 m, 40 m by 40 m, and 10 m by 10 m are tested. These grid sizes have been chosen as a grid size smaller than 10 m by 10 m will end up in computation times longer than 48 hours, which is unrealistic for use. On the other hand, choosing a computational grid size larger than 240 m by 240 m was found to not further decrease computational times making it unnecessary to choose larger computational grid cells.

The effect of computational grid size on simulated hydrodynamics outside of the study area is assessed on 5 locations: three locations to monitor water levels and two locations for flow velocities (figure 5.4). The water level is monitored as water levels outside of the study area have a strong influence on the simulated hydrodynamics within the study area. The water level locations are located in the main channel (location 1), on higher elevated terrain (location 2), and within a creek system outside of the study area (location 3). Apart from the water levels outside of the study area, the hydrodynamics in the study area are forced by the volume of water that is directed into the creek system. The main contributor to the volume of water that reaches the study area is the bifurcation in the main channel northeast of the study area. Therefore, two velocity locations have been chosen just inland of this bifurcation (velocity location 1 and 2 in figure 5.4).

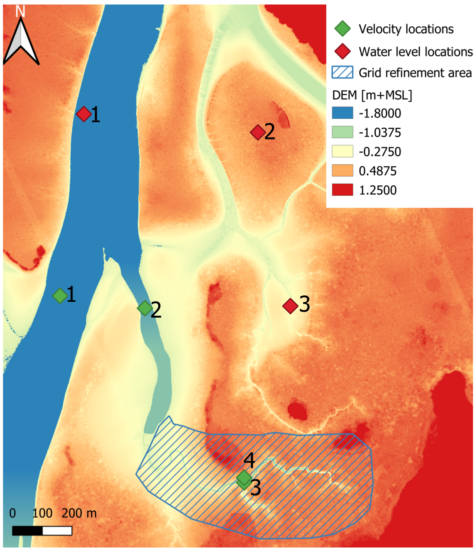

Figure 5.4: Locations where water levels and flow velocities will be compared in a sensitivity analysis on the effects of varying grid sizes on model predictions. In the blue shaded area, the smaller computational grid will be applied.

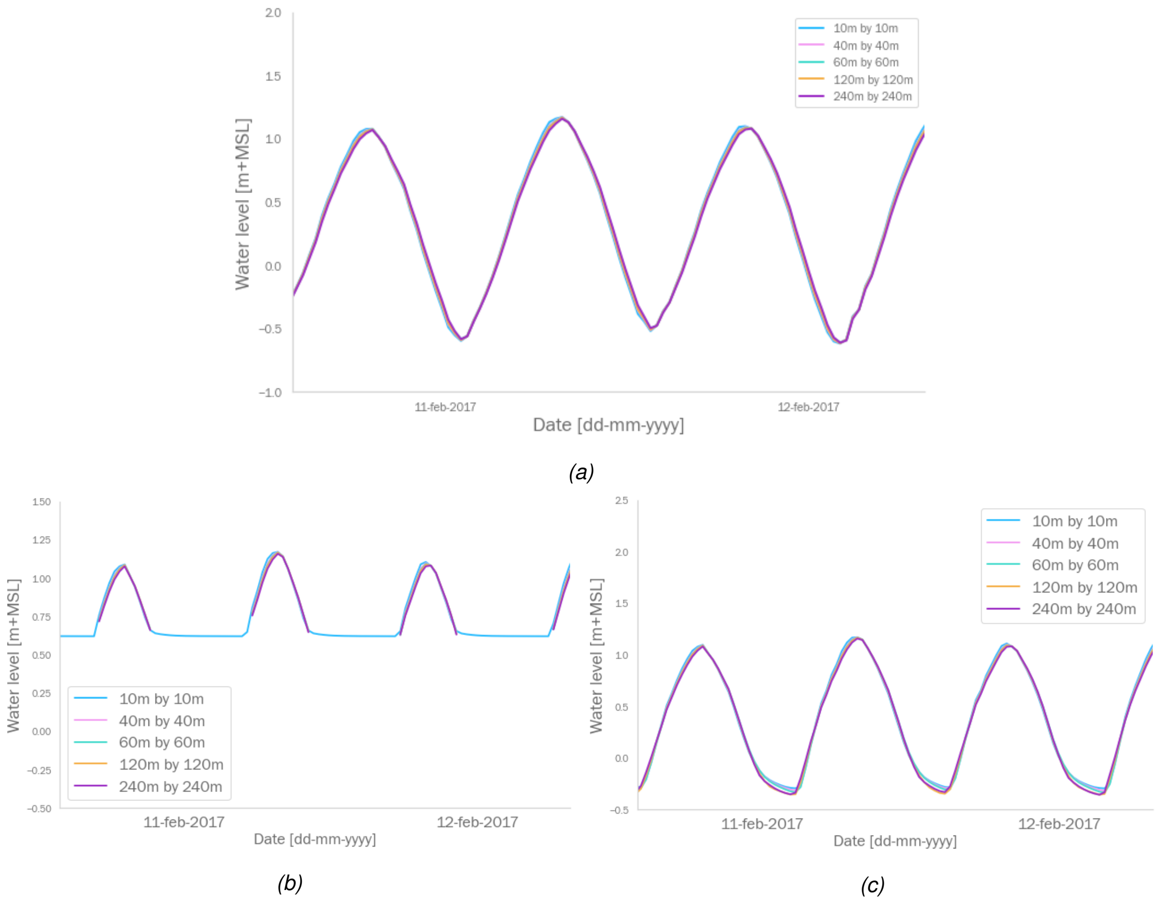

Figure 5.5: Sensitivity analysis of the water levels on varying grid sizes. (a) Location 1 (b) Location 2 and (c) Location 3 in figure 5.4

The sensitivity analysis showed that the water level in the main channel was barely affected by the different computational grid sizes (figure 5.5a). The same results followed from water levels at higher elevated terrain and in the creek system outside of the study area (figures 5.5b and 5.5c).

For cell averaged flow velocities, larger differences can be observed between the different computational grid sizes compared to the water levels. Clear differences can be observed between the maximum ebb and flood flow velocities on a 10 m by 10 m grid compared to 120 m by 120 m and 240 m by 240 m grid sizes (figure 5.6a and 5.6b). Assuming that the 10 m by 10 m grid results in the most accurate flow velocities, it can be seen that 120 m by 120 m and 240 m by 240 m grid sizes are underestimating maximum flood flow velocities. The 60 m by 60 m and the 40 m by 40 m are also slightly underestimating the maximum flood flow velocities, but these grids are simulating the ebb flow velocities quite accurate.

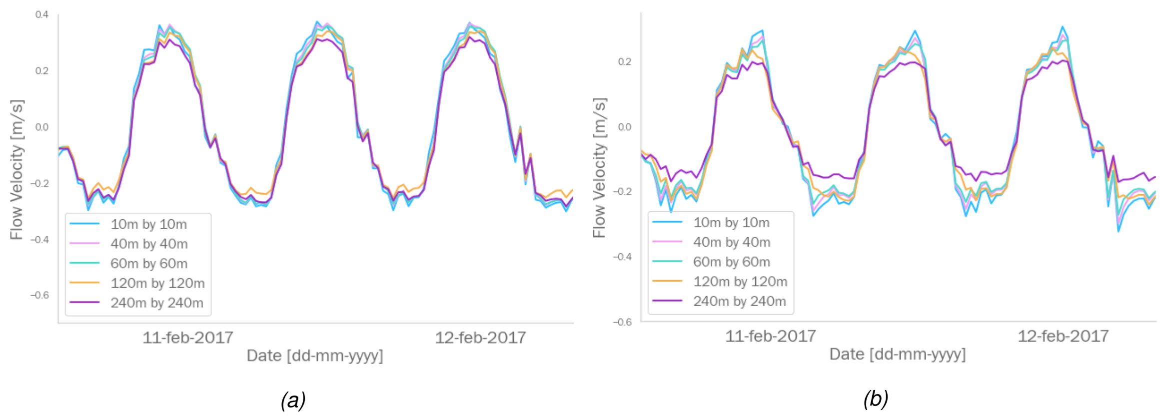

Figure 5.6: Sensitivity analysis of the flow velocities on varying grid sizes. (a) Location 1 and (b) Location 2 in figure 5.4

Next to the accuracy on simulating the flow velocities, computational times are also important to be able to make fast model runs. The simulation using a computational grid of 10m by 10m had a computational time of approximately 6 hours, for a five-day simulation. While all other simulations took approximately 30 minutes, for the same simulation duration. The results of the sensitivity analysis outside the study area and accompanying computational times are summarized in table 5.1.

Grid size $[m]$	Computational time $[h]$	RMSE water level main channel $[m]$	RMSE flow velocity bifurcation $[m/s]$
10 by 10	6.5	0	0
40 by 40	0.49	0.016	0.019
60 by 60	0.46	0.028	0.024
120 by 120	0.45	0.023	0.030
240 by 240	0.45	0.042	0.031

Table 5.1: Sensitivity analysis results outside the study area. RMSE of the different grids is calculated in relation to the 10 m by 10 m grid with equation 4.1 and the computational time is retrieved for a 5 day simulation.

Taking the result of the sensitivity analysis and the computational time of the different computational grid sizes into account, there has been chosen to use a grid size of 40 m by 40 m outside of the study area. This choice has been made to limit the computational cost of the model and still predict accurate flow velocities and water levels outside of the study area.

5.3.2 Computational grid within the study area

As stated earlier, within the study area a smaller grid size will be used to be able to accurately compare model results with measurements. Therefore, grid sizes of 10 m by 10 m, 5 m by 5 m, 2 m by 2 m, and 1 m by 1 m will be tested within the study area. This range is chosen as a grid size smaller than 1 m by 1 m is computationally not possible due to model constraints. On the other hand, choosing a grid size larger than 10 m by 10 m would not make it possible to retrieve model results close to all measurement locations. Therefore, making it harder to compare the modeled hydrodynamics with measured hydrodynamics. The area for which the smaller computational grid size is considered is shown with the blue shaded area in figure 5.4.

The effect of the computational grid on simulated hydrodynamics is monitored at creek station C3 and accompanying forest station F3N (velocity locations 3 and 4 in figure 5.4). These locations have been chosen as it is assumed to be representative for the hydrodynamics in the study area. At these locations only the cell-averaged flow velocities are tested, as from the sensitivity analysis outside the study area it is assumed that the computational grid barely affects the water levels.

The results of the sensitivity analysis show that at creek station C3 the flow velocities simulated by the 10 m by 10 m, 5 m by 5 m, and the 2 m by 2 m are underestimating the flood and ebb maximum flow velocities compared to the 1 m by 1 m grid (figure 5.7a). At forest station F3N the 10 m by 10 m grid and the 2 m by 2 m grid are overestimating the maximum ebb flow velocity, while the 5 m by 5 m grid is underestimating the maximum ebb flow velocity (figure 5.7b). For the sensitivity of the different grid sizes a RMSE has been calculated comparing the different grid sizes to the 1 m by 1 m grid size. Next to the RMSE, the computational times of the different computational grids in the study area are also compared using a grid of 40 m by 40 m outside of the study area. The results are given in table 5.2.

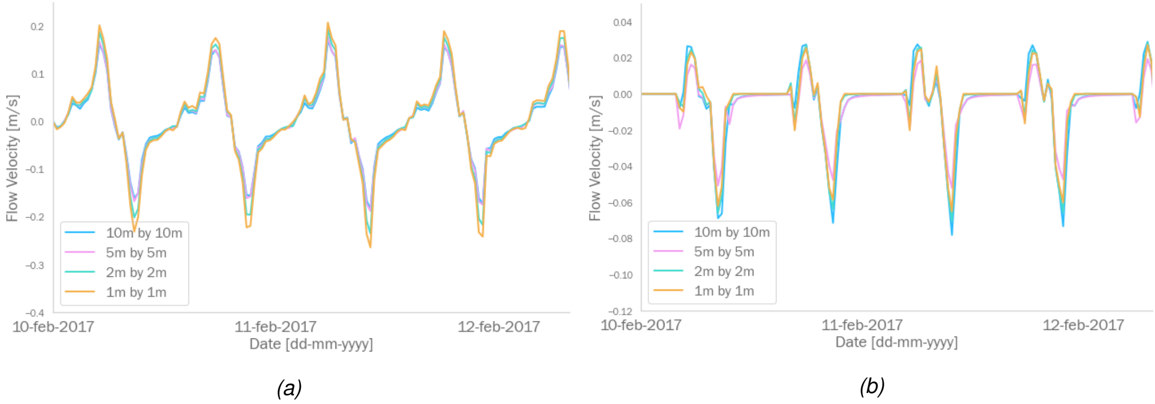

Figure 5.7: Sensitivity analysis of the flow velocities on varying grid sizes. (a) Location 3 and (b) Location 4 in figure 5.4

Grid Refinement Size $[m]$	Computational time $[h]$	RMSE C3 $[m/s]$	RMSE F3N $[m/s]$
1 by 1	57	0	0
2 by 2	4.5	0.009	0.002
5 by 5	1.5	0.02	0.004
10 by 10	0.75	0.025	0.006

Table 5.2: Sensitivity analysis results of the computational grid in the study area. RMSE calculated using equation 4.1. The computational time is retrieved for a 5 day simulation.

From this analysis a computational grid of 5 m by 5 m is chosen in the study area. As this computational grid size results in acceptable computational times and still simulates accurate flow velocities in the creek and forest. The computational grid used in the model domain is shown in figure 5.8.

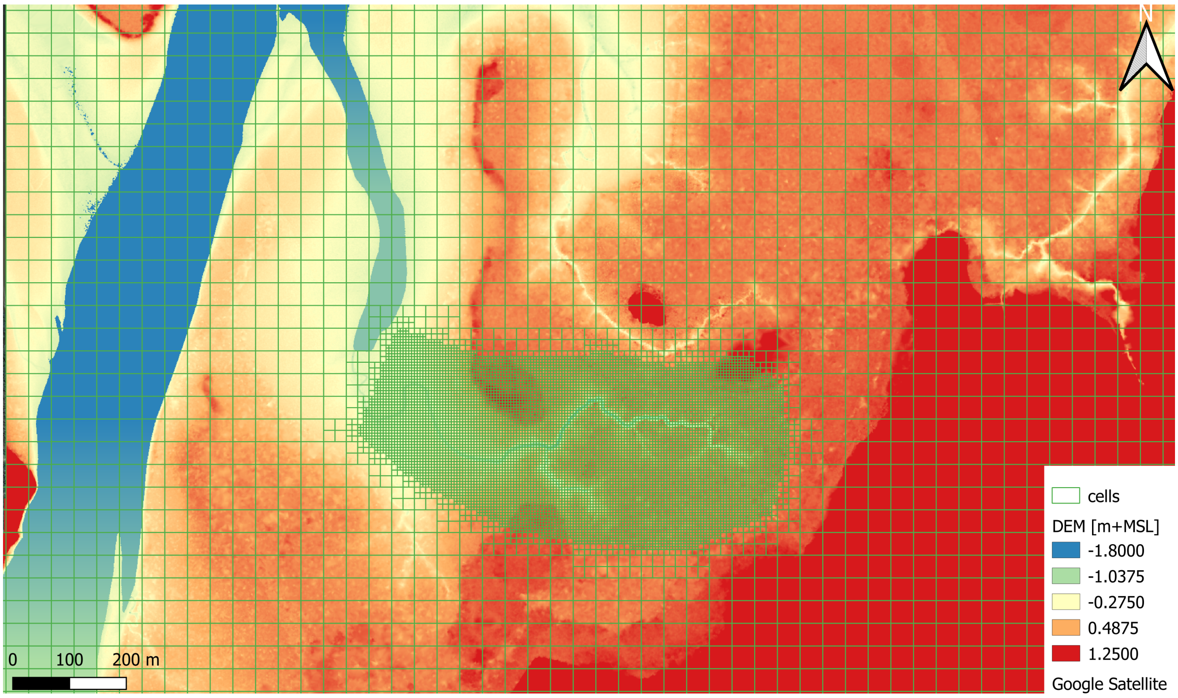

Figure 5.8: Computational grid used in the hydrodynamic model of the Whitianga estuary.

5.4 Boundary Conditions

The boundary condition forces the hydrodynamics within the whole model domain. For the tidal dynamics in the study area, it is crucial that the correct volume of water arrives at the beginning of the mangrove creek system through time. As there are no measurements available at the model domain boundary, calibration of the input boundary condition is needed.

The model boundary is located in between two water level measurement stations, one at the entrance of the estuary, measured at the harbour of Whitianga, and one at the entrance of the study area at creek station C0 measured by Horstman et al. (2021). These two data sets are used to design the input boundary conditions at the model boundary. This has been done by varying the fractional influence of both water level time series and afterwards comparing the measured water level time series at creek station C0 with the modeled water level at station C0. The calibration procedure is continued till the maximum deviation between the modeled and measured HWL and LWL are within 2 cm.

A short calibration procedure resulted in using 100 percent of the C0 time series and 0 percent of the Whitianga harbour time series. Using this fractional influence the measured and modeled water level time series' HWL and LWL were within the set limits. The simulated water level time series at C0 after calibration is shown in figure 5.9

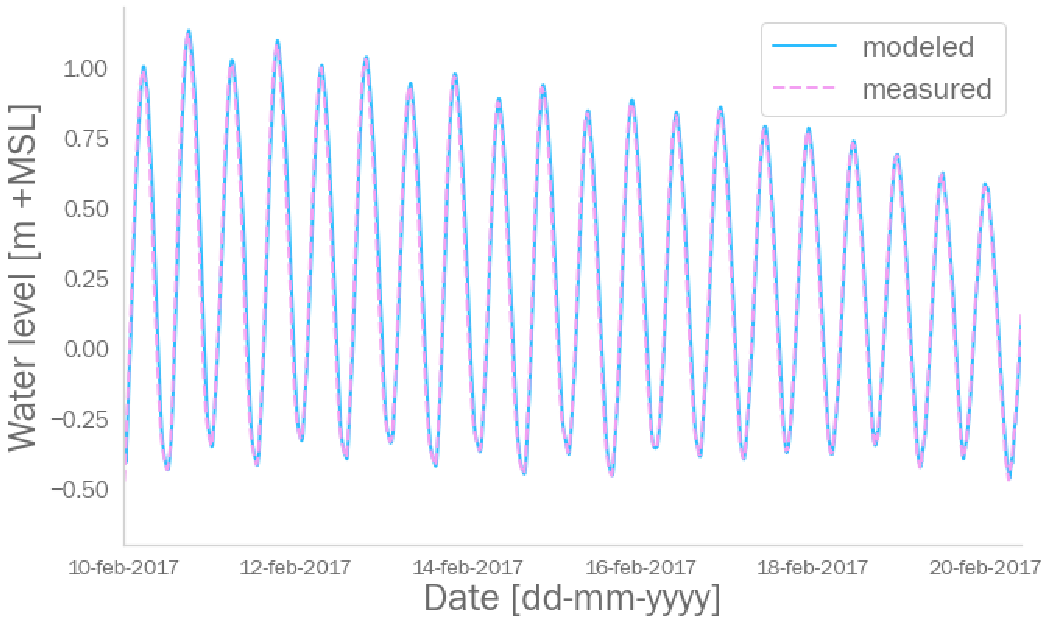

Figure 5.9: Modeled and measured water level time series after calibration of the boundary condition, retrieved at creek station C0

5.5 Base-case simulation

Two base-case simulations have been performed. The first simulation including the subgrid technique. The second, simulation excluding the use of subgrid. This is done to show the added value of using the subgrid modeling technique. Removing the subgrid modeling technique will imply that the bathymetry is averaged over the computational grid as explained in section 2.4.1, resulting in an uniform elevation in a computational cell. The simulations are performed for an entire spring-neap tidal cycle.

The effect of the subgrid modeling technique can clearly be seen when looking into the water level time series for creek stations C5 and C6. At creek stations C5 and C6 the creek narrows to a width between one and two meter surrounded with higher elevated areas. With the use of subgrid-based modeling a pretty good simulation of reality can be achieved. But when DEM averaging is applied, the elevation in a computational cell is averaged which causes that the bathymetry of the creek totally disappears, causing that the water level cannot drop as far as observed in the measurements. This is clearly shown in figure 5.10.

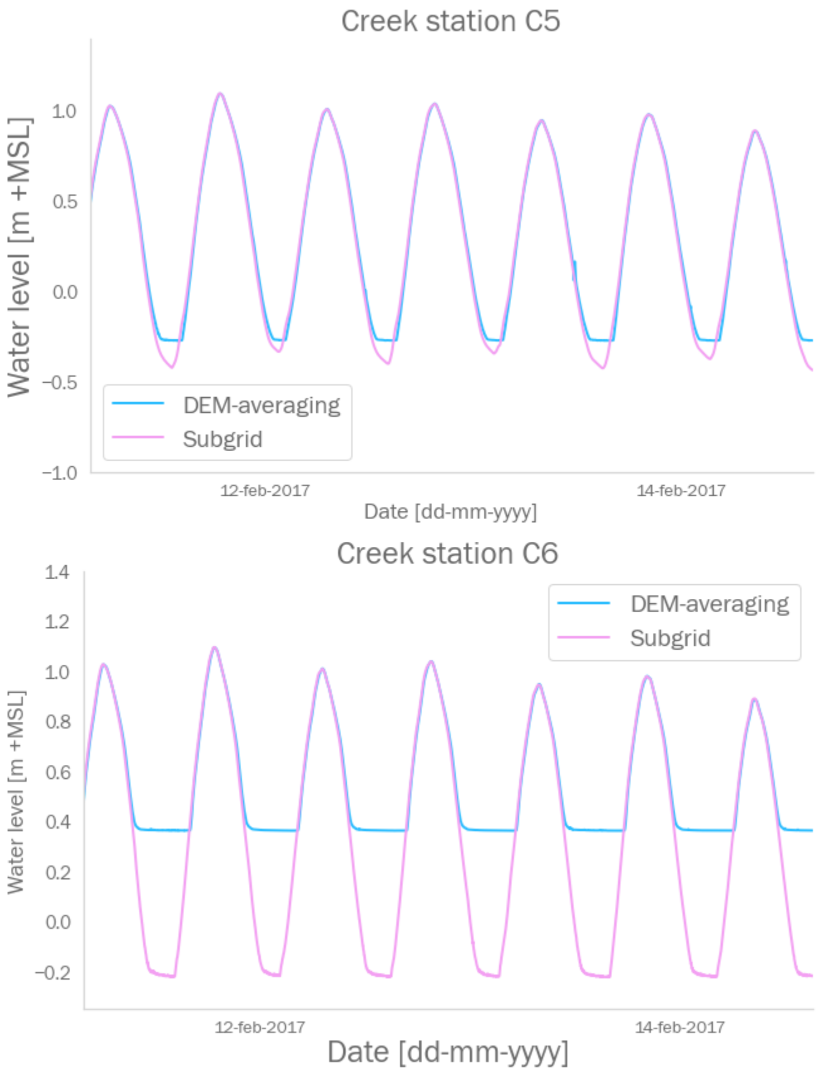

Figure 5.10: Comparison of the water level at creek stations C5 and C6 between a simulation including subgrid and a simulation excluding subgrid

The subgrid method also has large effect on the modeled flow velocities in the area. An example of the effect is shown figure 5.11. This effect is especially visible at within-creek water levels. Removing the subgrid from the simulation creates instabilities in the modeled flow velocities, as shown in figure 5.11. This is caused by large variations in bed elevation between different computational cells in the creek bed.

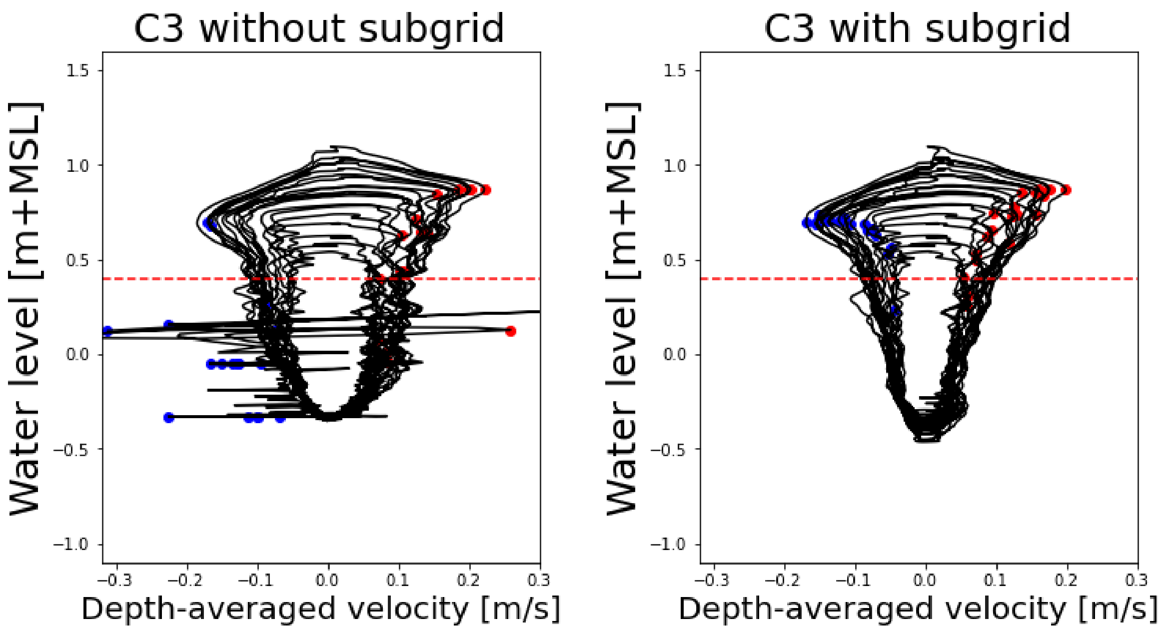

Figure 5.11: Comparison of the tidal flow-stage curves of a simulation including subgrid and a simulation excluding subgrid

Concluding from the two examples shown above, it is important to use the subgrid modeling technique when modeling an intertidal area with a strong varying bathymetry. If the subgrid modeling technique is excluded from the simulation, spatial variance in the bathymetry is lost. Which directly affects the simulated hydrodynamics in the area by destabilizing the within-creek flow velocities and causing that the creek is drained at higher elevation at station C5 and C6. The base-case including subgrid will be used in the validation of the vegetation representations. Therefore, the complete set of results for the base-case simulation used in the validation can be found in appendix B.

Chapter 6

Vegetation Representations

6.1 Roughness raster

The first vegetation representation that will be added to the base-case hydrodynamic model, is a roughness raster. To define the roughness raster a distinction is made between three areas: The deeper channel and beginning of the creek system, the inner creek area between creek stations C2-C6, and the forest platform. This distinction is based on the computed representative roughness values by Horstman et al. (2021). As no clear distinction between vegetated forest platform and creek bed is available in the measurements, it is assumed that locations of the creek bed can be recognised by the bed level. Therefore, the creek bed roughness is assumed at elevations below -0.1 m+MSL and vegetated forest platform elevation is assumed at elevations higher than -0.1 m+MSL.

Base values for the roughness raster and ranges for calibration are set based on the computed drag coefficients by Horstman et al. (2021) combined with literature (Mazda' et al., 1995; Stark et al., 2015). From this, a base roughness raster is set-up with Chézy roughness of 60 [$m^{1/2}s^{-1}$] in the deeper channel and in the whole creek system, and 2 [$m^{1/2}s^{-1}$] in the forest. This base roughness raster will be used for the first calibration run (figure 6.1).

Figure 6.1: Base roughness raster with a Chézy roughness of 60 [$m^{1/2}s^{-1}$] in the creek (white) and a Chézy roughness of 2 [$m^{1/2}s^{-1}$] in the forest (black)

6.1.1 Roughness raster calibration

The calibration ranges used for the roughness raster are given in table 6.1. The Chézy value for the deep channel + creek system between station C0 and C2 is kept constant during the calibration procedure. This choice is made to ensure that the correct tidal wave enters the area, as this roughness is used in the calibration of the forcing boundary condition. The calibration procedure used, is explained in section 1.4.

Location	Range of Chézy values [$m^{1/2}s^{-1}$]
Deep channel + creek between station C0 and C2	60
Creek between station C2 and C6	10-60
Forest platform	2-20

Table 6.1: Chezy roughness calibration ranges defined with roughness values found in Horstman et al. (2021), Mazda' et al. (1995) and Stark et al. (2015)

The Chézy values used in the different calibration runs can be found in table 6.2. The deviation for the LWL and HWL at the creek stations can be found in table 6.3. After six calibration simulations, the exit criterion of a mean deviation of 5 cm was reached, at the sixth run the mean deviation in HWL and LWL was 5.36 cm. The best performing run was with a Chézy value of 10 [$m^{1/2}s^{-1}$] in the inner creek (C2-C6) and a Chézy value of 5 [$m^{1/2}s^{-1}$] on the vegetated forest platform. This roughness raster will be used in the validation of the vegetation representation.

Calibration Run	Chézy creek (C2-C6) [$m^{1/2}s^{-1}$]	Chézy forest [$m^{1/2}s^{-1}$]
1	60	2
2	60	5
3	60	10
4	60	20
5	30	20
6	10	5

Table 6.2: Deviations between modeled and measured HWL and LWL using a roughness raster at creek station C0 and C5

Calibration Run	Mean deviation in HWL [m]	Mean deviation in LWL [m]	Mean deviation total [m]
1	0.0602	0.0533	0.0568
2	0.0568	0.0550	0.0559
3	0.0549	0.0555	0.0552
4	0.0667	0.0529	0.0598
5	0.0549	0.0541	0.0545
6	0.0624	0.0449	0.0536

Table 6.3: Mean deviation of HWL and LWL over every tidal cycle at all creek stations (C0-C6)

6.1.2 Results and comparison to measured characteristics

The results will be presented following the order of the competences from chapter 4. First looking into the modeled tidal flow-stage curves (figure 6.2).

Tidal flow-stage curves

The water levels at which maximum flow velocities occur within the creek show a slight inland increase from C0 till C4. Where maximum flow velocities at station C0 and C1 occur mostly within-creek water levels. Further inland, at station C2-C5, maximum flow velocities occur at over-bank water levels (figure 6.2). Additionally, at station C2-C5 maximum flood flow velocities occur at increasingly HWL. While, the maximum ebb flow velocities occur at consistent over bank water level elevations.

Comparing the modeled to the measured tidal flow-stage curves, roughly the same form can be observed at the different stations. A difference between the measured and the modeled curves, is that at station C2 the maximum ebb flow velocity is occurring at over-bank water levels, while at the measured tidal flow-stage curve the maximum flow velocity is occurring at within-creek water levels. Another difference compared to the measured tidal flow-stage curves, is that at station C6 the peak ebb flow velocities occur at within-creek water level while at the measured tidal flow-stage curve the maximum ebb flow velocity is consistently occurring at over-bank water levels.

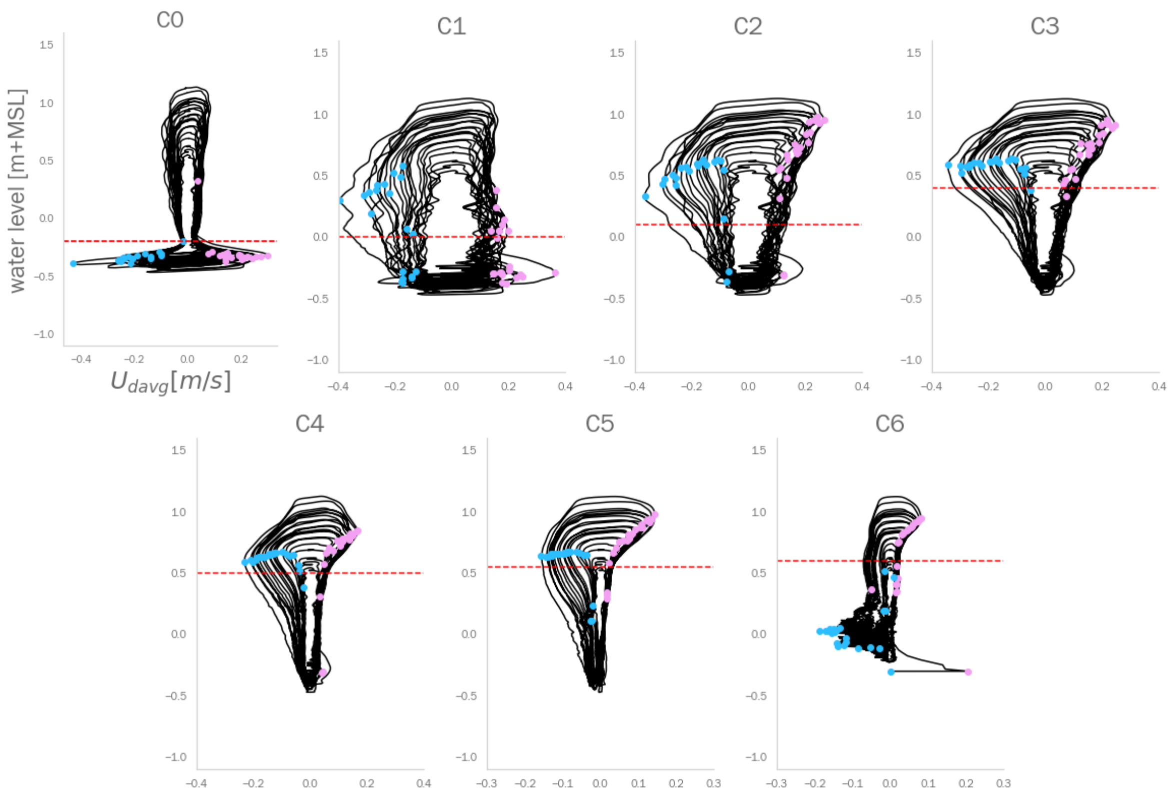

Figure 6.2: Simulated tidal flow-stage velocity curves for all creek stations, blue and pink dots indicate maximum ebb and flood tidal velocities during each individual tide. Modeled using a roughness raster.

Tidal duration asymmetry

The model results show a clear tidal duration asymmetry, where the duration of the falling tide is larger than the duration of the rising tide (figure 6.3). A parabolic trend can be observed in the asymmetry with increasing HWL. The peak of the parabole is around 1 m+MSL. This trend is observed for all creek stations except for station C6. At station C6 the same duration asymmetry as compared to the other creek stations can be found, but the asymmetry is larger and less affected by the HWL compared to other creek stations.

Comparing the modeled duration asymmetry to the measured duration asymmetry (figure 6.3 in grey), it can be found that overall the modeled duration asymmetry is smaller and has less dispersion than the measured duration asymmetry. Next to this, the modeled asymmetry decreases faster than the measured asymmetry for HWL larger than 1 m+MSL.

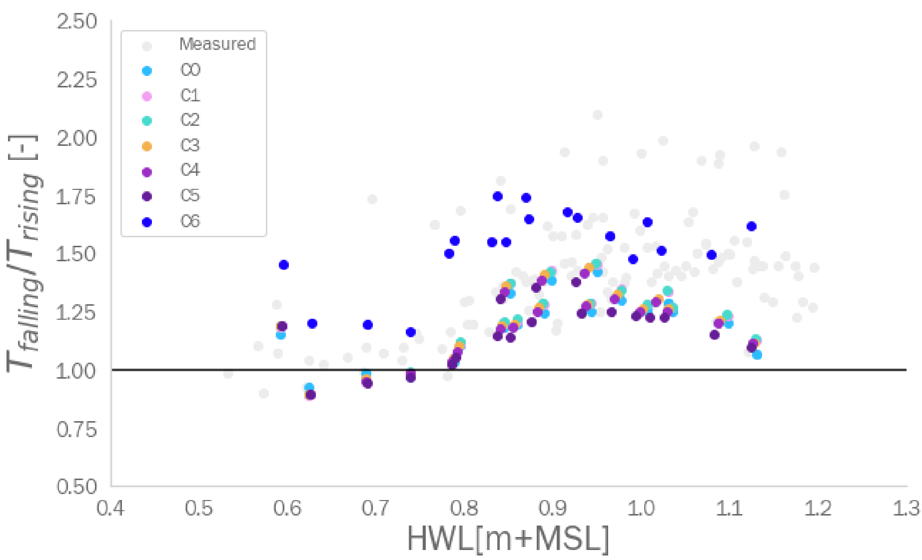

Figure 6.3: Duration asymmetry of the simulated tidal dynamics at the creek stations. Modeled using a roughness raster

Along creek delay of the LWL

The modeled and the measured along creek delay of the LWL is shown in figure 6.4. The along creek delay is measured in relation to the arrival of the LWL at creek station C0. The modeled along creek delay of the LWL is consistently smaller than the measured delay. The difference stems mainly from the delay in between station C0-C2, where the model did highly underestimate the delay. In between station C2-C6 the propagation velocity (gradient of line in figure 6.4) is comparable to the measured propagation velocity. In both the measured and the modeled along creek delay, a large increase in delay between station C5 and C6 can be found. This decrease caused that the rising tide caught up with the falling tide resulting in a more asymmetrical tide compared to station C0 (figure 6.3 and A.7).

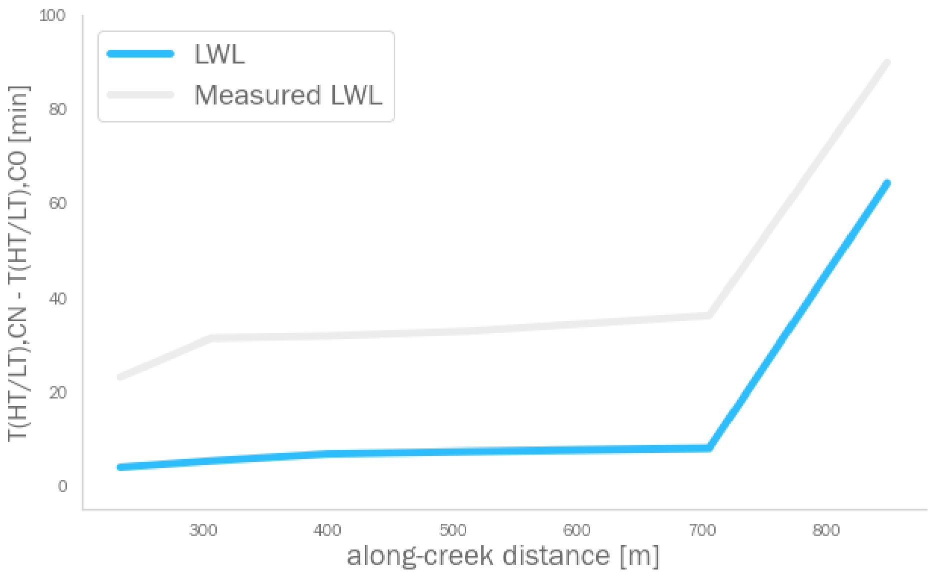

Figure 6.4: Along creek delay of the LWL, modeled using a roughness raster

Maximum flow velocities

The modeled flow velocities in the creek station are a factor 3 to 6 times larger than flow velocities in the corresponding forest station (figure 6.5). At creek station C3 a maximum flow velocity of 0.3 m/s was reached during ebb tide and a maximum of 0.22 m/s was reached during flood tide. At the corresponding forest station, F3N, flow velocities of 0.05 were reached during ebb tide and flow velocities of 0.08 m/s were reached during flood tide.

Comparing the modeled maximum flow velocities to the measured maximum flow velocities, it can be found that the model is consistently underestimating the maximum flow velocities in the creek and the forest. In the creek the underestimation is larger for ebb tide compared to the flood tide, while in the forest the underestimation of flood and ebb maximum flow velocities is comparable.

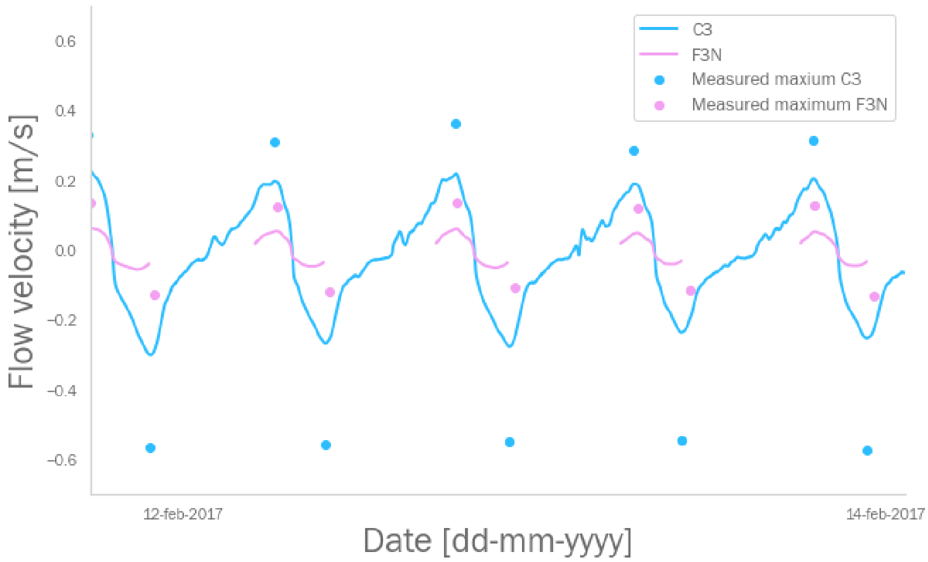

Figure 6.5: Flow velocity in creek station C3 and concurring forest station F3N, modeled using a roughness raster

Tidal flow velocity asymmetry

Next to the difference in maximum flow velocity in the creek and the forest, a tidal velocity asymmetry during each tide can be observed (figure 6.6 and 6.7). Figure 6.6 shows that the flow velocities in the forest are predominantly flood dominant. Some trends can be observed when looking at the individual stations. Station F2N shows a decreasing dominance with increasing HWL. While station F3N and F4N are not affected by increasing HWL, the flood dominance in stations F5N and F6N is decreasing with increasing HWL. Comparing the modeled with the measured tidal asymmetry at the forest stations, it can be found that apart from the difference in HWL the modeled asymmetry is quite comparable to the measured asymmetry. The only difference in asymmetry, is that the model simulates an ebb dominance for more tides than measured.

Figure 6.7 shows the tidal velocity asymmetry at the creek stations. In the creek stations an ebb dominant pattern is observed, with a slight increase in asymmetry with increasing HWL. Only for station C6 this trend does not hold. At station C6 the flow is ebb dominant with no increase with increasing HWL. Station C0, C1 and C2 are the least ebb dominant creek stations, showing that even at higher HWL still part of the tidal cycles are flood dominant. Comparing the modeled asymmetry to the measured asymmetry, it can be observed that especially for larger HWL the model is underestimating the asymmetry. Next to this, the model simulates for some tides an flood-dominance which is not measured. This is especially for creek station C0, C1, and C3 where the model simulates predominantly a flood dominance for small HWL.

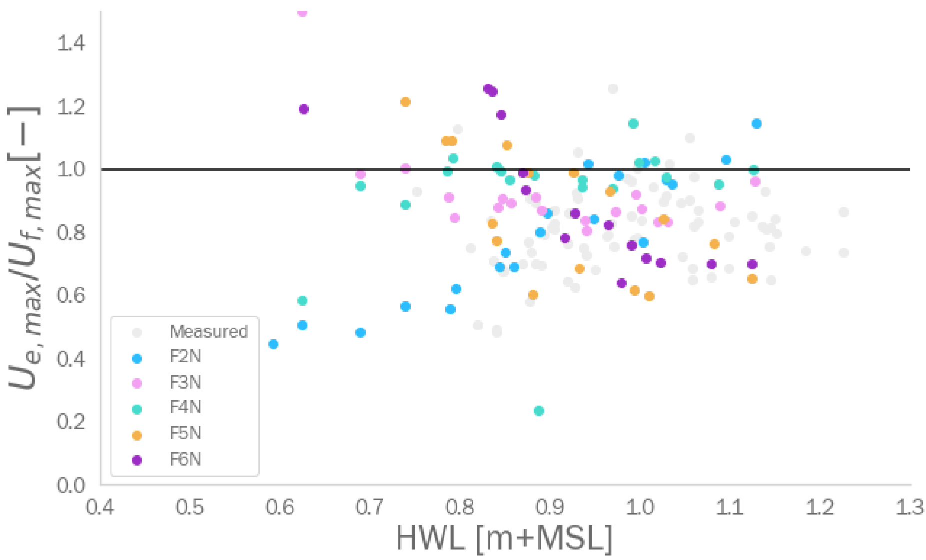

Figure 6.6: Ratio between simulated maximum ebb and flood flow velocity at the forest stations using a roughness raster

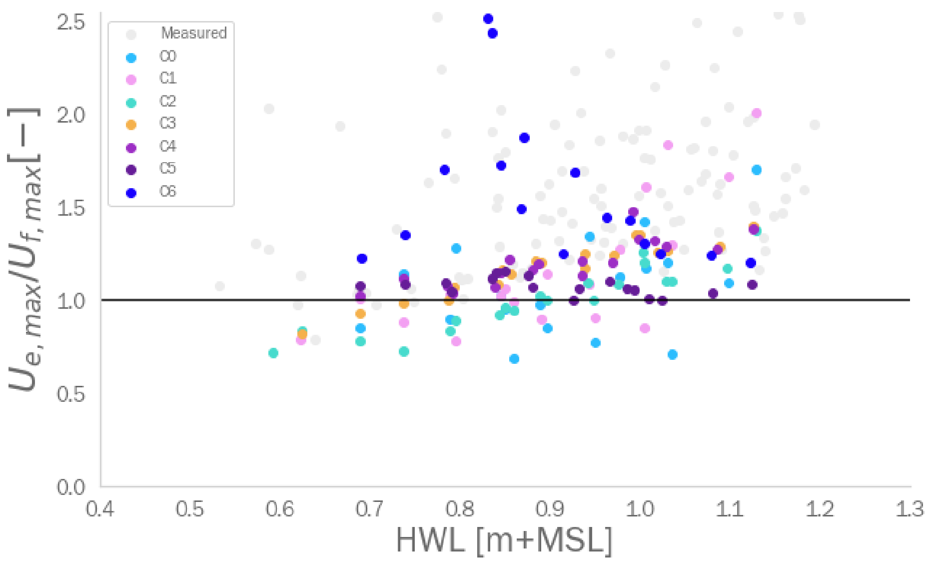

Figure 6.7: Ratio between simulated maximum ebb and flood flow velocities at the creek stations using a roughness raster

6.2 Interflow layer

The parameter values for the interflow layer are chosen according to measured characteristics in the area. The interflow layer is defined by the type of interflow, porosity, the hydraulic conductivity, the interflow layer height. To run the model, the roughness, which is now at the interface between the interflow layer and the traditional surface water layer, is defined to account for canopy-scale turbulence.

For reasons explained in section 2.4.2, the storage in the interflow layer is based on the porosity and the water depth. The interflow layer height is defined to the lowest elevation in the computational cell (interflow type 3). To get the porosity value in the interflow layer, the measured solid volume fraction is subtracted from 1 (table 3.1). Next to the measured density an extra artificial density is added to account for the larger avicennia marina trees and their leaves. This resulted in a base porosity value of 0.90 in the forest. In the back of the creek, between creek stations C2-C6, a small decrease in porosity is added to account for the steep banks with root systems shown in figure 3.2d. Therefore, in the inner creek a porosity value of 0.98 is chosen. In the main channel, a value for the porosity of 1 is set as no vegetation is present in this area.

The hydraulic conductivity is computed using equation 2.8. By dividing the discharge through the cross-sectional area, the hydraulic conductivity can be calculated knowing the flow velocity and the water level gradient. The hydraulic conductivity is calculated apart for the creek and for the forest. In the creek, the average flow velocity measured in the creek stations is used and the water level gradient over the creek is used. In the forest, the average flow velocity measured at the forest stations north of the creek and the water level gradient over the forest is used. This resulted in the hydraulic conductivity values given in table 6.4.

The height of the interflow layer is 0.2 m. This is based on the pneumatophore height in the study area. A constant artificial height is added to increase the effect of the interflow layer. As the interflow layer is defined 'below the surface', the whole DEM is elevated with the height of the interflow layer. This ensures that the impervious layer remains at the correct elevation. At last, the values for the roughness have been set to take into account the canopy-scale turbulence. As no earlier research converted canopy-scale turbulence into Chézy roughness, roughness values for the creek and forest are assumed using the knowledge obtained from applying the roughness raster. The base values for the key parameters of the interflow layer are listed in table 6.4.

Parameter	Domain wide value	Channel value	Inner creek value (C2-C6)	Forest platform value
Porosity [-]	-	1	0.98	0.90
Hydraulic conductivity [m/s]	-	4166.67	4166.67	333.33
Height [m]	0.2	-	-	-
Roughness [$m^{1/2}s^{-1}$]	-	60	40	20

Table 6.4: Model settings for the model with an interflow layer

6.2.1 Calibration

For the calibration of the interflow layer, the same calibration procedure as for the roughness raster is used. For calibration, the porosity, the hydraulic conductivity, and the depth of the interflow layer will be used. As these three parameters are assumed to have the most influence on the simulated hydrodynamics.

Calibration run	Porosity creek	Porosity forest	HC forest [m/s]	HC creek [m/s]	Height interflow [m]
1	0.98	0.9	333.33	4166.67	0.2
2	0.931	0.855	333.33	4166.67	0.2
3	0.882	0.81	333.33	4166.67	0.2
4	0.588	0.54	333.33	4166.67	0.2
5	0.882	0.855	208.33	4166.67	0.2
6	0.588	0.54	208.33	4166.67	0.2
7	0.588	0.54	208.33	4166.67	0.5
8	0.882	0.54	208.33	4166.67	0.5

Table 6.5: Calibration parameter values for the interflow layer

In table 6.5 the parameter settings of the calibration runs are given. As in the first four runs the maximum water level prediction did not show significant improvement on changes in porosity (table 6.6), the hydraulic conductivity and interflow layer depth were changed in the remaining calibration runs. Decreasing the hydraulic conductivity of the forest did not significantly affect the water levels with respect to calibration run three and four, which uses the same porosity. Therefore, the depth of the interflow layer was increased in run seven and eight to a depth of 50 cm.

The overall mean deviation given in table 6.6, shows that the calibration procedure did not significantly improved the results for the overall deviation in HWL and LWL. Therefore, the first calibration run will be used in the further analysis of the interflow layer. The first calibration run has been chosen as the parameter values used in this calibration run are based on the measurements in the area and are therefore the most representative for the functioning of the interflow layer in mimicking the effect of vegetation observed in the area.

Calibration Run	Mean HWL [m]	Mean LWL [m]	Mean total [m]
1	0.058	0.080	0.069
2	0.057	0.080	0.068
3	0.057	0.080	0.068
4	0.056	0.079	0.067
5	0.058	0.079	0.068
6	0.056	0.079	0.067
7	0.058	0.079	0.068
8	0.061	0.079	0.070

Table 6.6: mean deviation of HWL and LWL for every tidal cycle at all creek stations

6.2.2 Results and comparison to measured characteristics

The results of the hydrodynamic model with an interflow layer will be presented following the order of the competences set-up in chapter 4.

Tidal flow-stage curves

The water levels at which maximum creek flow velocities occur, are at approximately constant water levels for station C2-C6. Maximum flow velocities at station C2-C6 occur mostly at over-bank water levels (figure 6.8). At creek stations C2-C4 and C6 the ebb-flow velocity occurs at constant water levels while water levels increase for flood flow velocities.

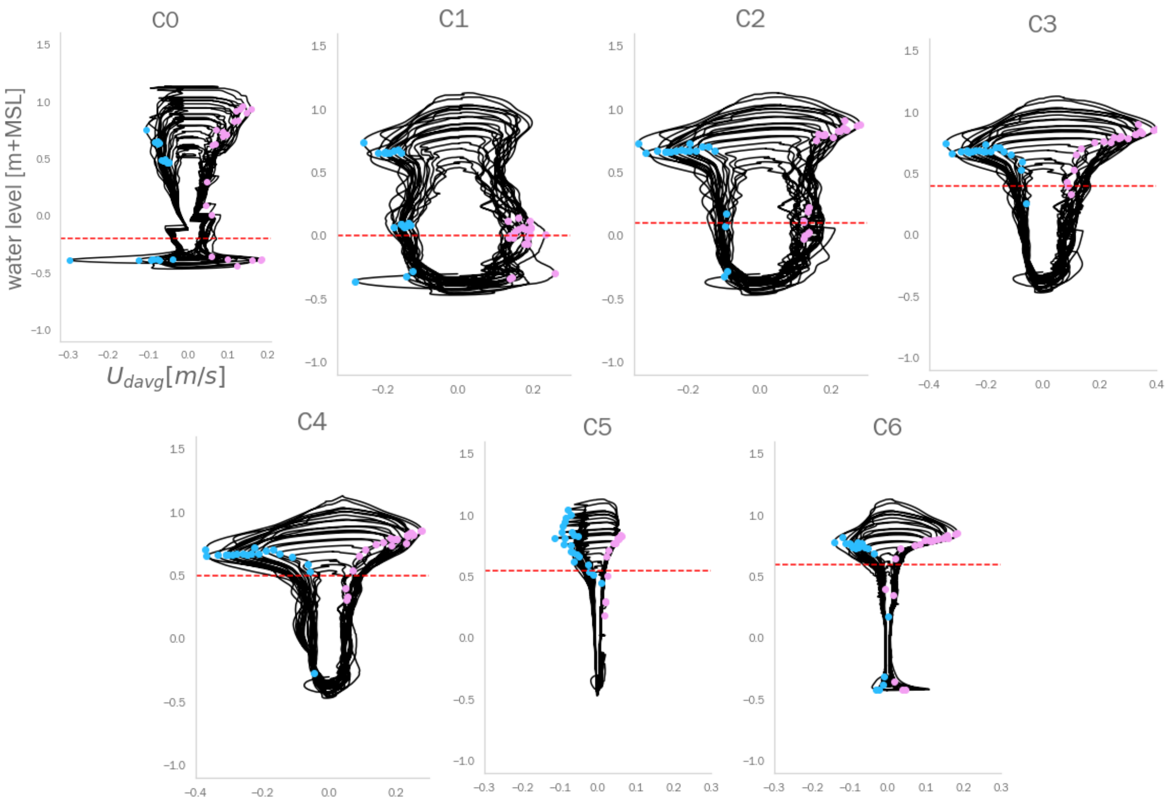

Figure 6.8: Simulated tidal flow-stage velocity curves for all creek stations, blue and pink dots indicate maximum ebb and flood tidal velocities during each individual tide. Modeled using an interflow layer

Comparing the modeled to the measured tidal flow-stage curves, it can be found that for most stations the overall form of the tidal flow-stage curve is comparable to the measured form. At stations C0, C1, and C2 a difference can be found in the water level where maximum flow velocities occur compared to the measured curves. In the measured tidal flow-stage curves the maximum flow velocities occur at within-creek water levels, while at the modeled curves the flow velocity occur predominantly at over-bank water levels. At station C5, the maximum ebb flow velocities occur at increasingly HWL. This is different than in the measured tidal flow-stage curve, where the measured maximum ebb flow velocity occurs at a constant just over-bank water level.

Tidal duration asymmetry

The duration asymmetry observed at the different creek stations is increasing with HWL till a HWL of 1.0 m+MSL afterwards the asymmetry is decreasing (figure 6.9). When comparing the different creek stations during one tide, no significant variation in asymmetry can be found. Comparing the modeled to the measured duration asymmetry, a clear difference can be found comparing the different creek station during one tide. In the measured duration asymmetry large differences can be found comparing the station, while the modeled duration asymmetry at the different stations is very compact. Additionally, for HWL above 1 m+MSL the modeled asymmetry decreases faster than the measured asymmetry, which only slightly decreases.

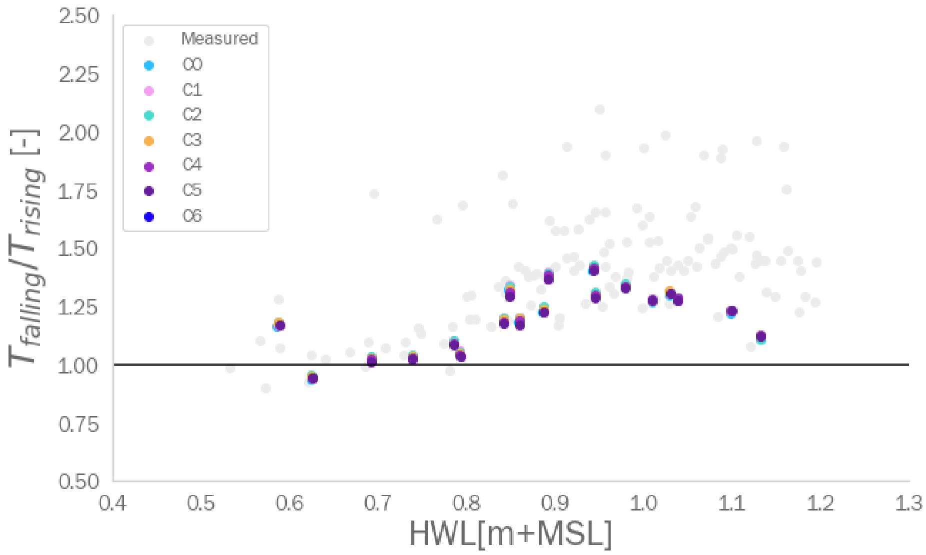

Figure 6.9: Duration asymmetry at the creek stations using an interflow layer

Along creek delay of the LWL

The along creek delay in arrival of the LWL compared to creek station C0 is shown in figure 6.10. The along creek propagation velocity (the gradient of the line in figure 6.10) of the LWL is almost constant over the whole creek with a slight decrease in propagation velocity in between creek station C5 and C6. The LWL peaks travel from station C0 to station C6 in less than 15 minutes. A large difference in delay can be observed when comparing the modeled along creek delay with the measured.

The model simulated smaller along creek delays compared to the measurements. Additionally, the decrease in propagation velocity in between stations C5 and C6 is smaller than the measured decrease in propagation velocity.

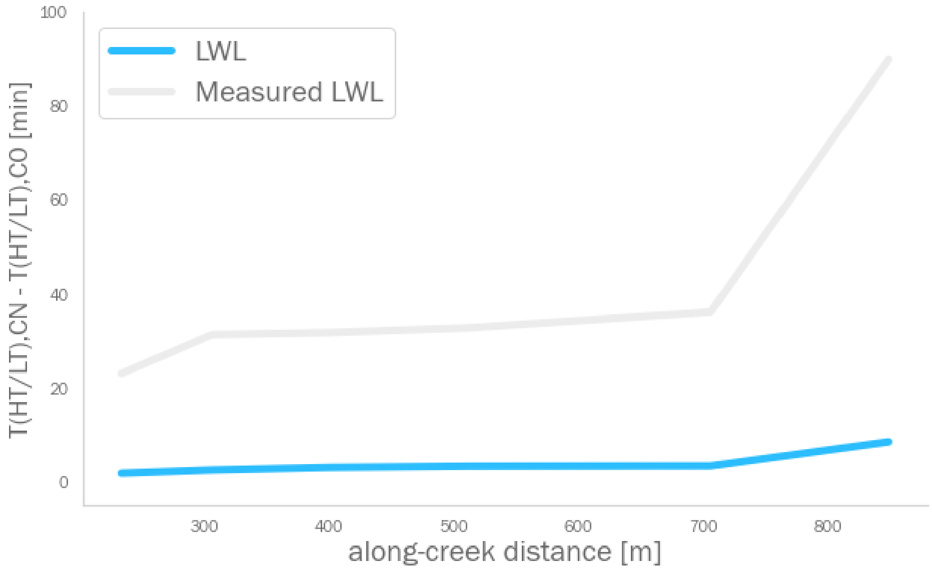

Figure 6.10: Along creek delay of tidal low- water levels using an interflow layer

Maximum flow velocities

The flow velocities in the creek are 2-3 times larger than at the corresponding forest station. The flow velocities in the creek (creek station C3) reach a maximum velocity of 0.3 m/s during flood tide and 0.22 m/s during ebb tide. In the forest (forest station F3N), the flow velocity maxima are 0.13 m/s during flood tide and 0.12 m/s during ebb tide (figure 6.11). When comparing the flow velocities in the modeled flow velocities to the measured flow velocities at station C3, it can be observed that the flood flow velocity maxima are simulated quite accurate. But, the maximum ebb flow velocities are highly underestimated by the model. For forest station F3N, the model quite accurately simulated the maximum ebb and flood flow velocities.

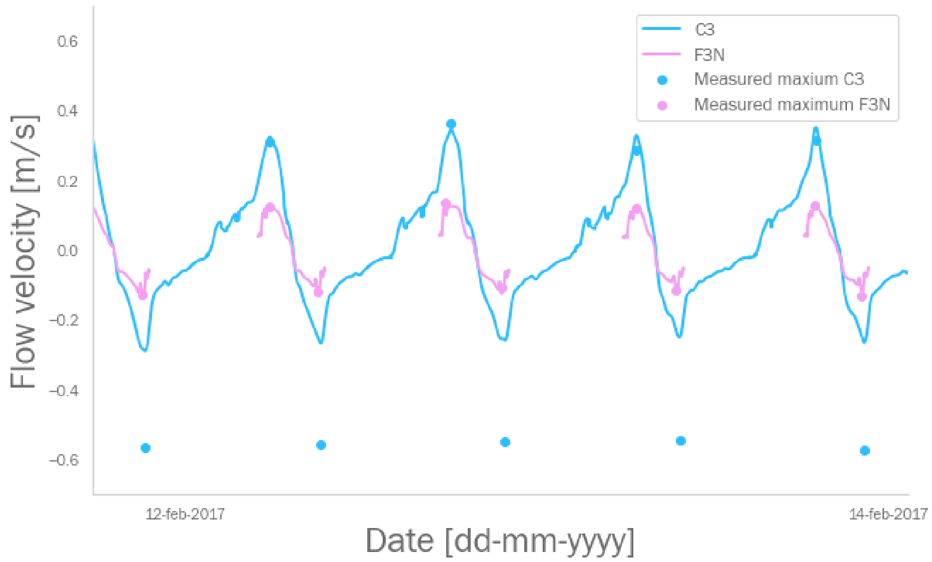

Figure 6.11: Modeled flow velocities at stations C3 and F3N, using an interflow layer

Tidal flow velocity asymmetry

When comparing the maximum flow velocities during ebb tide with the maximum flow velocities during flood tide in one tidal cycle, an asymmetry can be found in the creek stations as well as in the forest stations (figure 6.12 and 6.13). Creek stations C0, C3, and C6 show a flood flow velocity dominant pattern, not significantly affected by the HWL. Creek stations C2, C4, and C5, show an ebb flow velocity dominant asymmetry slightly increasing with HWL for creek stations C2 and C4 and rapidly decreasing for creek station C5. This pattern is different than the measured pattern, where an ebb dominant pattern was observed (shown in grey in figure 6.12). The modeled and the measured asymmetry show almost no comparison.

At the forest stations, a mainly flood dominant pattern can be observed (figure 6.13). Except for stations F4N and F6N, which show predominantly an ebb dominance. Station F2N shows a decreasing flood dominance with increasing HWL, while stations F3N and F5N show an increasing flood dominance with increasing HWL. Comparing the modeled tidal velocity asymmetry with the measured asymmetry, a comparable dominance is found. Although, the measurements show a flood dominance for all stations, while the modeled asymmetry does not show a flood dominance for station F4N and F6N.

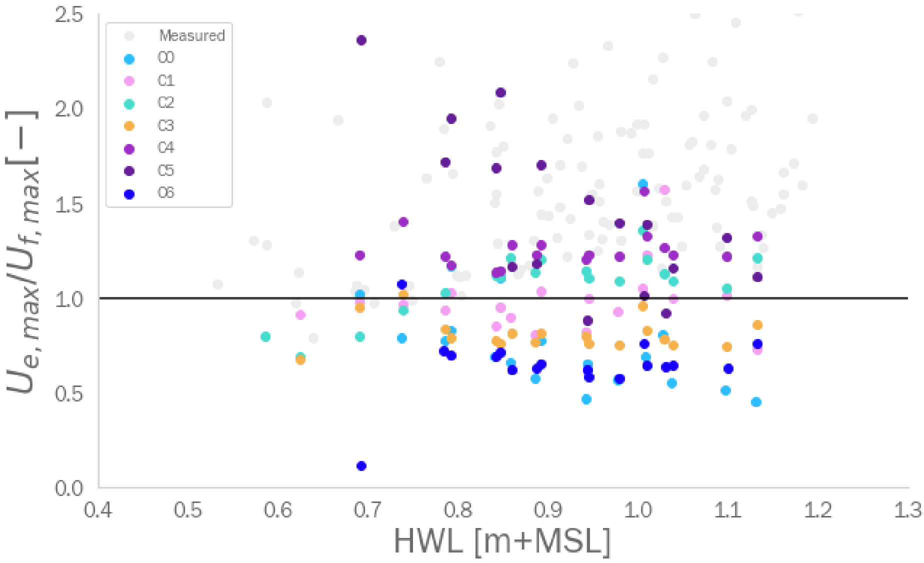

Figure 6.12: Ratio between maximum ebb and flood flow velocity at the creek stations, modeled using an interflow layer

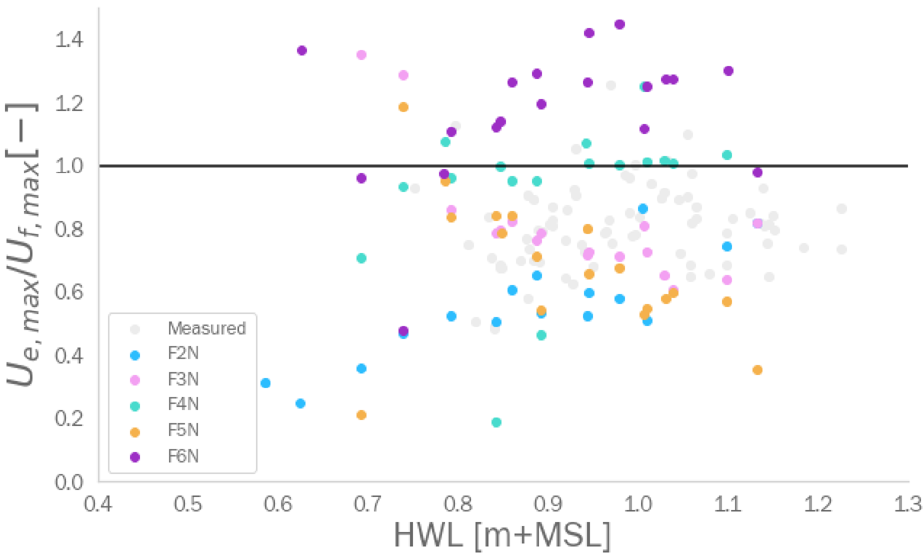

Figure 6.13: Ratio between maximum ebb and flood flow velocities at the forest stations, modeled using an interflow layer

6.3 Evaluation of vegetation representations

To evaluate the functioning of the two vegetation representations, they will be tested on the five competences defined in chapter 4. The base-case model including sub-grid has also been tested on the different competences. The results of the base-case simulation can be found in appendix B.

The first competence focused on qualitative comparison of the tidal flow-stage curves on certain measured characteristics. The tidal flow-stage curves of the base-case, roughness raster, and the interflow layer are given in figures B.6, 6.2, and 6.8. To qualitatively compare the tidal flow-stage curves with the measured curves, the checklist defined in chapter 4 is used. The results are given in table 6.7.

	Base-case	Roughness Raster	Interflow
Max flow velocity at in-creek water level at station (C0,C1)	Yes	No	No
Max ebb flow velocity at constant water level (C3-C5)	Yes	Yes	No
Max ebb flow velocity at just over bank water level (C3-C5)	No	Yes	Yes
Increasing max flow velocity with increasing HWL (C3-C5)	No	Yes	No

Table 6.7: Checklist qualitative comparison tidal flow-stage curves

In figure B.6 the tidal flow-stage curves of the base-case simulation are shown. In the flow-stage curves can be found that the model simulates maximum flow velocities at within-creek water levels at creek station C0 and C2. The base-case model also simulates the maximum ebb flow velocities at a constant water level throughout the spring-neap cycle at stations C3-C5. Although, the model does not simulate the maximum ebb flow velocities at just over-bank elevations at stations C3-C5. When looking further into water level of the maximum flood flow velocities, it can be found that these are occurring at constant elevations at station C4 and C5. Therefore, the base-case only showed two of the four defined criteria.

The tidal flow-stage curves modeled with the roughness raster are shown in figure 6.2. The model simulates the maximum flood flow velocities at station C0 at within-creek water level. But for station C1, half of the maximum ebb flow velocities are at over-bank water levels. The maximum ebb flow velocities are simulated at constant just over-bank water levels at stations C3-C5. In contrast with the maximum ebb flow velocities, the maximum flood flow velocities occur at increasingly HWL. Therefore, the tidal stage-flow velocity curves showed to apply to three of the four defined criteria.

The tidal flow-stage curves of the second vegetation representation, the interflow layer, are shown in figure 6.8. The modeled maximum flow velocities at station C0 and C1 occur at both within-creek and over-bank water levels. The maximum ebb flow velocities at station C5 occur at increasingly HWL, while the maximum ebb flow velocities at stations C3 and C4 are occurring at constant water levels. The maximum ebb flow velocities at station C4 are occurring at just over-bank water level, but this is not the case for creek stations C3 and C5. The maximum flood flow velocities at stations C3-C5 are occurring at increasingly HWL. Therefore, the tidal stage-flow velocity curves showed to apply to one of the four criteria defined.

As stated in chapter 4, competences 2-5 will be assessed quantitatively using a NRMSE. In table 6.8 the NRMSE's for the four competences are given.

Competence	NRMSE Base Case	NRMSE Roughness Raster	NRMSE Interflow Layer
Duration asymmetry	0.142	0.234	0.359
along creek delay of the LWL	0.792	0.732	0.944
Maximum flow velocities	0.428	0.510	0.237
Tidal velocity asymmetry	0.606 & 0.452	0.467 & 0.229	0.588& 0.406

Table 6.8: Normalized root mean squared error results for the different hydrodynamic models set-up in this research tested on the first four competences

For the first competence, the duration asymmetry, all three models scored pretty well with NRMSE's below 0.4. But when comparing the NRMSE values, the base case model is the best performing model. Which has the implication that the addition of both vegetation representations did not improve the results of the model for this competence. When looking into the interpretation of the NRMSE values, the base-case and the roughness raster are simulating the duration asymmetry accurate. The interflow layer is simulating the duration asymmetry somewhat accurate.

The second competence, concerning the propagation velocity of the LWL along the creek, resulted in relatively high NRMSE's for all three models. The roughness raster did slightly improve the functioning of the model in comparison to the base-case model, but still resulted in a relatively high NRMSE. The addition of the interflow layer, did decrease the accuracy of the model on this competence in relation to the base-case. When looking into the interpretation of the different NRMSE, it can be seen that all models are poorly accurate on this competence.

The third and the fourth competence are assessing the flow velocities in the study area. The third competence, the maximum flow velocities, showed large differences between the different models. The roughness raster did not improve the model on this competence in relation to the base-case, while the interflow layer did improve the results of this model by 40% in relation to the base-case model. Interpreting the results, it can be found that the base-case model and the roughness raster model are somewhat accurate on simulating this competence, while the interflow layer is predicting this competence accurate.

The fourth competence focuses on the tidal velocity asymmetry, the NRMSE's for the forest stations are computed apart from the creek stations. The addition of the roughness raster did significantly improve the functioning of the model for the creek stations as well as for the forest stations in relation to the base-case. The addition of the interflow layer did improve the model results for the forest stations but only showed minor improvement for the ebb dominance in the creek stations. Interpreting the results, the models are simulating the tidal velocity asymmetry somewhat accurate. Except for the forest stations with the roughness raster model, these are predicted accurate.

Chapter 7

Discussion

7.1 Implications of the results

7.1.1 Use of subgrid-based modeling in intertidal areas

This study confirmed that by using a subgrid-based model, larger computational cells can be used without a significant effect on the hydrodynamic results. This is clearly shown in the sensitivity analysis performed on the water levels. In this analysis it became clear that the coarsening the grid to a 240 m by 240 m grid barely affected the water levels in comparison to a 10 m by 10 m grid. For the flow velocities larger differences are found, but for the flow velocities also the grid could be coarsened to a 40 m by 40 m grid without affecting the flow velocities too much. This observation is in contrast with modeling studies using traditional models, which found significant influence of the grid size on observed hydrodynamics (Deb et al., 2022; Rayson et al., 2015). This is especially applicable in intertidal areas with a highly variable bathymetry such as intertidal wetlands, as earlier research stated that the tidal dynamics in such area are largely topographic driven (Horstman et al., 2015). The benefit of using larger computational grid cells is that the computational time of the model will decrease. The computational cost of the hydrodynamic model using subgrid was only 40-80 minutes to simulate a whole spring-neap cycle (12 days). While, the computational cost of the full high resolution simulation was 140 hours for a whole spring-neap cycle.

The vegetation representations used in this research are mainly applied to the subgrid level. Meaning that the vegetation characteristics are defined at a high resolution. In the vegetation representations a distinction is made between three areas. Within these areas constant vegetation characteristics are applied. The application of the vegetation characteristics on the high-resolution subgrid, allows for making an accurate distinction between vegetated and unvegetated areas (e.g. between the creek and the forest). In comparison to traditional models, this has the advantage that the correct vegetation characteristics are applied in the different areas not hampered by the position of the computational cells. This effect is clearly shown in the increase in creek flow velocity compared to the base-case model for over-bank water elevations at creek station C3 and C4 when applying a roughness raster (figure 6.2). To further make use of the capability of the subgrid, the vegetation characteristics could also be varied over the forest platform, which could further increase the predictive capability of the model including a vegetation representation. Although, this is only possible if extensive vegetation measurements are performed in the study area.

7.1.2 Modeled tidal flow-stage curves

In the results of this research was found that the subgrid-based model accurately predicts the form of the tidal flow-stage curve. The form modeled by the hydrodynamic model without a vegetation representation is already pretty accurate (figure B.6). This is due to the fact that high-resolution bathymetry is taken into account and the tidal flow-stage curves are mainly bathymetry driven (Ashall et al., 2016; Horstman et al., 2015).

With the addition of the roughness raster a large increase in flow velocity in the creek can be found where the water levels are at over-bank elevations. This is due to the fact that the water experiences more bed friction on the forest platform which causes an increase in creek flow velocity in relation to the base-case. This observation is similar to observations in other studies (Ashall et al., 2016; Horstman et al., 2015), where is shown that due to vegetation on the forest platform more flow is routed via the creeks.

The addition of the interflow layer did not improve the predictive capability of the hydrodynamic model on tidal flow-stage curves, especially at creek stations C5-C6. This is caused by that the flow in the interflow layer does not take into account the effect of the narrowing creek in the back of the forest. As in the interflow layer diffusive flow is simulated, which does not take into account bathymetric properties (Nelen & Schuurmans, 2022). The interflow layer is defined relative to the lowest elevation in the computational cell, which causes that at the narrow creek with steep banks in the back of the forest relatively large amounts of water are routed via the interflow layer. Above the interflow layer the bathymetric effects are taken into account, but in the narrow creeks in the back of the study area, this has less effect due to the amount of flow routed via the interflow layer. This implies that the interflow layer cannot be used in simulating the observed hydrodynamics in the creek, therefore the interflow layer should only be used on the vegetated forest platform.

7.1.3 Water level results

Underestimating shoaling in the creek channel

At creek station C1 and C2 the measured HWL has increased with 10% with respect to the tides at creek station C0 (figure A.2 and A.3), caused by shoaling (Horstman et al., 2021). The measured increase in water levels at these creek stations is caused by the dominating effect of the decreasing channel width over the increase of the total transect width at stations C1 and C2 compared to C0. Additionally, the elevation of the surrounding intertidal flat increased close to the mangrove fringe, contributing to the shoaling (Horstman et al., 2021). This increase in water levels was not captured by the different models used in this research. For the base-case this can be explained by that the flow can be easily routed over the forest platform due to equal bed roughness on the forest platform and the creek channel. Therefore, the water level is less affected by the decreasing width of the channel in this section of the study area.

In comparison to the base-case, the bed roughness is increased on the forest platform with the roughness raster. But still the increase in water levels at C1 and C2 is not captured. This can be explained in the way the vegetation is represented. The roughness raster determines the bed roughness at a certain location, but the relative effect of this bed roughness decreases with water depth. This means that for higher water levels, the increased roughness on the forest platform only has small effect on the water level. Explaining the small effect of the roughness raster observed at high water levels.

The effect of the interflow layer does scale with the water depth, for the first 0.2 m of water depth. Above this water depth the water is modeled as open water flow. At high water levels, a part of the water column is flowing above the interflow layer where only a small increase in roughness is defined. This causes that the water can relatively easily flow over the forest platform, causing that the increase in water level at stations C1 and C2 is not captured.

The deviation in HWL comparing the simulated and measured water levels is approximately 0.065 m for the models including a vegetation representation. This deviation in HWL is comparable to other model studies in intertidal areas (Smolders et al., 2015; Stark et al., 2016). Both studies applied a roughness raster to take the effect of vegetation into account. This shows the need of using a vegetation representation that scales with the water depth, for example by applying the equations Baptist et al. (2007) explained in section 2.3.

Underestimating variation in LWL

In figure 3.3b can be found that the measured LWL shows significant variation comparing creek stations C0-C6. This is caused by the varying creek profile and varying vegetation properties on the forest platform. The varying vegetation causes that parts of the forest drain more quickly than other parts of the forest, as this is mainly vegetation driven.

When comparing this observation to the LWL's simulated by the different models (figure 7.1), barely any variation can be found in the simulated LWL's. This is caused by the uniform roughness/vegetation properties applied on the forest platform. Causing that the only variation in LWL in between the different stations is bathymetry driven. This can clearly be observed in figures 7.1a and 7.1b, where a large bathymetry driven variation can be found at station C6. This bathymetry driven variation is not observed in the model applying an interflow layer (figure 7.1c), for the reasons explained in the previous section.

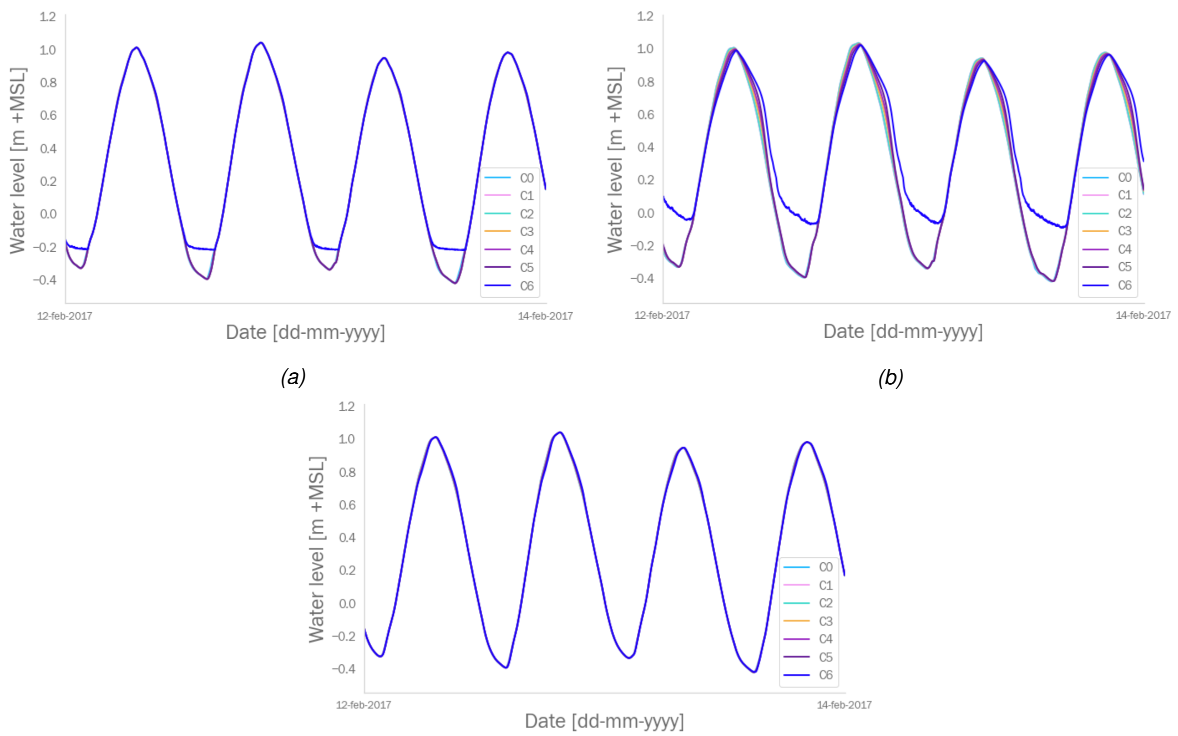

(a) (b) (c)

Figure 7.1: Modeled water levels at all creek stations from 12 February till 14 February, (a) water levels modeled by the base-case model (b) water levels when applying a roughness raster and (b) applying an interflow layer

Underestimation along creek delay and duration asymmetry

In the study area a large difference is found in the along creek propagation velocity of the LWL and HWL (figure 3.4b). Caused by the greater impact of the bed roughness for smaller water depths (Horstman et al., 2021). Next to this, an asymmetry was found between the duration of the rising and falling of the tide (figure 3.4a). Where the falling of the tide took 2-2.5 times longer than the rising tide. This duration asymmetry was created by the combined effect of the large-scale hypsometry and the vegetation properties, while local variations in creek geometry only generated minor variations (Horstman et al., 2021).

When looking into the simulated along creek delay of the LWL, it can be found that all three models are underestimating the along creek delay, especially at stations C1 and C2. For the base-case this can be explained by that the same roughness is applied to the forest platform as in the creeks. This causes that the water can easily flow over the forest platform, resulting in that the water in the forest can easily flow seawards over the forest platform. Causing that the forest easily drains, which increases the propagation velocity of the LWL. The same holds for the roughness raster, the bed roughness applied does not effect the route the water takes during drainage of the forest. Which causes that the forest quickly drains seawards over the forest platform, increasing the propagation velocity of the LWL along the creek.

The hydrodynamic model including an interflow layer does barely simulate a delay in LWL. The underestimation at creek stations C1 and C2 is caused by the same reason as in the other two models. But the interflow layer does also underestimate the propagation velocity of the LWL between stations C5 and C6. This is caused by the underestimation of the bathymetric effect in the back of the creek for the same reason as explained in section 7.1.2.

The duration asymmetry modeled by the different models shows the same trend as for the measured duration asymmetry. Although, the differences between the different creek for the same tides are smaller than measured. This is caused by that the measured duration asymmetry is mainly created by the vegetation properties, which are in all three models assumed equal over the whole forest platform. Creating less variation in duration asymmetry in between the different creek stations.

7.1.4 Flow Velocities

Underestimating creek ebb flow velocities

At the creek stations a higher creek ebb flow velocity is measured compared to flood flow velocities. This is caused by that the maximum ebb flow velocities occur at within-creek water levels, when the transport of water is confined to the creek.

While, maximum flood flow velocities occur at over-bank water levels when water also flows creek-parallel over the forest platform.

In the results can be found that the roughness raster as well as the interflow layer are underestimating the ebb flow velocities at station C3 compared to the measured ebb flow velocities (figures 6.5 and 6.11). For the roughness raster and the interflow layer, this can be explained by that during the maximum ebb flow velocity still a lot of water is routed via the forest platform, shown in figure 7.2. Caused by that the flow over the forest platform is not routed back to the creeks, but flows creek-parallel over the forest platform. Both vegetation representations were not able to reduce this flow enough at ebb tide to predict the correct maximum ebb flow velocities. This directly also influences the simulated tidal velocity asymmetries in the creek, which are underestimated by both vegetation representation. This observation implies that an uniform vegetation representation on the forest platform, is not able to simulate the observed flow routing in the area.

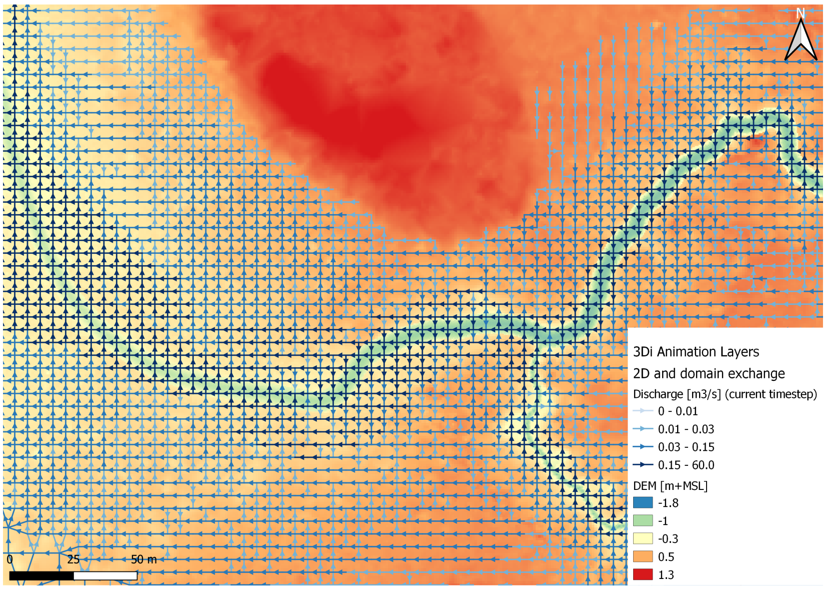

Figure 7.2: Flow routing using a calibrated roughness raster during ebb-tide on 14 February 2017

7.2 Uncertainties in the used methodology

7.2.1 Uncertainties in the hydrodynamic model in- and output

Digital Elevation Model

To construct a digital elevation map of the area, the creek profile is a combination of manual transect measurements and an available LiDAR map. For elevations lower than -0.4 m+MSL the LiDAR map was substituted with manually gathered transect data. In between the transects, where no manual bathymetry data was available, the bathymetry data was interpolated using the two nearest transects. In other studies performed in mangrove areas, ordinary kriging was used to reconstruct a complete bathymetry (Horstman et al., 2015). The ordinary kriging created a bathymetry with a vertical accuracy of the order 10^{-2}. In this research the transects were interpolated with a triangular interpolation method, which led to a smooth creek bed. This, could have had effect on the deformation of the tide and on the variation in LWL simulated.

Next to the missing bathymetry data in the creek, little information was available about the under-water bed elevations outside of the study area, which resulted in assumptions being made for the bed elevation in this part of the model domain. The bathymetry assumptions made outside of the study area could have negative impact on the simulated hydrodynamics within the study area, as it could have affected the deformation of the tide before it reached creek station C0. Which could possibly result in loss of accuracy in the results of the simulations.

Also at higher elevations the bathymetry showed some inaccuracies. Due to the vegetation cover in the forest, small creeks and pools were not captured as they were not visible. This is especially important near station C6, as a pool is observed in the measurements (figure 3.1c). This is not included in the bathymetry, which could have affected the water levels simulated at this station.

Although these uncertainties in the used bathymetry, comparing the used bathymetry to other modeling studies also a lot of improvements can be found. In other studies simulating hydrodynamics in an intertidal area the bathymetry was averaged over the grid cells, which are between 2 m by 2 m and 10 m by 10 m (Horstman et al., 2015; Horstman et al., 2013a). In our study the bathymetry was taken into account on a 1 m by 1 m resolution, which is apart from the uncertainties already a large improvement in comparison to traditional models.

Locations of the retrieved model results

In the used modeling software, 3Di, simulation results are only available at the center points of the grid cells for water levels, and at the cell edges for flow velocities. Therefore, there is a discrepancy between the locations of the model results and the measurement locations. By decreasing the computational grid in the study area, the effect is minimized to a maximum distance of 2.5 meter.

Natural variations

Natural variations in weather could have had effects on the measurements performed in the area, for example higher flow velocities or water levels due to wind set-up. These natural variations are not taken into account in the numerical simulation. When afterwards comparing the results of the model with the measurements this could lead to discrepancies.

7.2.2 Calibration and validation

Calibration

The calibration procedure for the vegetation representations used in this research is based on improving the predicted HWL and LWL in the study area. For the calibration of the roughness raster, the water levels changed with changing values of the roughness raster, although only minor improvements were achieved. Therefore, high roughness values (outside of the range measured in the area) had to be used on the forest platform. This did slightly improve the modeled HWL and LWL in the area, but did also have effects on the measured flow velocities. By applying high roughness values on the forest platform, the model underestimated the flow velocities in the forest resulting in poor model performance on predicted flow velocities. For the interflow layer, the water levels did not significantly change when changing the parameters of the interflow layer.

Looking back on the choices made for the calibration, it can be concluded that possibly better results could have been achieved when focusing on another calibration parameter. This is mainly because the chosen vegetation representations showed to have small effect on the HWL in the study area. This was the case for the roughness raster but especially for the interflow layer, which did not have any significant effect on the modeled HWL. Therefore, it is suggested to calibrate the vegetation representations on the flow velocities in the three defined areas. This would increase the capability of the models in predicting the flow velocities in the creek and the forest, which are also affecting the asymmetries observed in the area.

The downside of calibrating using the flow velocities, is that measured flow velocities are more prone to variations due to external factors, small-scale variations in the vegetation or bathymetry. Which can not be captured within a hydrodynamic model.

Validation

The flow velocities used in the validation of the hydrodynamic models are cross-sectional averaged quantities. Which means that flow velocities cannot easily be compared at an exact location, for example the thalweg of the creek. Due to the subgrid modeling technique the flow velocities can be reconstructed to each subgrid cell, although due to time constraints this was outside of the scope of the research.

But if reconstruction was applied to the flow velocities, the flow velocities could be compared more accurately. This could especially improve the modeled flow velocities in the creek, as the flow velocity is measured in the deepest part of the creek. In the deepest part of the creek the flow velocity is the biggest, this explains that reconstructing flow velocities to retrieve the flow velocity at this point could improve the predictive capability of the model as flow velocities are less underestimated. Therefore, it would be good to reconstruct the flow velocities when comparing modeled with measured flow velocities. This is especially important if flow velocities would be used during the calibration process.

Chapter 8

Conclusions and recommendations

8.1 Conclusions

The aim of this research was to investigate the impact of two vegetation representations in a subgrid-based hydrodynamic model of a mangrove forest in the Whitianga estuary. Following from this, the main research question is:

What is the effect of taking vegetation into account in a subgrid-based hydrodynamic model of the Whitianga study area?

In this research a subgrid-based hydrodynamic model was used, which efficiently takes high-resolution spatial data into account. The difference with a conventional model is that the spatial data is not averaged over the larger computational grid cells but is incorporated in the model via the higher-resolution subgrid, so spatial resolution is not lost. The use of this subgrid-based model has shown that larger computational grid cells can be used without massively affecting the modeled hydrodynamics in the area. Outside the study area, grid cells of 40 m by 40 m could be used and within the study area grid cells of 5 m by 5 m to be able to accurately compare model results with measured hydrodynamics. This reduced the computational time of the model from 140 hours to 1.5 hours for modeling a whole spring-neap cycle. Using this computational grid size without the subgrid would destabilize within-creek flow velocities and loose the cross-sectional properties of narrow creeks.

Two different vegetation representations have been tested in the subgrid-based hydrodynamic model. The first vegetation representation is a spatially varying roughness, implemented via a roughness raster. A distinction in roughness is made between the deeper channels, the inner creek and the vegetated forest platform. The roughness raster was calibrated on HWL and LWL which resulted in a roughness raster with a Chézy value of: 60 [$m^{1/2}s^{-1}$] in the channel, 10 [$m^{1/2}s^{-1}$] in the creek between station C2-C6, and 5 [$m^{1/2}s^{-1}$] on the forest platform.

The second vegetation representation, is simulating the effect of vegetation as flow through a porous medium. This is implemented in the model via an interflow layer. In defining the interflow layer the same distinction between the three areas has been used as in the roughness raster. The parameters of the interflow layer have been set using vegetation and hydrodynamic measurements in the area. After calibrating the interflow layer on HWL and LWL, the depth of the interflow layer was set to 20 cm. A porosity of 0.9 was used in the forest, 0.98 in the creek between stations C2-C6 and 1 in the deep channel and creek between stations C0-C1. A hydraulic conductivity of 4167 m/s was used in the deep channel and the whole creek system, and a hydraulic conductivity of 333 m/s was used on the forest platform. To take into account the canopy-scale turbulence a roughness raster was applied with a Chézy value of: 60 [$m^{1/2}s^{-1}$] in the channel, 40 [$m^{1/2}s^{-1}$] in the creek between stations C2-C6, and 20 [$m^{1/2}s^{-1}$] on the forest platform.

The vegetation representations have been validated on five competences. The roughness raster did improve the predictive capability of the model on the tidal flow-stage curves, the along creek delay and the tidal flow velocity asymmetry in comparison to the model without a vegetation representation. But still largely underestimated the along creek delay and the ebb tidal velocity, caused by the creek-parallel flow over the forest platform during ebb tide. Which is directly routed via the forest platform seawards, in stead of routed through the creek. The roughness raster did decrease the predictive capability of the model on the maximum flow velocities, due to the high bed roughness applied in the forest.

The interflow layer, did decrease the predictive capability of the model on the tidal flow-stage curves, the duration asymmetry and the along creek delay. This is mainly caused due to that the flow in the creek is also simulated partly in the interflow layer. This decreased the effect of the bathymetry on the flow, which had negative impact on the predictive capability of the model on these competences as these characteristics are mainly bathymetry-driven. For the interflow layer the same behaviour is observed as for the roughness raster, where a lot of flow is still routed via the forest platform during ebb flow. This caused that the maximum ebb flow velocity was underestimated, which resulted in a poor predictive capability of the creek flow velocity asymmetry. The interflow layer did improve the predictive capability of the model on the flow velocities observed on the forest platform in relation to the base-case.

To answer the main research question, the two different vegetation representations assessed in this research both have a different influence on the model results. The roughness raster did improve the predictive capability of the model on three out of five competences, while the interflow layer only improved the model on two out of five competences. The application of a spatially varying roughness did increase the flow velocity in the creek and increased the ebb-dominance observed in the creek. It decreased the flow velocity in the forest, but could not simulate the measured routing of the water during ebb-flow. The interflow layer did also decrease the flow velocity in the forest and increased the flow velocity in the creek. Although, it did barely improve the model on the observed creek ebb-flow asymmetry. Caused by that the same flow-routing is observed compared to the roughness raster. Moreover, by simulating part of the creek flow in the interflow layer did decrease the predictive capability of the model on the duration asymmetry and the along creek delay.

8.2 Recommendations for future research

The research clearly showed the applicability of the subgrid modeling technique for modeling mangrove eco-systems. Therefore, it can be recommended to use this research as a stepping stone for further research into modeling mangrove eco-systems with the subgrid modeling method.

The research has shown that the roughness raster has a positive effect on most competences. The subgrid modeling method has the capability to further specify the vegetation characteristics on a high-resolution (e.g. a varying roughness on the forest platform). It is recommended to further look into the influence of varying the vegetation characteristics over the forest platform using the density measurements from the area, as this could improve the predictive capability of the model. On the other hand, the roughness raster showed to have less effect on high water levels, due to the decreasing influence of the roughness raster with increasing water depth. Therefore, for future research it is recommended to look further into applying a vegetation representation that scales with water depth.

The interflow layer has shown to decrease the predictive capability of the model for most competences. This is mainly caused by that part of the creek flow is also simulated with the interflow layer. Therefore, it it recommended to further explore the applicability of the interflow layer in simulating flow through vegetation. But only applying the interflow layer to the areas where dense vegetation is present. As it has shown to accurately simulate flow velocities on the forest platform

In future research it is also recommended to not solely focus the calibration process on HWL and LWL as both vegetation representations showed only minor improvements on this characteristic. Therefore, in future research it is recommended to also include flow velocities on the forest platform and in the creek in the calibration process. Using a water level and flow velocity calibration procedure could further improve the functioning of both vegetation representations.

References

AgriMetSoft. (2019). RMSE (Root Mean Square Error). https://agrimetsoft.com/calculators/Root%20Mean%20Square%20Error

AgriMetSoft. (2020). NRMSE (Normalized Root Mean Square Error). https://agrimetsoft.com/calculators/Normalized%20Root%20Mean%20Square%20Error#:~:text=The%20Normalized%20Root%20Mean%20Square,typically%20resolved%20by%20the%20model.

Ashall, L. M., Mulligan, R. P., Van Proosdij, D. & Poirier, E. (2016). Application and validation of a three-dimensional hydrodynamic model of a macrotidal salt marsh. *Coastal Engineering*, *114*, 35–46. https://doi.org/10.1016/j.coastaleng.2016.04.005

Baptist, M. J., Babovic, V., Uthurburu, J. R., Keijzer, M., Uittenbogaard, R. E., Mynett, A. & Verwey, A. (2007). On inducing equations for vegetation resistance. *Journal of Hydraulic Research*, *45*(4), 435–450. https://doi.org/10.1080/00221686.2007.9521778

Best, S., Van der Wegen, M., Dijkstra, J., Willemsen, P. W., Borsje, B. W. & Roelvink, D. J. (2018). Do salt marshes survive sea level rise? Modelling wave action, morphodynamics and vegetation dynamics. *Environmental Modelling and Software*, *109*, 152–166. https://doi.org/10.1016/j.envsoft.2018.08.004

Breda, A., Saco, P. M., Sandi, S. G., Saintilan, N., Riccardi, G. & Rodríguez, J. F. (2021). Accretion, retreat and transgression of coastal wetlands experiencing sea-level rise. *Hydrology and Earth System Sciences*, *25*(2), 769–786. https://doi.org/10.5194/hess-25-769-2021

Britter, R. E. & Hanna, S. R. (2003). Flow and dispersion in urban areas. *Annual Review of Fluid Mechanics*, *35*, 469–496. https://doi.org/10.1146/annurev.fluid.35.101101.161147

Casulli, V. (2009). A high-resolution wetting and drying algorithm for free-surface hydrodynamics. *International Journal for Numerical Methods in Fluids*, *60*(4), 391–408. https://doi.org/10.1002/fld.1896

Deb, M., Abdolali, A., Kirby, J. T. & Shi, F. (2022). Hydrodynamic modeling of a complex salt marsh system: Importance of channel shoreline and bathymetric resolution. *Coastal Engineering*, *173*. https://doi.org/10.1016/j.coastaleng.2022.104094

Deltares. (2021). *Delft3D 3D/2D modelling suite for integral water solutions Hydro-Morphodynamics* (tech. rep.).

FAO. (2007). *State of the world's forests, 2007.* Food; Agriculture Organization of the United Nations.

Friedrichs, C. T. (2010). Barotropic tides in channelized estuaries. *Contemporary issues in estuarine physics* (pp. 27–61). Cambridge University Press. https://doi.org/10.1017/CBO9780511676567.004

Furukawa & Wolanski. (1996). Sedimentation In Mangrove Forests.

Gijsman, R., Horstman, E. M., van der Wal, D., Friess, D. A., Swales, A. & Wijnberg, K. M. (2021). Nature-Based Engineering: A Review on Reducing Coastal Flood Risk With Mangroves. https://doi.org/10.3389/fmars.2021.702412

Giri, C., Ochieng, E., Tieszen, L. L., Zhu, Z., Singh, A., Loveland, T., Masek, J. & Duke, N. (2011). Status and distribution of mangrove forests of the world using earth observation satellite data. *Global Ecology and Biogeography*, *20*(1), 154–159. https://doi.org/10.1111/j.1466-8238.2010.00584.x

Gourgue, O., van Belzen, J., Schwarz, C., Bouma, T. J., van de Koppel, J. & Temmerman, S. (2021). A Convolution Method to Assess Subgrid-Scale Interactions Between Flow and Patchy Vegetation in Biogeomorphic Models. *Journal of Advances in Modeling Earth Systems*, *13*(2). https://doi.org/10.1029/2020MS002116

Haughey, R. R. (2017). *Modelling The Hydrodynamics Within The Mangrove Tidal Flats in The Firth Of Thames* (Doctoral dissertation). University of Waikato. Waikato.

Horstman, E. M., Dohmen-Janssen, C. M., Bouma, T. J. & Hulscher, S. J. (2015). Tidal-scale flow routing and sedimentation in mangrove forests: Combining field data and numerical modelling. *Geomorphology*, *228*, 244–262. https://doi.org/10.1016/j.geomorph.2014.08.011

Horstman, E. M., Dohmen-Janssen, C. M. & Hulscher, S. J. (2013a). *MODELING TIDAL DYNAMICS IN A MANGROVE CREEK CATCHMENT IN DELFT3D* (tech. rep.). https://ris.utwente.nl/ws/portalfiles/portal/223257889/Horstman2013modeling.pdf

Horstman, E. M., Dohmen-Janssen, C. M., Narra, P. M., van den Berg, N. J., Siemerink, M. & Hulscher, S. J. (2014). Wave attenuation in mangroves: A quantitative approach to field observations. *Coastal Engineering*, *94*, 47–62. https://doi.org/10.1016/j.coastaleng.2014.08.005

Horstman, E. M., Bryan, K. R. & Mullarney, J. C. (2021). Drag variations, tidal asymmetry and tidal range changes in a mangrove creek system. *Earth Surface*

Processes and Landforms, *46*(9), 1828–1846. https://doi.org/10.1002/esp.5124

Horstman, E. M., Dohmen-Janssen, C. M. & Hulscher, S. J. (2013b). Flow routing in mangrove forests: A field study in Trang province, Thailand. *Continental Shelf Research*, *71*, 52–67. https://doi.org/10.1016/j.csr.2013.10.002

Horstman, E. M., Lundquist, C. J., Bryan, K. R., Bulmer, R. H., Mullarney, J. C. & Stokes, D. J. (2018). The Dynamics of Expanding Mangroves in New Zealand. *Coastal Research Library*, *25*, 23–51. http://www.springer.com/series/8795

Hu, K., Chen, Q., Wang, H., Hartig, E. K. & Orton, P. M. (2018). Numerical modeling of salt marsh morphological change induced by Hurricane Sandy. *Coastal Engineering*, *132*, 63–81. https://doi.org/10.1016/j.coastaleng.2017.11.001

Jones, H. (2008). *Coastal Sedimentation: What We Know and the Information Gaps* (tech. rep.). www.ew.govt.nz

Kirezci, E., Young, I. R., Ranasinghe, R., Muis, S., Nicholls, R. J., Lincke, D. & Hinkel, J. (2020). Projections of global-scale extreme sea levels and resulting episodic coastal flooding over the 21st Century. *Scientific Reports*, *10*(1). https://doi.org/10.1038/s41598-020-67736-6

Krauss, K. W., Allen, J. A. & Cahoon, D. R. (2003). Differential rates of vertical accretion and elevation change among aerial root types in Micronesian mangrove forests. *Estuarine, Coastal and Shelf Science*, *56*(2), 251–259. https://doi.org/10.1016/S0272-7714(02)00184-1

Kulp, S. A. & Strauss, B. H. (2019). New elevation data triple estimates of global vulnerability to sea-level rise and coastal flooding. *Nature Communications*, *10*(1). https://doi.org/10.1038/s41467-019-12808-z

Lowe, R. J., Falter, J. L., Koseff, J. R., Monismith, S. G. & Atkinson, M. J. (2007). Spectral wave flow attenuation within submerged canopies: Implications for wave energy dissipation. *Journal of Geophysical Research: Oceans*, *112*(5). https://doi.org/10.1029/2006JC003605

Mazda', Y., Kanazawa2, N. & Wolanski, E. (1995). *Tidal asymmetry in mangrove creeks* (tech. rep.).

Mazda, Y., Kobashi, D. & Okada, S. (2005). Tidal-scale hydrodynamics within mangrove swamps. *Wetlands Ecology and Management*, *13*(6), 647–655. https://doi.org/10.1007/s11273-005-0613-4

Mazda, Y., Magi, M., Ikeda, Y., Kurokawa, T. & Asano, T. (2006). Wave reduction in a mangrove forest dominated by Sonneratia sp. *Wetlands Ecology and Management*, *14*(4), 365–378. https://doi.org/10.1007/s11273-005-5388-0

Mazda, Y., Wolanski, E., King, B., Sase, A., Ohtsuka, D. & Magi, M. (1997). *Drag force due to vegetation in mangrove swamps* (tech. rep.). Kluwer Academic Publishers.

Menéndez, P., Losada, I. J., Beck, M. W., Torres-Ortega, S., Espejo, A., Narayan, S., Díaz-Simal, P. & Lange, G. M. (2018). Valuing the protection services of mangroves at national scale: The Philippines. *Ecosystem Services*, *34*, 24–36. https://doi.org/10.1016/j.ecoser.2018.09.005

Mullarney, J. C. & Henderson, S. M. (2018). *Chapter 1 Flows Within Marine Vegetation Canopies* (tech. rep.). www.worldscientific.com

Mullarney, J. C., Henderson, S. M., Reyns, J. A., Norris, B. K. & Bryan, K. R. (2017). Spatially varying drag within a wave-exposed mangrove forest and on the adjacent tidal flat. *Continental Shelf Research*, *147*, 102–113. https://doi.org/10.1016/j.csr.2017.06.019

Nair, K. P. (2010). The Coconut Palm (Cocos nucifera L.) *The agronomy and economy of important tree crops of the developing world* (pp. 67–109). Elsevier. https://doi.org/10.1016/b978-0-12-384677-8.00003-5

Nelen & Schuurmans. (2022). 2D interflow. https://docs.3di.live/g_interflow.html

Nepf, H. M. (1999). Drag, turbulence, and diffusion in flow through emergent vegetation. *Water Resources Research*, *35*(2), 479–489. https://doi.org/10.1029/1998WR900069

Nepf, H. M. (2012). Hydrodynamics of vegetated channels. *Journal of Hydraulic Research*, *50*(3), 262–279. https://doi.org/10.1080/00221686.2012.696559

Neumann, B., Vafeidis, A. T., Zimmermann, J. & Nicholls, R. J. (2015). Future coastal population growth and exposure to sea-level rise and coastal flooding - A global assessment. *PLoS ONE*, *10*(3). https://doi.org/10.1371/journal.pone.0118571

Norris, B. K., Mullarney, J. C., Bryan, K. R. & Henderson, S. M. (2017). The effect of pneumatophore density on turbulence: A field study in a Sonneratia-dominated mangrove forest, Vietnam. *Continental Shelf Research*, *147*, 114–127. https://doi.org/10.1016/j.csr.2017.06.002

Ostling, J. L., Butler, D. R. & Dixon, R. W. (2009). The biogeomorphology of mangroves and their role in natural hazards mitigation. *Geography Compass*, *3*(5), 1607–1624. https://doi.org/10.1111/j.1749-8198.2009.00265.x

Rayson, M. D., Gross, E. S. & Fringer, O. B. (2015). Modeling the tidal and sub-tidal hydrodynamics in a shallow, micro-tidal estuary. *Ocean Modelling*, *89*, 29–44. https://doi.org/10.1016/j.ocemod.2015.02.002

Saintilan, N., Khan, N. S., Ashe, E., Kelleway, J. J., Rogers, K., Woodroffe, C. D. & Horton, B. P. (2020). Thresholds of mangrove survival under rapid sea level rise. *Science*. https://www.science.org

Smolders, S., Meire, P., Plancke, Y., Ides, S., Meire, P. & Temmerman, S. (2015). Role of intertidal wetlands for tidal and storm tide attenuation along a confined estuary: a model study-discussion paper. *Nat. Hazards Earth Syst. Sci. Discuss*, *3*, 3181–3224. https://doi.org/10.5194/nhessd-3-3181-2015

Stark, J., Van Oyen, T., Meire, P. & Temmerman, S. (2015). Observations of tidal and storm surge attenuation in a large tidal marsh. *Limnology and Oceanography*, *60*(4), 1371–1381. https://doi.org/10.1002/lno.10104

Stark, J., Plancke, Y., Ides, S., Meire, P. & Temmerman, S. (2016). Coastal flood protection by a combined nature-based and engineering approach: Modeling the effects of marsh geometry and surrounding dikes. *Estuarine, Coastal and Shelf Science*, *175*, 34–45. https://doi.org/10.1016/j.ecss.2016.03.027

Taherkhani, M., Vitousek, S., Barnard, P. L., Frazer, N., Anderson, T. R. & Fletcher, C. H. (2020). Sea-level rise exponentially increases coastal flood frequency. *Scientific Reports*, *10*(1). https://doi.org/10.1038/s41598-020-62188-4

Töpke, K. (2022). Mangroves. http://www.coastalwiki.org/wiki/Mangroves

Volp, N. D., Van Prooijen, B. C. & Stelling, G. S. (2013). A finite volume approach for shallow water flow accounting for high-resolution bathymetry and roughness data. *Water Resources Research*, *49*(7), 4126–4135. https://doi.org/10.1002/wrcr.20324

Woodruff, J. D., Irish, J. L. & Camargo, S. J. (2013). Coastal flooding by tropical cyclones and sea-level rise. https://doi.org/10.1038/nature12855

Appendix A

Water levels vegetation representations

A.1 Water level roughness raster

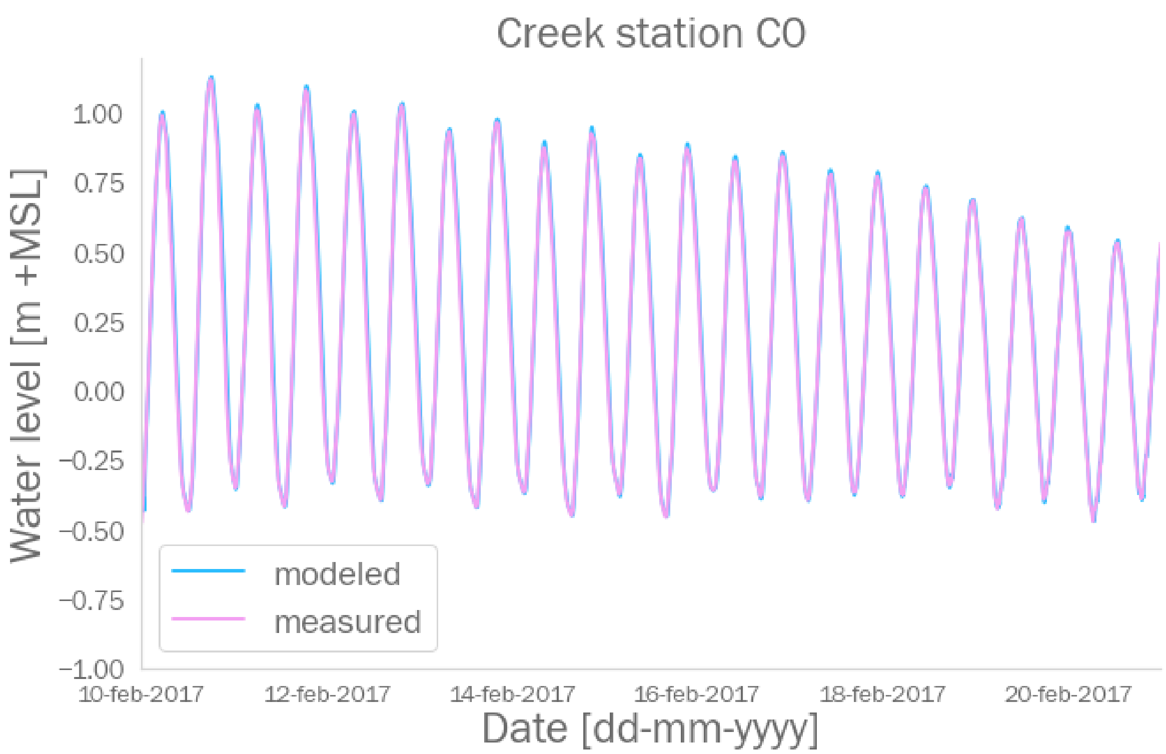

Figure A.1: Comparison between modeled and measured water levels at creek station C0

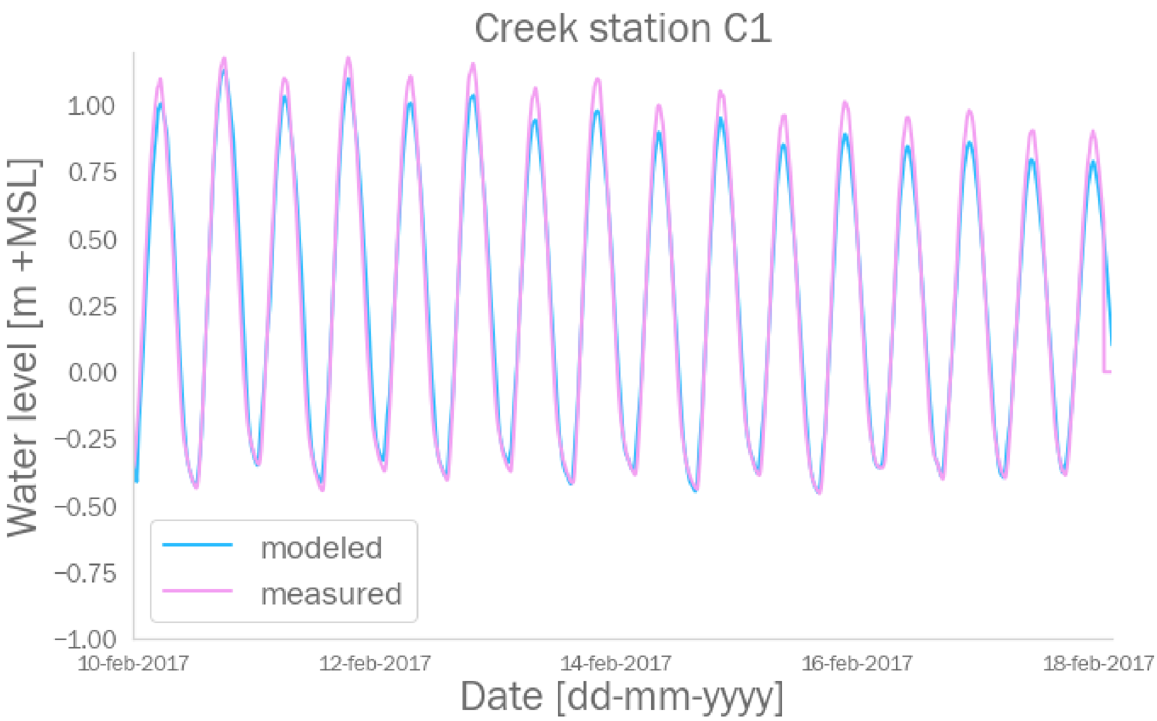

Figure A.2: Comparison between modeled and measured water levels at creek station C1

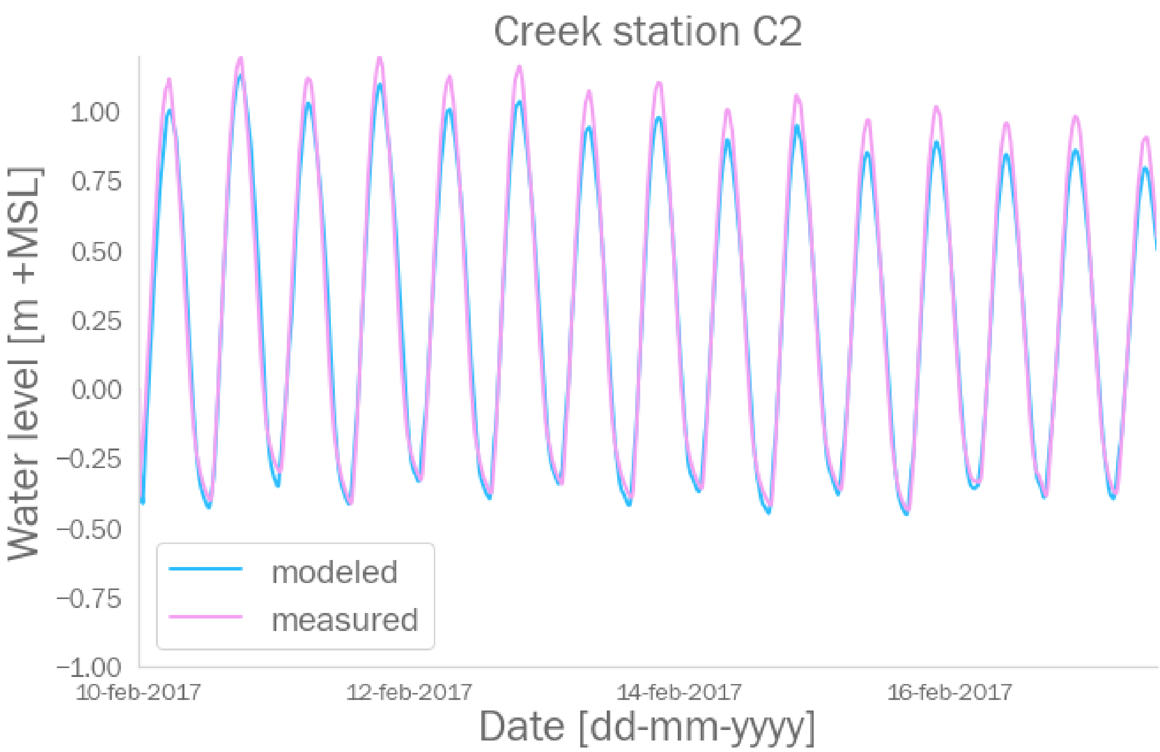

Figure A.3: Comparison between modeled and measured water levels at creek station C2

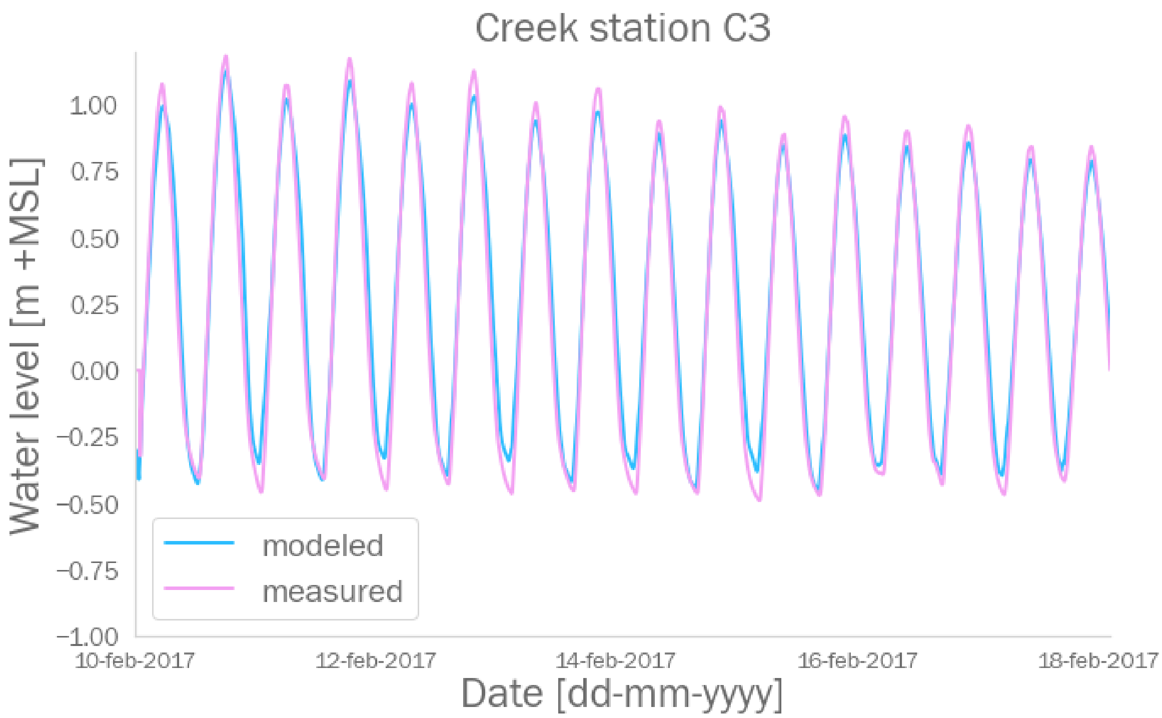

Figure A.4: Comparison between modeled and measured water levels at creek station C3

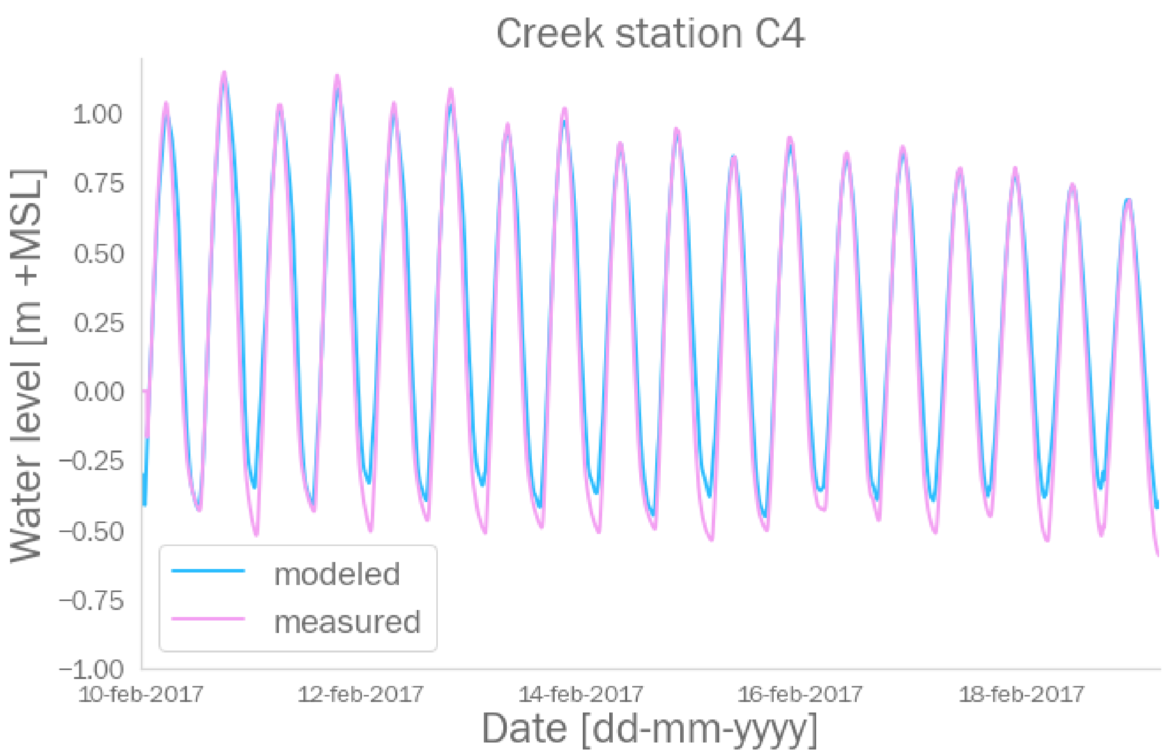

Figure A.5: Comparison between modeled and measured water levels at creek station C4

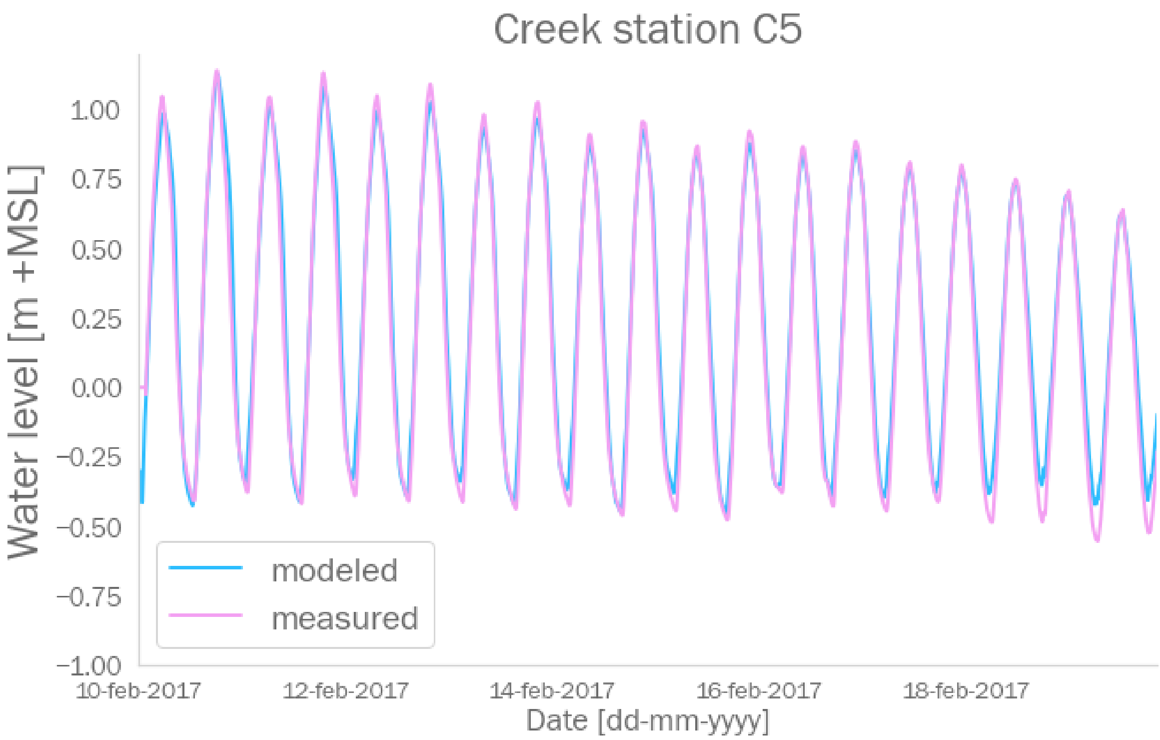

Figure A.6: Comparison between modeled and measured water levels at creek station C5

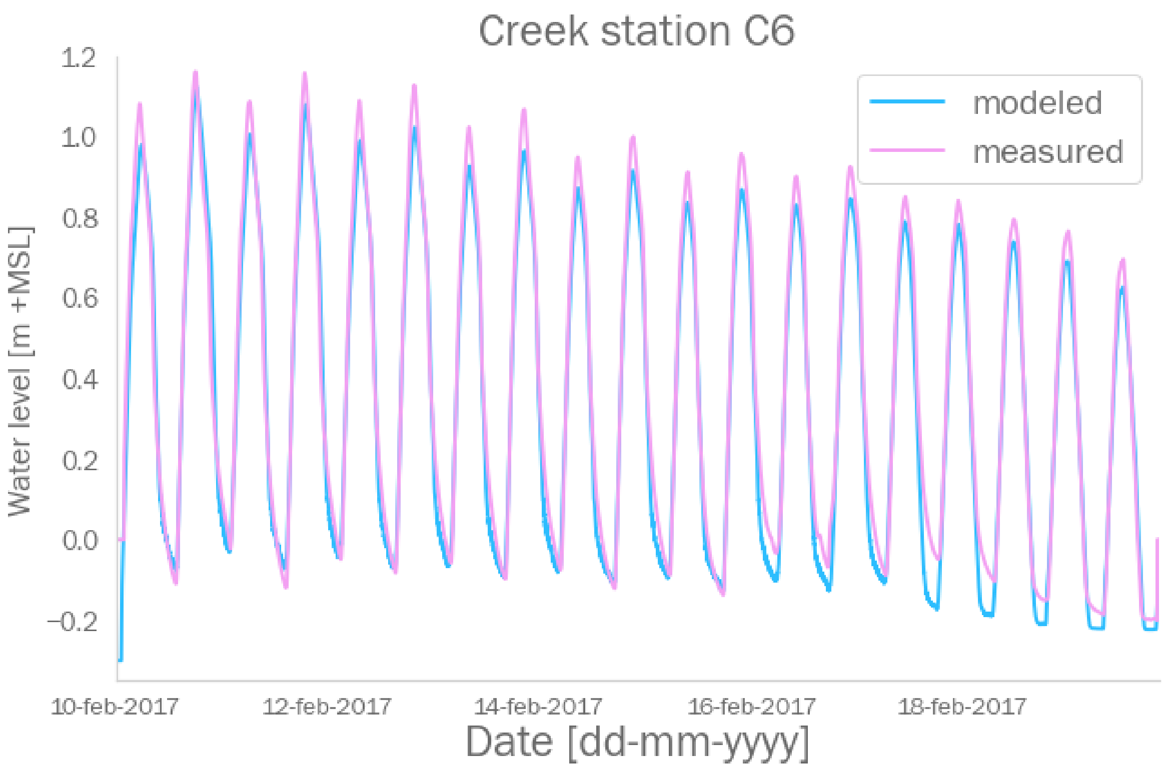

Figure A.7: Comparison between modeled and measured water levels at creek station C6

A.2 Water levels interflow layer

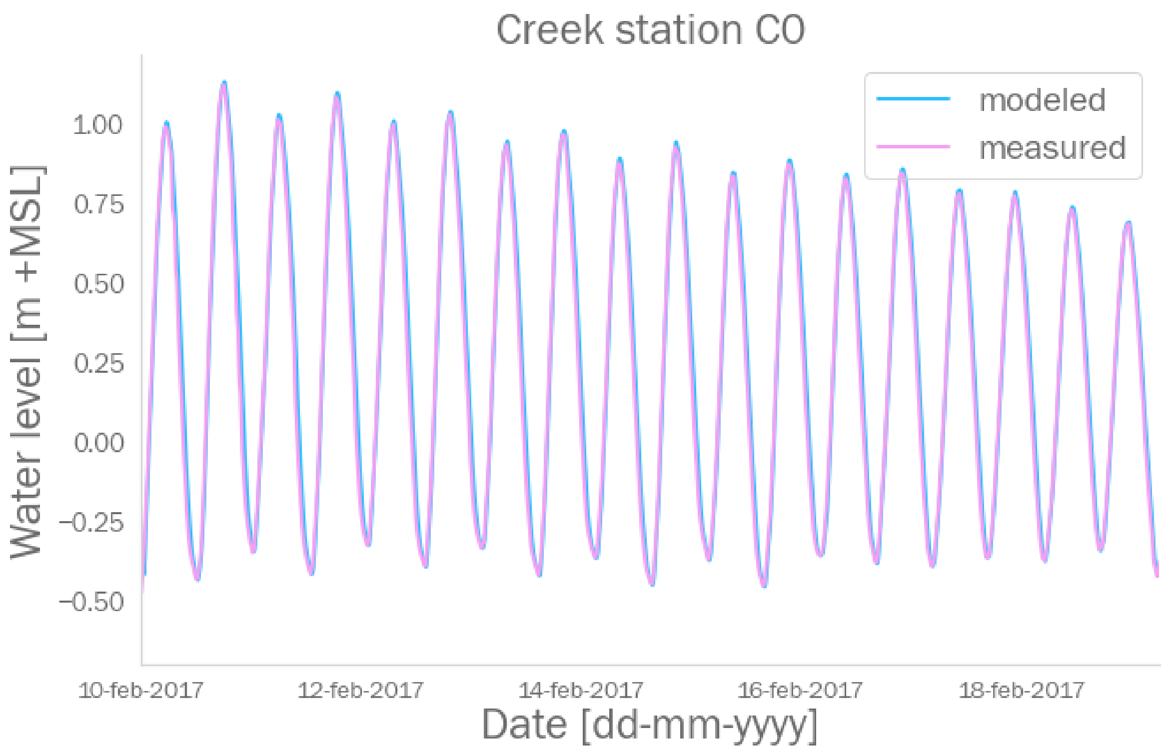

Figure A.8: Comparison between modeled and measured water levels at creek station C0

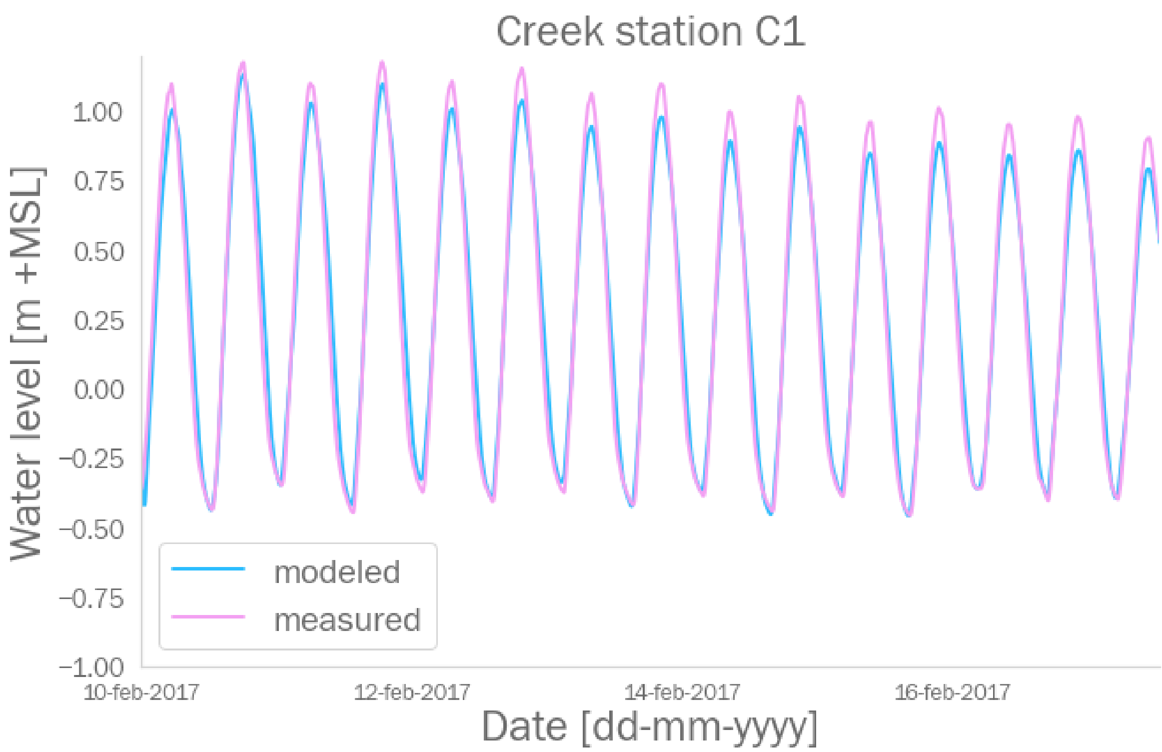

Figure A.9: Comparison between modeled and measured water levels at creek station C1

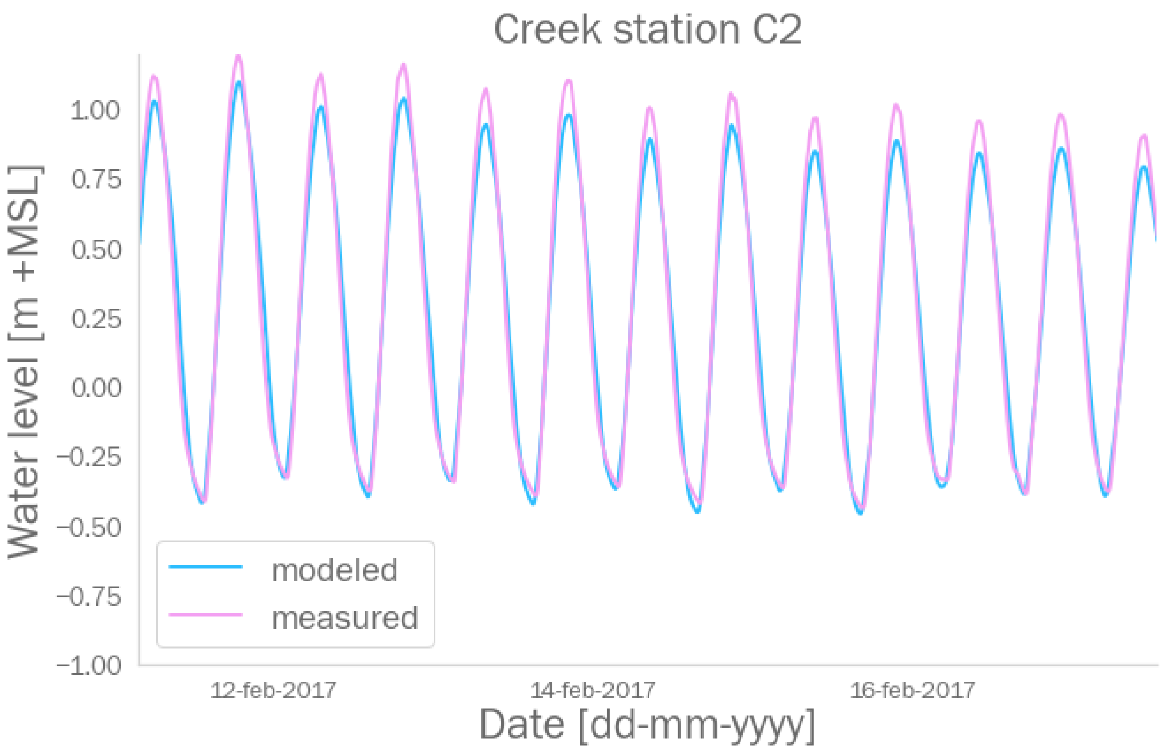

Figure A.10: Comparison between modeled and measured water levels at creek station C2

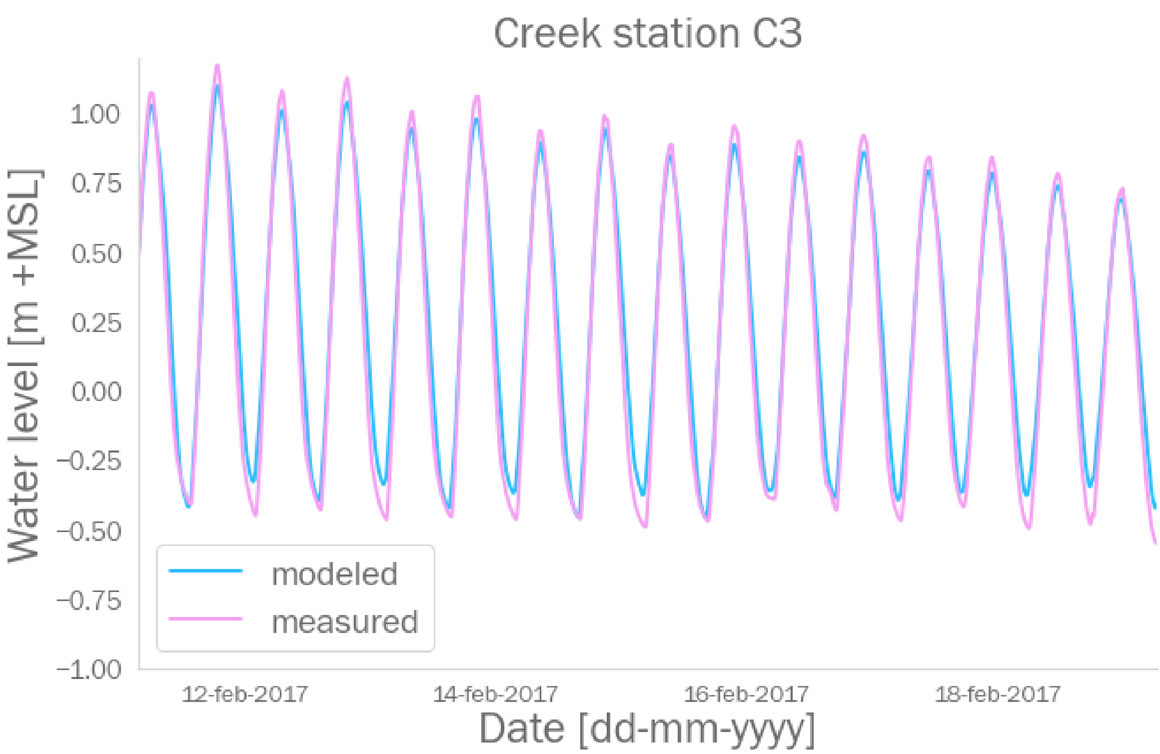

Figure A.11: Comparison between modeled and measured water levels at creek station C3

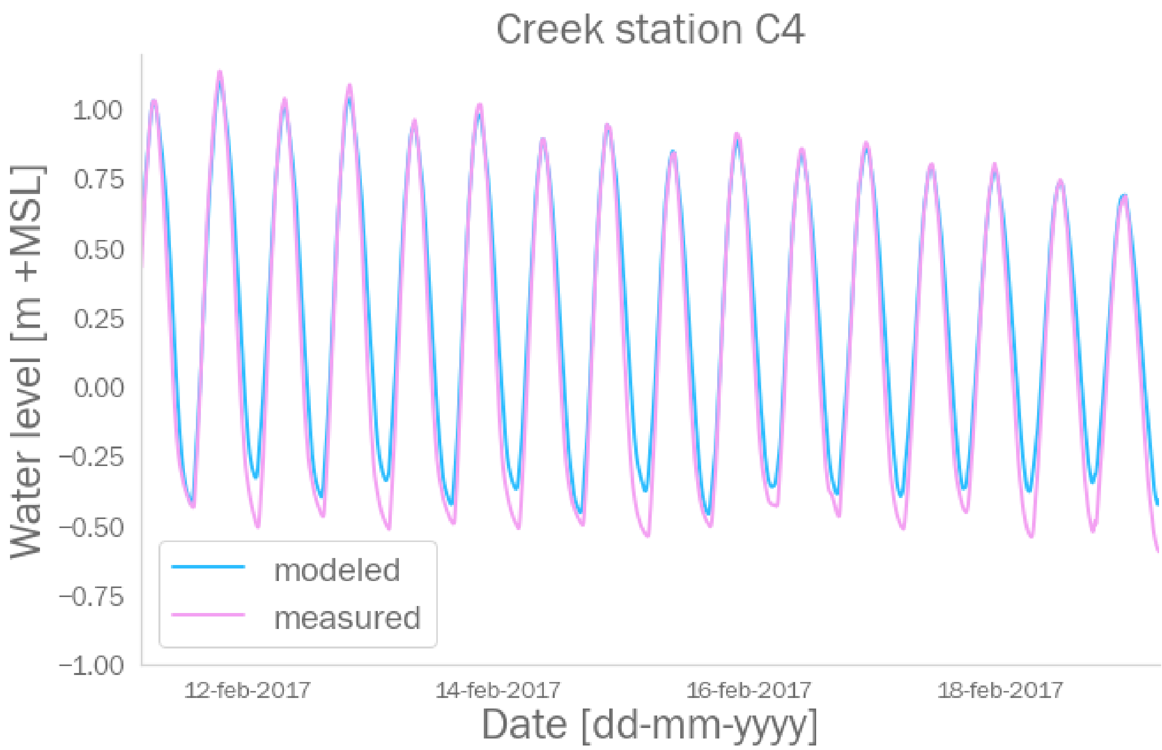

Figure A.12: Comparison between modeled and measured water levels at creek station C4

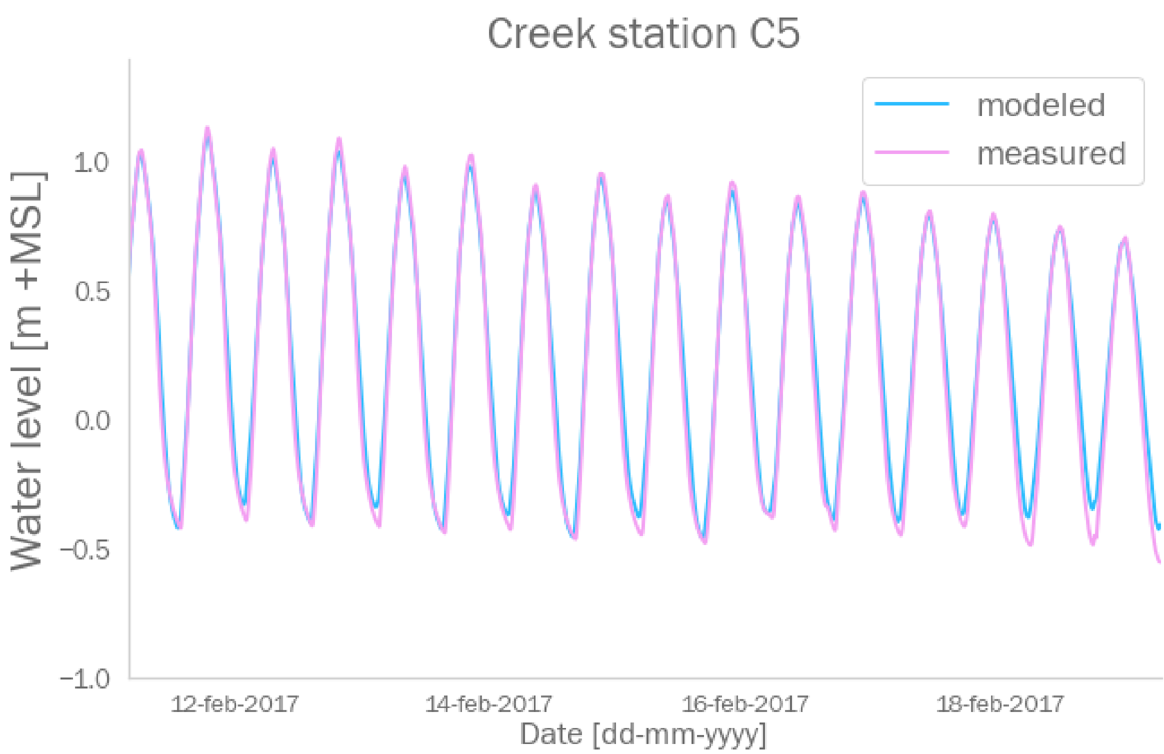

Figure A.13: Comparison between modeled and measured water levels at creek station C5

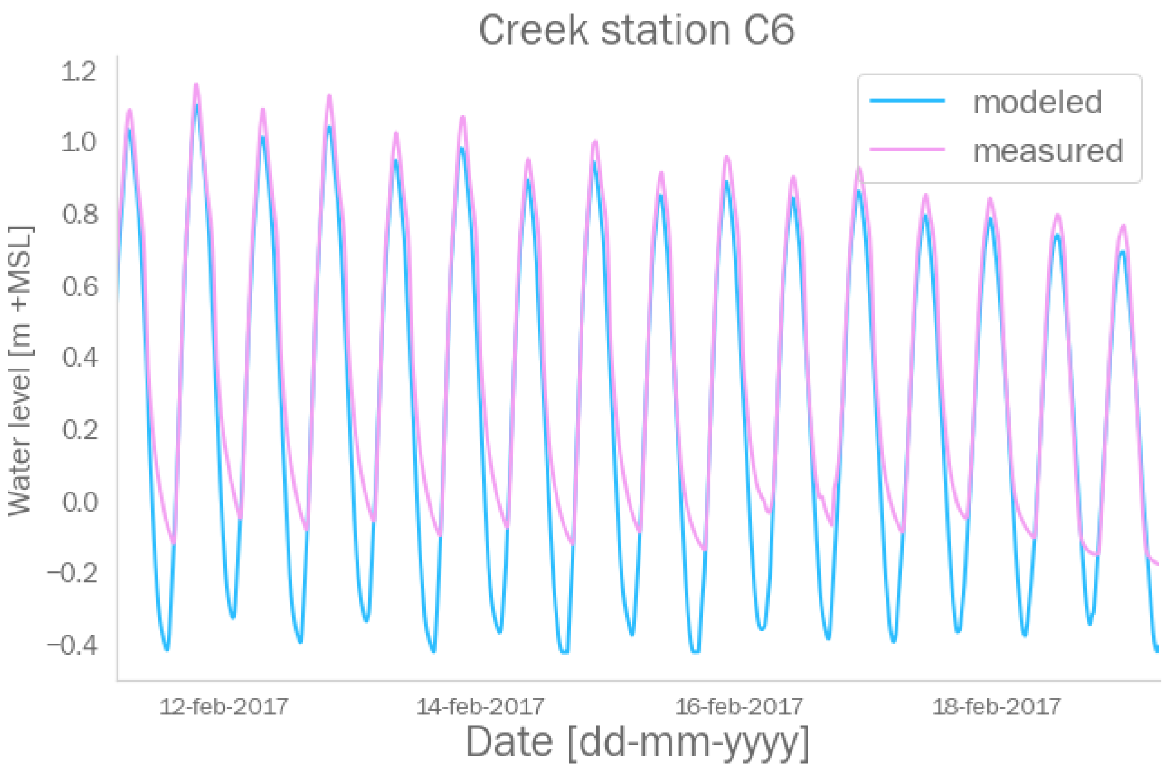

Figure A.14: Comparison between modeled and measured water levels at creek station C6

Appendix B

Results base-case simulation

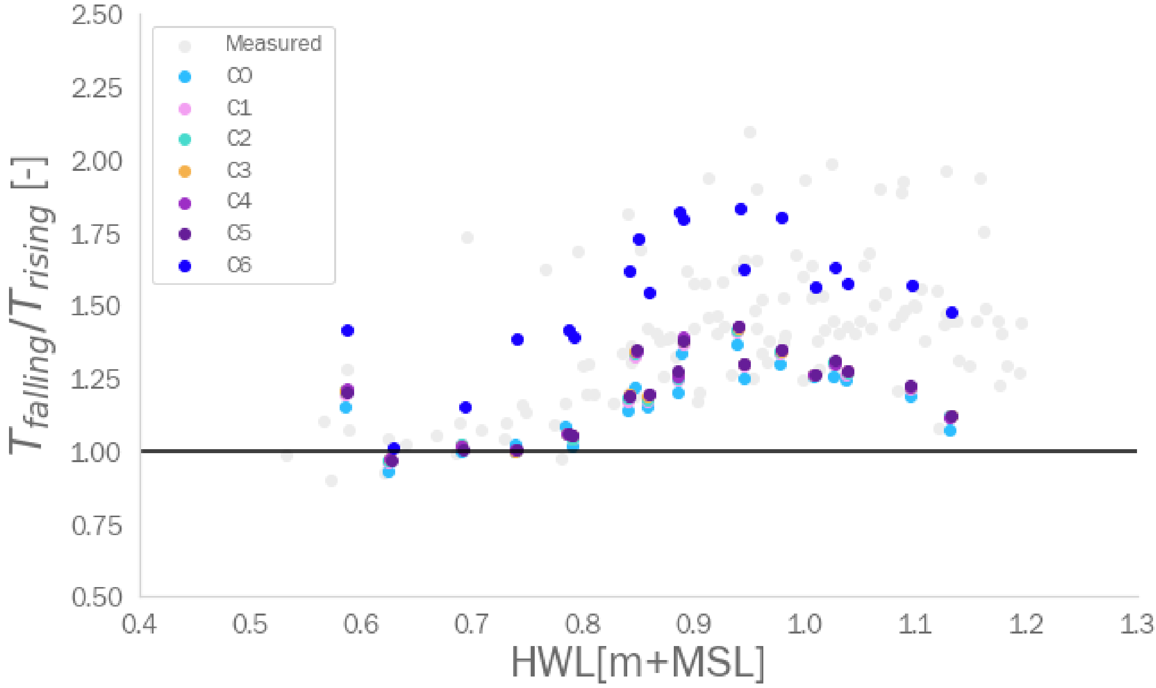

Figure B.1: Duration asymmetry at the creek stations modeled with the base-case model

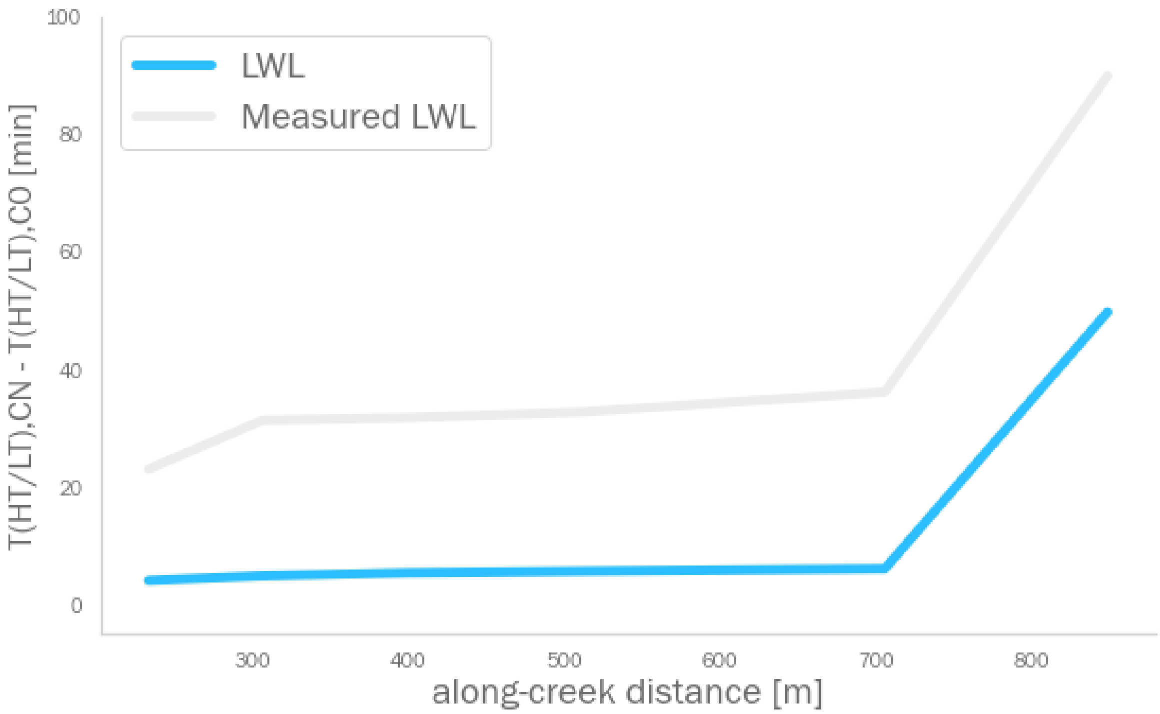

Figure B.2: Along creek delay of the LWL, modeled using the base-case model

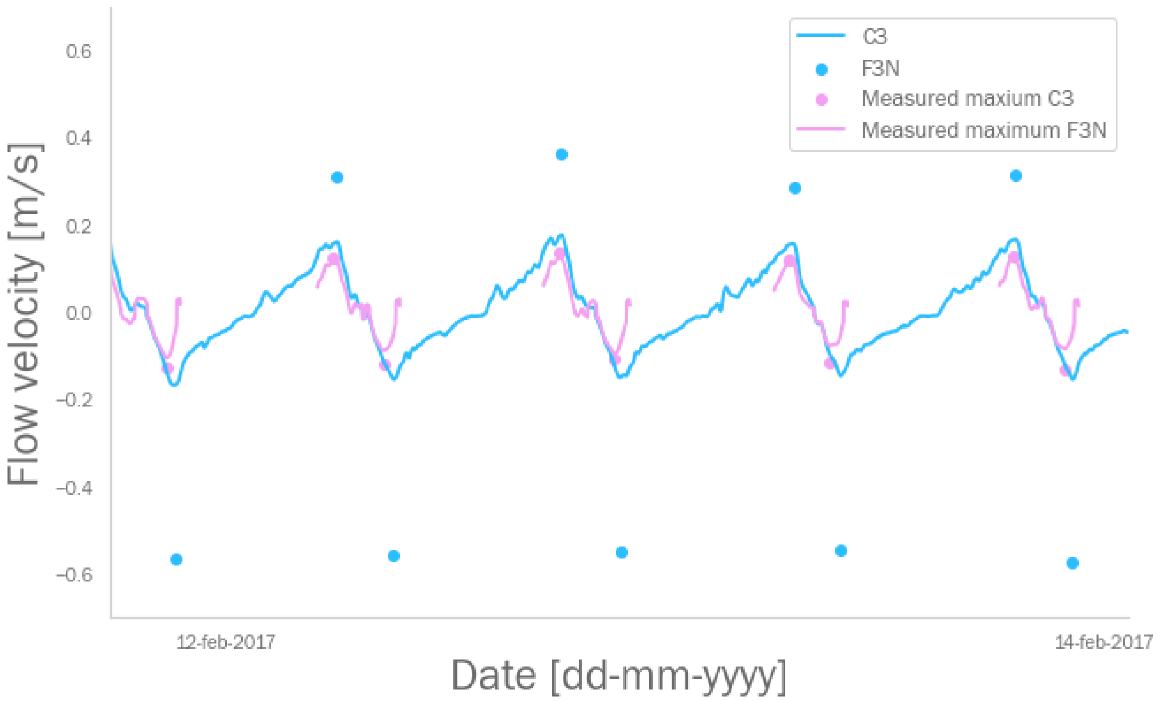

Figure B.3: Flow velocity in creek station C3 and concurring forest station F3N, modeled using the base-case model

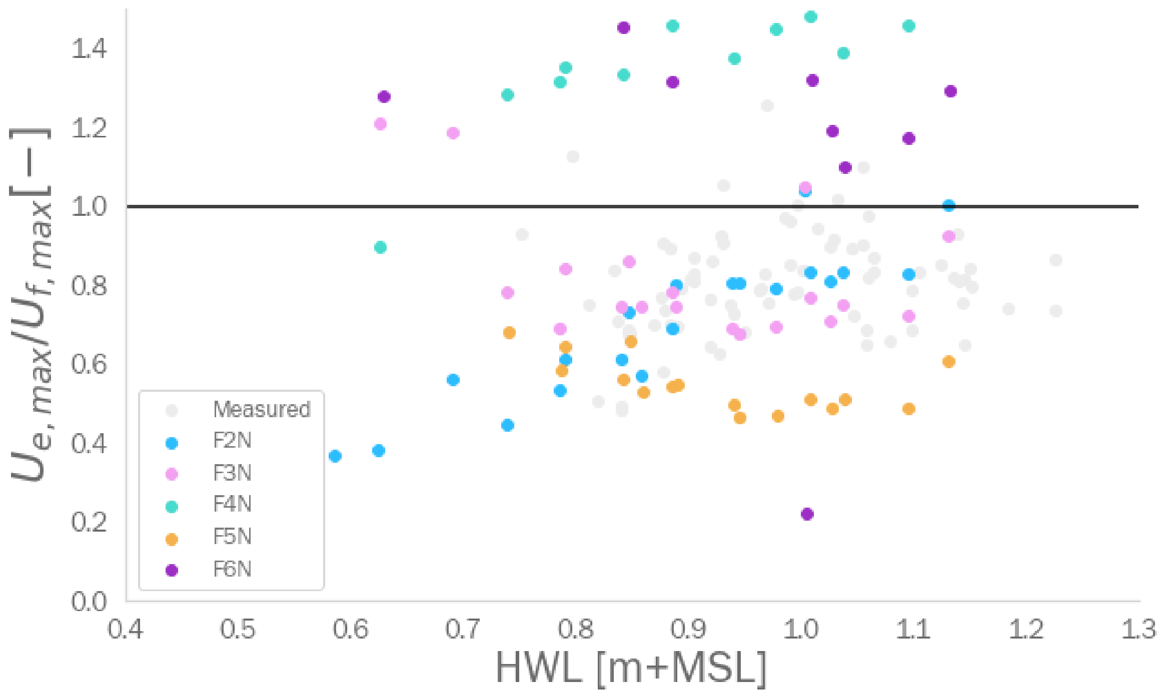

Figure B.4: Ratio between maximum ebb and flood flow velocities at the forest stations, modeled using the base-case model

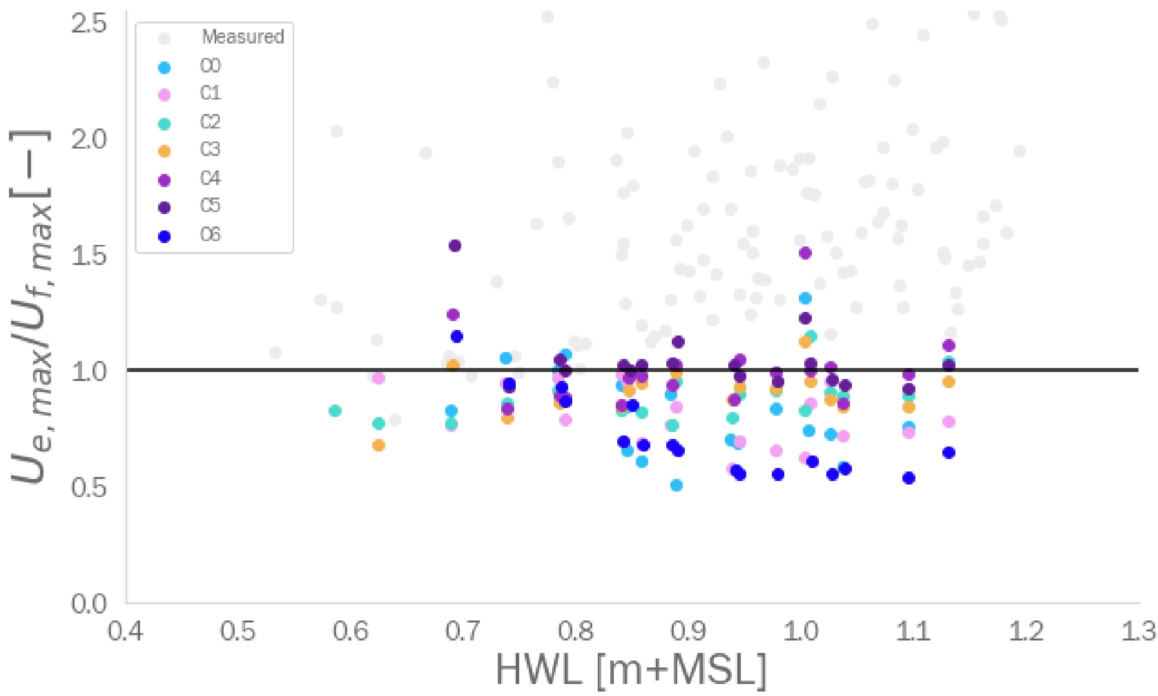

Figure B.5: Ratio between maximum ebb and flood flow velocities at the creek stations, modeled using the base-case model

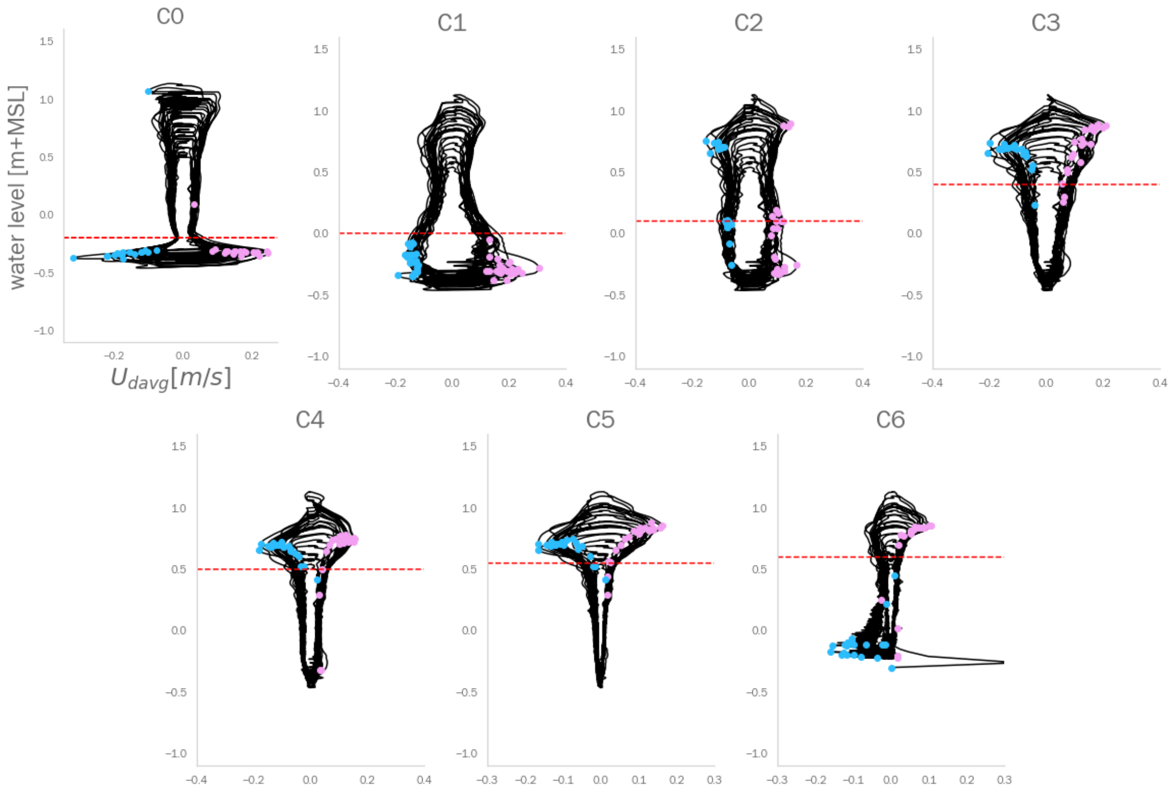

Figure B.6: Simulated tidal flow-stage velocity curves for all creek stations, blue and pink dots indicate maximum ebb and flood tidal velocities during each individual tide. Modeled using the base-case model